Exploring strategies for enhancing type I interferon responses to radiotherapy by modulating cGAS-dependent and -independent mechanisms

Wing Yu Lee

St Hilda's College

University of Oxford

A thesis submitted for the degree of

Master of Science by Research in Oncology

8th October 2025 (Trinity Term)

Word Count: 16665

Contents

Abstract

The potential of inducing anti-tumour immunity after radiotherapy, especially type I interferon (IFN) production that can facilitate immune cell recruitment, has recently been explored in different cancer contexts to enhance therapeutic efficacy. The cyclic GMP-AMP synthase (cGAS)/stimulator of interferon genes (STING) pathway has been regarded as one of the major routes in detecting cytosolic DNA as a result of DNA damage caused by radiotherapy. However, the possible formation of micronuclei (MN) harbouring highly condensed nucleosomal DNA post-radiation has been thought to hinder cGAS/STING pathway activation, and hence reduce type I IFN production. This study thus aimed to investigate whether type I IFN production induced by radiation could be promoted by altering cGAS-independent pathways such as suppressing glycogen synthase kinase-3 beta (GSK3β), or by boosting activation of the cGAS/STING pathway itself through histone deacetylase (HDAC) inhibition to amplify the pro-immunogenic effects of radiotherapy and increase therapeutic effectiveness. Results demonstrated that repression of GSK3β either by administration of GSK3β inhibitors or siRNA knockdown did not increase interferon-beta (IFN-β) production post-radiation. HDAC inhibition with vorinostat increased histone acetylation and, at moderate concentrations, possibly increased cGAS binding to MN and nuclear interferon regulatory factor-3 (IRF-3) levels shown by immunofluorescence. However, effects were not sustained at higher concentrations and were not corroborated by bulk assays, suggesting that more evidence was required to further support these exploratory findings. Taken together, neither approach was sufficient to robustly enhance IFN-β induction post-radiation. Although the interventions did not yield strong effects, this study delineates key methodological constraints and the biological complexity of IFN regulation. It

clarifies the limits of indirect modulation and points towards alternative and more direct approaches.

Acknowledgements

I would like to thank Professor Geoff Higgins for his supervision and guidance throughout this project. I am also grateful to Dr Gonzalo Rodriguez-Berriguete for his mentorship and technical advice, and to the members of the Higgins Lab for their help and insightful discussions.

Finally, I wish to thank my family and friends for their unwavering support and understanding during my studies in the Department of Oncology at the University of Oxford.

Abbreviations

AP-1	Activating protein-1
ATP	Adenosine triphosphate
BCA	Bicinchoninic acid
BSA	Bovine serum albumin
cGAMP	Cyclic GMP-AMP
cGAS	Cyclic GMP-AMP synthase
CI	Confidence interval
CMV	Cytomegalovirus
DAPI	4′,6-diamidino-2-phenylindole
DDR	DNA damage response
DMEM	Dulbecco's Modified Eagle Medium
DMSO	Dimethyl sulfoxide
DSB	Double-strand break
DTT	Dithiothreitol
EDTA	Ethylenediaminetetraacetic acid
ELISA	Enzyme-linked immunosorbent assay
ER	Endoplasmic reticulum
FBS	Fetal bovine serum
GSK3β	Glycogen synthase kinase-3 beta

GFP	Green fluorescent protein
Gy	Gray
H3K27ac	Histone H3 lysine 27 acetylation
HCC	Hepatocellular carcinoma
HDAC	Histone deacetylase
HEK293	Human embryonic kidney 293
HEPES	4-(2-hydroxyethyl)piperazine-1-ethanesulfonic acid
IC_{50}	Half maximal inhibitory concentration
IF	Immunofluorescence
IFN	Interferon
IFN-β	Interferon-beta
IRF-3	Interferon regulatory factor-3
IRFs	Interferon regulatory factors
KATs	Lysine acetyltransferases
MFI	Median fluorescence intensity
$MgCl_2$	Magnesium chloride
MN	Micronuclei
NaCl	Sodium chloride
NF-κB	Nuclear factor-kappa B
OASL1	2'-5'-oligoadenylate synthase-like protein 1

p53	Tumour protein p53
p-IRF-3	Phospho-interferon regulatory factor-3
p-STING	Phospho-stimulator of interferon genes
p-TBK1	Phospho-TANK-binding kinase 1
PBS	Phosphate-buffered saline
PBS-T	Phosphate-buffered saline with Tween-20
PFA	Formaldehyde
Poly (I:C)	Polyinosinic-polycytidylic acid
PTMs	Post-translational modifications
RIG-I	Retinoic acid-inducible gene I
SDS	Sodium dodecyl sulfate
siNT	Non-targeting siRNA
STING	Stimulator of interferon genes
TBK1	TANK-binding kinase 1
TBS	Tris-buffered saline
TBS-T	Tris-buffered saline with Tween-20
TME	Tumour microenvironment
TRIM21	Tripartite motif-containing protein 21
WB	Western blotting
WT	Wildtype

List of figures

Main figures

Supplementary figures

1. Introduction

1.1 Radiotherapy and immunomodulation

Radiotherapy is a type of cancer treatment that uses ionising radiation to eradicate tumour cells by inducing DNA damage. By generating DNA lesions, particularly double-strand breaks (DSBs), radiotherapy disrupts cellular replication and survival, ultimately leading to tumour cell death. (1) It is commonly delivered either as a definitive treatment or in combination with surgery and systemic therapies like chemotherapy, with the aim of achieving effective local tumour control. (2)

From a radiobiological perspective, cellular and tumour responses to radiotherapy have traditionally been described by the “five R’s” of radiobiology: DNA damage repair, tumour cell repopulation, redistribution within the cell cycle, reoxygenation and intrinsic radiosensitivity. Together, these principles explain how radiation dose, scheduling and tumour biology may influence treatment efficacy and normal tissue responses. These classical concepts provide a foundational framework for understanding the biological effects of radiotherapy beyond its immediate cytotoxic action. (1,3)

Clinically, radiotherapy has been one of the most extensively used cancer treatments over the past decade for both curative and palliative intent. With approximately 20 million new cases of cancer diagnosed globally in 2022, around 10 million of these new patients were reported to require radiotherapy as part of their treatment procedures, demonstrating the prominent relevance of radiotherapy in treating various cancer types, ranging from head and neck cancers to cervical and prostate cancers. (4–6)

While radiotherapy is best known for killing cancer cells by creating irreversible and lethal DNA damage, its potential in inducing immunomodulatory effects on tumours and surrounding tissues has been explored in hopes of raising the treatment effectiveness of radiotherapy. Studies have shown that radiotherapy can induce the release of tumour antigens and upregulate a number of cell surface molecules on tumour cells, such as the major histocompatibility complex class I receptor for cross-presentation of tumour antigens leading to T cell priming, as well as the Fas cell surface death receptor for apoptosis induction. Such effects contribute to the proliferation and activation of immune cells, and hence trigger the production of cytokines and chemokines like interferons (IFNs) that can then enhance the infiltration of effector immune cells into the tumour microenvironment (TME), promoting an anti-tumour immune response. (7–10) Due to these immunomodulatory properties, radiotherapy has also been explored in combination with immunotherapy to reach an abscopal effect, which is the induction of a systemic response on remote and unirradiated metastases. One of the widely investigated examples is the combination with immune checkpoint blockade, as radiotherapy may upregulate the expression of immune checkpoints and their co-stimulatory molecules, such as programmed death-ligand 1 and B7-1/2, which can be resolved by the introduction of monoclonal antibodies for such immune checkpoints. (9–13) This demonstrated the ability of radiotherapy in producing robust immunogenic responses alongside its original purpose of primary tumour control.

While radiotherapy can stimulate anti-tumour immune responses, it is also recognised that its effects on the immune system are highly context- and dose-dependent, encompassing both immunostimulatory and immunosuppressive outcomes. In addition to promoting antigen release and IFN signalling, radiotherapy

can induce immunosuppressive mechanisms as well, including the recruitment of regulatory immune populations like regulatory T cells and myeloid-derived suppressor cells, depletion of tumour-infiltrating lymphocytes and the release of suppressive cytokines such as transforming growth factor-β that can inhibit T cell proliferation. (14–17) These effects may limit sustained immune activation following treatment and contribute to variable clinical responses.

Importantly, radiation dose and fractionation have been shown to critically influence radiation-induced immunogenicity and activation of the cGAS/STING pathway. Studies have demonstrated that low to moderate radiation doses can promote induction of the nuclear factor-kappa B (NF-κB) pathway, cytosolic DNA sensing and IFN signalling, displaying more immunostimulatory responses and effective cGAS/STING pathway activation. (18–20) On the other hand, higher single doses may induce DNA exonucleases such as three prime repair exonuclease 1, leading to degradation of cytosolic DNA and attenuation of cGAS/STING signalling. (14,17,21) Fractionated radiation was also considered locally immunosuppressive due to lymphocytes being cleared from the radiation field rapidly without sufficient time for recovery. (15,16) This dose-dependent balance provides a potential explanation for inconsistent immune activation following radiotherapy, and highlights the importance of understanding how downstream IFN responses are regulated following irradiation.

Beyond dose and fractionation effects, the immunological effects of radiotherapy are further shaped by the TME, which comprises multiple components including tumour cells, immune cell populations, stromal elements, blood vessels and the extracellular matrix that collectively influence radiation responses. (22,23) Immune cells within the TME, such as dendritic cells, classically activated (M1) macrophages

and tumour-infiltrating lymphocytes, can modulate how tumours respond to radiation by affecting antigen presentation, inflammatory signalling involving cytokines and chemokines, as well as recruitment of immune cells like cytotoxic T cells. At the same time, immunosuppressive components of the TME like regulatory T cells and tumour-associated macrophages may counteract these effects and dampen radiation-induced immune activation. (24–28) (**Figure 1**) As a result, tumour-intrinsic responses to radiotherapy, including the induction of innate immune signalling pathways within irradiated tumour cells, can have important downstream consequences for immune modulation within the TME, providing critical context for interpreting radiation-induced immune responses.

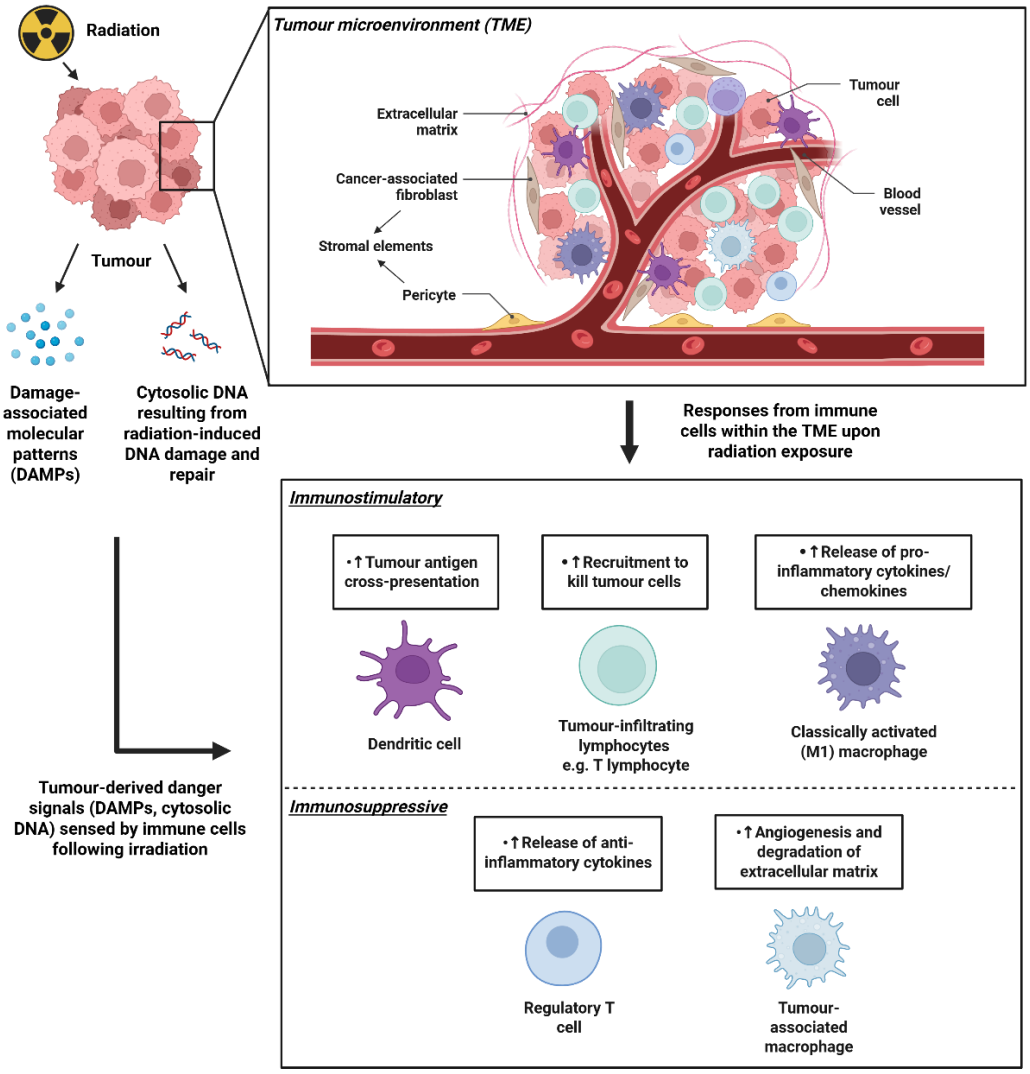

Figure 1. Radiotherapy-induced immunomodulation within the tumour microenvironment. Radiotherapy induces DNA damage and subsequent DNA repair in tumour cells, leading to the release of tumour-derived danger signals such as damage-associated molecular patterns (DAMPs) and cytosolic DNA. These signals are sensed by immune cells within the tumour microenvironment (TME), shaping downstream immunostimulatory and immunosuppressive responses. Immunostimulatory effects include enhanced tumour antigen cross-presentation, recruitment of tumour-infiltrating lymphocytes and release of pro-inflammatory cytokines and chemokines, whereas immunosuppressive components of the TME, such as regulatory T cells and tumour-associated macrophages, may counteract these effects and hinder immune activation. (Created with BioRender)

1.2 Type I interferons (IFNs) and anti-tumour immunity

As one of the most common cytokines induced upon activation of immune cells like plasmacytoid dendritic cells, (29,30) IFNs have been widely recognised for their functions in antiviral responses, but they have recently gained increasing attention for their anti-tumour properties. Type I IFNs like interferon-beta (IFN-β) can induce a range of intrinsic and extrinsic effects, affecting tumour cell growth and proliferation by means such as promoting apoptosis and inhibiting angiogenesis. (31,32) This ultimately leads to the stimulation of cytokine release, the recruitment of immune cells like tumour-infiltrating lymphocytes to the TME, as well as the induction of a range of immune cell responses. (32–36) In terms of innate immunity, type I IFNs have been shown to facilitate dendritic cell activation and presentation of tumour antigens essential for the initiation of an anti-tumour immune response. (36) They also possess the ability to enhance the phagocytic capacity as well as polarisation towards more pro-inflammatory phenotypes in macrophages. One study performed on mouse models and cell lines displayed an accumulation of potent anti-tumourigenic macrophages at tumour sites after intratumoural administration of cyclic GMP-AMP (cGAMP) that can strongly induce type I IFN production. (37,38) In terms of adaptive immunity, type I IFNs can promote $CD8^+$ T cell priming and boost the recruitment and effector functions of these cytotoxic T

cells, elevating their cytolytic activity for more effective tumour cell killing together with the help of $CD4^+$ helper T cells. (39–41) In addition to that, type I IFNs suppress the migration of regulatory T cells to tumour sites, restricting the formation of an immunosuppressive TME and thus strengthening the generation of an impactful anti-tumour immune response. (42) (**Figure 2**)

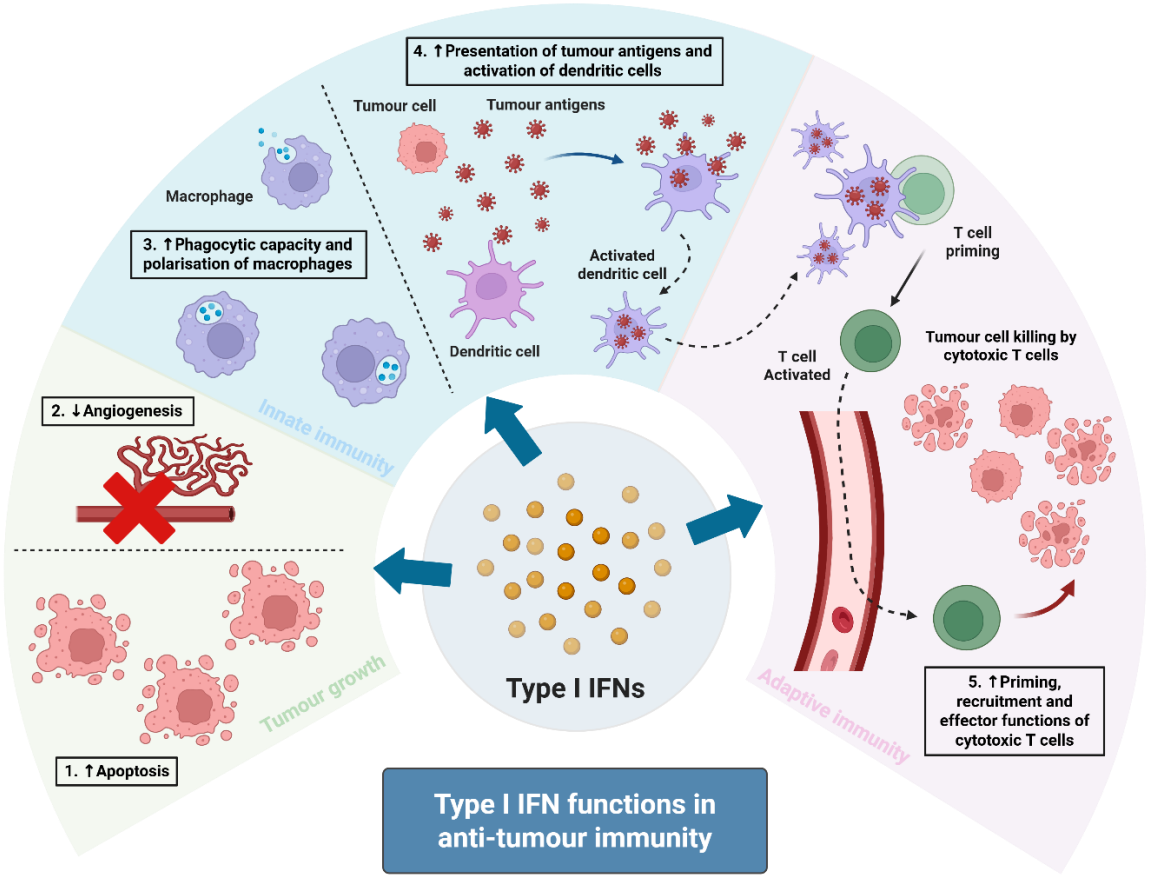

Figure 2. Anti-tumour properties of type I IFNs. Type I IFNs are capable of inducing different effects that lead to anti-tumour immune responses, including hindering tumour growth, recruiting and activating immune cells from innate immunity like dendritic cells and those from adaptive immunity like cytotoxic T cells. (Created with BioRender)

Overall, through these effects on the immune system, the induction of a type I IFN response can enhance anti-tumour immunity that inhibits cancer progression, promote immune clearance and potentially reshape the TME of immunosuppressive (immune-cold) tumours into immune-activating (immune-hot). (33,34) Therefore, it

is worth understanding whether boosting IFN responses induced by radiation may promote anti-tumour immunity and ultimately improve treatment outcomes.

1.3 Cyclic GMP-AMP synthase (cGAS)/stimulator of interferon genes (STING) pathway and radiotherapy-induced type I IFN production

Type I IFNs can possibly be induced through numerous innate immune sensors and signals. Some examples are toll-like receptors and retinoic acid-inducible gene I (RIG-I)-like receptors, which are capable of recognising damage-associated molecular patterns released upon tissue injury or tumour cell death, as well as sensing cytosolic RNA from pathogens like oncolytic viruses. Subsequent signalling pathways from these receptors then eventually converge on transcription factors including interferon regulatory factors (IRFs) like IRF-3, IRF-7, as well as NF-κB, driving the transcription of type I IFNs. (43–46) However, among the broad range of signalling pathways that are able to promote type I IFN production, the cGAS/STING pathway has been reported to play a central role in mediating type I IFN responses in various cell types ranging from tumour cells themselves to immune cells like dendritic cells especially after radiation. (47–51)

As mentioned previously, radiotherapy eliminates cancer cells primarily by inducing DNA damage. In cells that survive this damage after exposure to ionising radiation, the DNA repair process may lead to the formation of cytosolic DNA fragments, such as through incomplete DNA repair or the generation of chromosomal aberrations arising from DNA DSBs, which may mis-segregate during mitosis and localise in the cytoplasm. (51–53) These fragments can then be detected by cytosolic DNA sensors like cGAS. Once cGAS detects DNA, it induces the formation of cGAMP

that then activates downstream components of the pathway like STING. STING activation promotes the activation of TANK-binding kinase 1 (TBK1), which contributes to the phosphorylation of key transcription factors like IRF-3 and NF-κB. (33) The translocation of these transcription factors into the nucleus induces the transcription and production of type I IFNs, and ultimately leads to the induction of a radiation-induced anti-tumour immune response. (**Figure 3**) Therefore, both direct DNA damage that leads to cell death and the development of immune responses triggered by detection of cytosolic DNA can contribute to the therapeutic effects of radiotherapy.

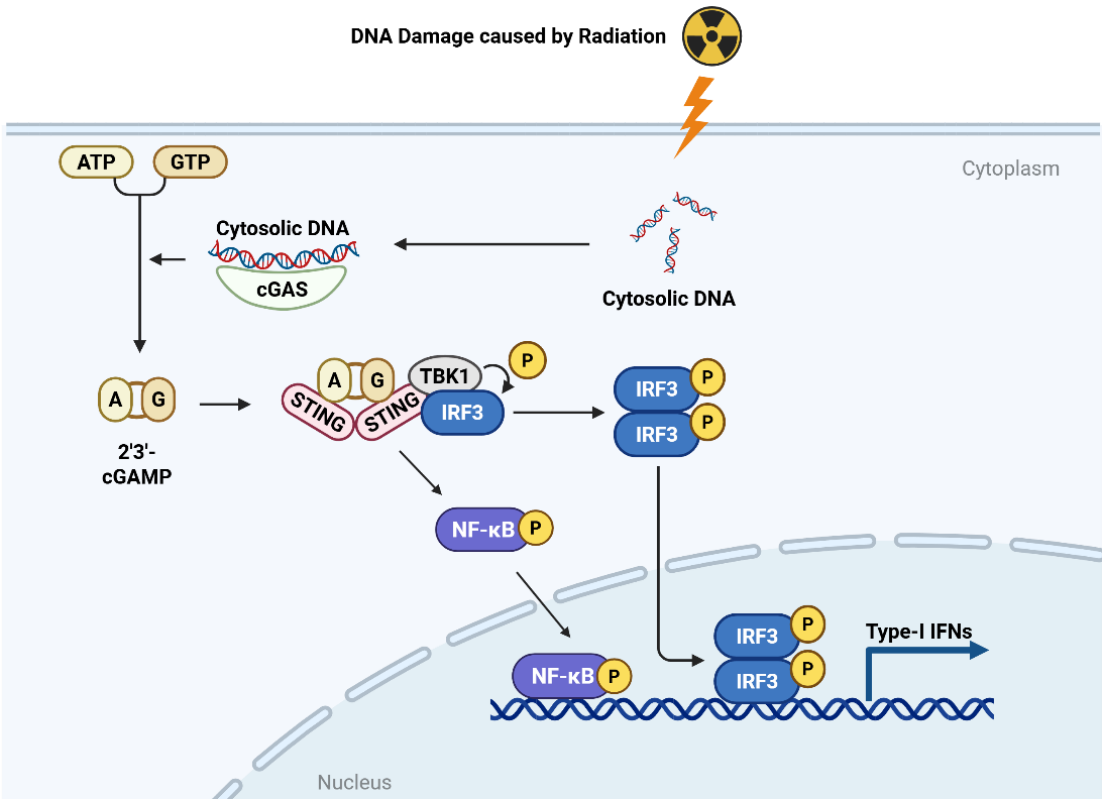

Figure 3. Illustration of the cGAS/STING pathway. Cytosolic DNA can be generated following DNA damage induced by radiotherapy, which is then detected by cGAS. cGAS activation leads to the production of cGAMP, which in turn activates downstream signalling components like STING, TBK1, IRF-3 and NF-κB that eventually results in type I IFN production. (Created with BioRender)

The production of type I IFNs induced post-radiotherapy plays an important role in unleashing the anti-tumour effects of radiotherapy and facilitating better treatment outcomes. One study showed an increase in intratumoural IFN-β production in tumours as well as increased T cell priming and T cell-dependent tumour regression following radiotherapy. They also suggested that type I IFNs were essential for radiotherapy-mediated tumour reduction by demonstrating a much stronger inhibition of tumour outgrowth post-radiotherapy in normal mice compared to mice that were unresponsive to type I IFNs. (54) Another study performed on patients with hepatocellular carcinoma (HCC) displayed increased serum levels of IFN-β post-radiation, particularly in those with favourable responses to treatment. (55) Higher post-radiotherapy serum IFN-β levels were also associated with better progression-free survival, which was validated in a similar study conducted on HCC patients that showed association with better overall survival as well. (56) These highlight the potential increase in therapeutic efficacy for radiotherapy when elevation in type I IFN levels is achieved post-radiation.

1.4 Challenges in cGAS/STING pathway activation post-radiation

While the cGAS/STING pathway itself is a major driver of IFN production, it was previously believed that cGAS detects DNA released from radiation-induced micronuclei (MN), which are fragments of the nuclear genome caused by DNA damage or chromosomal segregation errors and not incorporated into the main nucleus, upon rupture of the micronuclear envelope. This then activates STING and subsequent IFN signalling. (57–62)

However, recent findings have challenged this idea, showing that MN often contain highly condensed nucleosomal DNA that, despite binding to cGAS, limits cGAS/STING activation and reduces type I IFN production. (63–65) A study conducted by Takaki et al. mainly demonstrated this by showing that increased cGAS localisation to MN post-radiation did not result in significant changes in cGAMP levels. Nucleosome structures within MN were also suggested to structurally inhibit cGAS activation due to the acidic patch on histone H2A/H2B outcompeting double-stranded DNA for the DNA-binding surface of cGAS, causing cGAS to preferentially bind to these highly condensed structures. Moreover, naked DNA from sources like viruses can successfully activate the cGAS/STING pathway, further validating the effect of highly condensed nucleosomal DNA on hindering cGAS/STING pathway activation. (65) Nevertheless, while this has helped clarify why cGAS activation may be limited post-radiation, studies exploring strategies to overcome this barrier and restore or enhance cGAS/STING signalling are still lacking. Furthermore, although previous work has characterised cGAS binding to MN, (57–65) few studies have functionally linked these observations to downstream type I IFN signalling outcomes.

1.5 cGAS-independent induction of type I IFN response with glycogen synthase kinase-3 beta (GSK3β) inhibition

To overcome the above challenge, cGAS-independent alternative pathways were first considered to evaluate whether targets beyond the cGAS/STING pathway could compensate for the limitations observed with MN and enhance type I IFN responses. GSK3β, a kinase involved in glucose homeostasis, was ultimately selected as the target for this part of the study. It has been shown that many proto-

oncogenic or tumour suppressing transcription and translation factors are substrates of GSK3β, such as β-catenin, NF-κB and tumour protein p53 (p53), with GSK3β being an important regulator of the Wnt/β-catenin signalling pathway, which is responsible for regulating cellular functions like proliferation, differentiation and apoptosis, by phosphorylating β-catenin and promoting its proteasomal degradation. (66–70) While GSK3β generally acts as a positive modulator of NF-κB-dependent transcription, its overall role in cancer is highly context-dependent. GSK3β has been reported to be a tumour promoter in cancer types like pancreatic or colorectal cancer, while being a suppressor in others like gastric, breast or prostate cancer. (66,71,72) In terms of being a tumour promoter, overexpression of active GSK3β was reported to sustain pro-survival transcription and aggressive phenotypes. Elevated levels of total and active GSK3β were capable of triggering apoptosis, correlated with worse prognosis and disrupted transcription mediated by the NF-κB pathway independent of nuclear β-catenin status. (71–77) In terms of being a tumour suppressor, GSK3β was mainly believed to hinder cancer cell proliferation and survival by promoting the degradation of β-catenin, which is responsible for activating transcription of genes for cancer cell growth. GSK3β was also suggested to downregulate numerous proto-oncogenic proteins and cell cycle checkpoint proteins to inhibit cell proliferation and restrain epithelial-mesenchymal transition. (66,72,75,78–81)

Despite GSK3β inhibition being reported to sensitise various cancers to radio- and chemotherapy in cells, (72,82,83) it is unclear whether GSK3β negatively regulates IFN-β production. Therefore, it was hypothesised that if GSK3β negatively regulates IFN-β production, then upon repression of GSK3β, IFN-β production will increase following irradiation to improve pro-immunogenic responses. To test this, two small-molecule inhibitors – LY2090314 and 9-ING-41 – were selected. Both drugs are

potent, highly selective adenosine triphosphate (ATP)-competitive GSK3β inhibitors and are currently under evaluation in early-phase clinical trials, (84–89) deeming them suitable for assessing how GSK3β inhibition may influence downstream type I IFN signalling induced by radiation.

Although both GSK3β inhibitors have been investigated in combination with chemotherapy in several cancer models, such as bladder cancer and glioblastoma, as well as in clinical trials with established safety profiles, studies examining their combination with radiotherapy remain limited. Existing literature has largely focused on their effects as monotherapies or in combination with chemotherapeutic agents, with little direct evaluation of their interactions with radiation-induced signalling pathways. (86–88,90–92) Thus, the role of GSK3β and the influence of its inhibition, particularly by the inhibitors used in this study, warrant further investigation in the context of radiotherapy.

1.6 Activation of cGAS/STING pathway with histone deacetylase (HDAC) inhibition

As mentioned previously, the recent study conducted by Takaki et al. showed that cGAS activation was structurally limited due to highly condensed nucleosomal DNA in radiation-induced MN, while naked DNA from sources such as viruses could successfully activate the cGAS/STING pathway. (65) Therefore, in the second part of this study, we reverted our focus back to the cGAS/STING pathway in an attempt to directly address the hindrance in activation of this pathway caused by MN.

HDACs are responsible for reducing acetylation in histones and hence condense chromatin structures, making DNA less accessible for transcription and thus

decreasing gene expression. While HDACs are often overexpressed in malignant cells, (93) we hypothesised that HDAC inhibition may relax chromatin structures by increasing acetylation to allow cGAS to bind to more accessible DNA upon radiation-induced MN formation. This may then potentially promote activation of cGAS and the cGAS/STING pathway, leading to increased downstream signalling like nuclear translocation of the key transcription factor IRF-3, that can ultimately lead to increased IFN-β production. To evaluate this, the HDAC inhibitor vorinostat was selected, as its pan-HDAC inhibition nature can ensure effective increases in acetylation levels, potentially inducing effects on MN. (94,95) Vorinostat is an approved drug for cutaneous T-cell lymphoma, with additional evidence of tolerability in combination with radiotherapy or chemotherapy in early-phase clinical trials. In particular, results from several phase I clinical trials combining the use of vorinostat with radiotherapy showed good overall tolerance in patients with malignancies like gastrointestinal carcinoma, glioblastoma and paediatric glioma, (96–99) making it a suitable candidate for exploring links between HDAC inhibition, radiation and type I IFN signalling.

1.7 Aims and objectives of the study

This study therefore investigated strategies to address the above challenge and enhance IFN-β production post-radiation through two main approaches, which were (1) modulating IFN-β signalling via potentially cGAS-independent alternative pathways, more specifically repression of GSK3β and (2) promoting cGAS/STING pathway activation through chromatin remodelling by investigating whether HDAC inhibition could increase DNA accessibility via decreasing chromatin compaction in MN and facilitate cGAS activation.

The challenge in activating the cGAS/STING pathway post-radiation and the two main approaches investigated are summarised in **Figure 4**. The ultimate aim of the study was to enhance IFN-β production post-radiation to boost pro-immunogenic effects of radiotherapy and improve therapeutic efficacy.

To achieve the above aims, the following objectives were set out:

1. Evaluate the effects of GSK3β inhibition on IFN-β production levels post-radiation using siRNA knockdown and small-molecule GSK3β inhibitors.

2. Determine whether HDAC inhibition with vorinostat increases micronuclear DNA accessibility and enhances cGAS/STING activation post-radiation, examined by cGAS binding to MN and IRF-3 nuclear translocation.

3. Assess whether HDAC inhibition augments downstream signalling components of the cGAS/STING pathway involved in type I IFN production post-radiation.

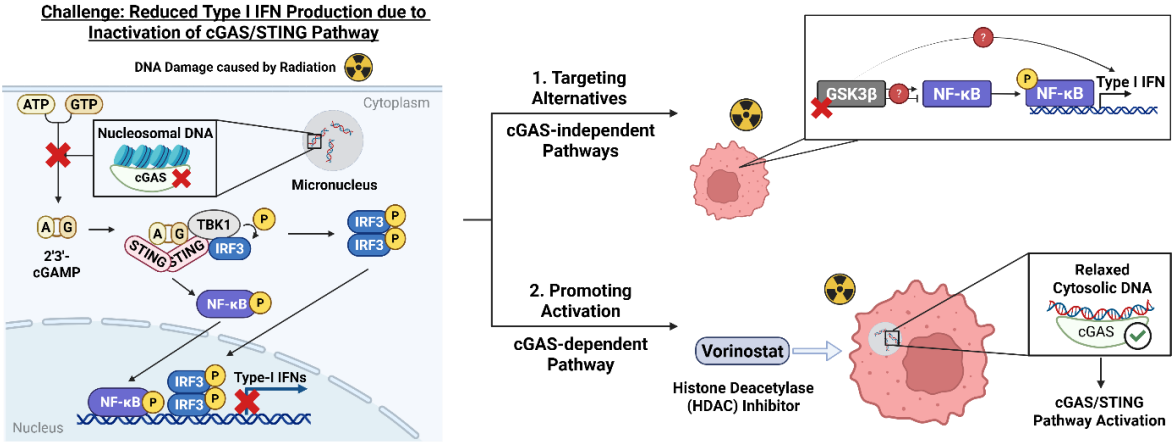

Figure 4. Schematic overview of rationale and key aims of the study. Radiotherapy can induce DNA damage and micronuclei (MN) formation, but highly condensed nucleosomal DNA within MN may restrict cGAS activation and thereby limit type I IFN production. To address this, two main strategies were explored: (1) targeting cGAS-independent alternative pathways via GSK3β inhibition to modulate type I IFN signalling and (2) promoting activation of cGAS/STING signalling via HDAC inhibition to relax chromatin structures in MN and increase DNA accessibility. Together, these approaches were evaluated for their ability in restoring type I IFN production and enhancing anti-tumour immunity post-radiotherapy. (Diagram created with BioRender)

2. Materials and Methods

2.1 Cell culture

Human embryonic kidney 293 (HEK293) wildtype (WT) cells (a kind gift from Professor Ian Tomlinson) and HeLa WT cells (human cervical adenocarcinoma cell line) (American Type Culture Collection) were cultured in Dulbecco's Modified Eagle Medium (DMEM) high glucose (Sigma-Aldrich) supplemented with 10% fetal bovine serum (FBS) (Gibco) and 1% Penicillin-Streptomycin (Sigma-Aldrich cat #P4333) in a water-jacketed incubator (37°C, 5% carbon dioxide, humidified) respectively. Cell lines were tested for mycoplasma contamination monthly and before running each experiment with Mycoalert™ Mycoplasma Detection Kit (Lonza cat #LT07-418). Cell samples were spun at 200 xg for 5 minutes, and the supernatant was transferred to a white 96-well flat bottom plate. Mycoalert™ Reagent (Lonza cat #LT27-237) and Mycoalert™ Substrate (Lonza cat #LT27-238) were reconstituted in Mycoalert™ Assay Buffer (Lonza cat #LT27-220) according to manufacturer's instructions, and then incubated for 15 minutes at room temperature. Mycoalert™ Reagent was added to samples in a 1:1 volume ratio and incubated for 5 minutes before measuring luminescence with the POLARstar Omega microplate reader (Bmg Labtech). Mycoalert™ Substrate was then added to samples with the same volume as the Mycoalert™ Reagent added, and incubated for 10 minutes before measuring luminescence. Experiments only proceeded when results were mycoplasma-negative (second luminescence reading divided by first reading < 0.9).

2.2 Small interfering RNA (siRNA) transfections for knockdown of GSK3β

Silencer™ Select Negative Control No. 1 siRNA (Invitrogen cat #4390844) was used as the non-targeting siRNA (siNT) control. Both siNT and siGSK3β (5'-CUCAAGAACUGUCAAGUAAtt-3') (Silencer™ Select validated siRNA from

Invitrogen) were diluted with 1X Opti-MEM Medium (Gibco) to reach a concentration of 200 nM. Lipofectamine RNAiMAX Transfection Reagent (Invitrogen cat #13778075) was diluted with 1X Opti-MEM Medium in a 1:100 dilution, then mixed with the diluted siRNA in a 1:1 volume ratio. The transfection complex was incubated on ice for 20 minutes before being added to HEK293 cells seeded at 1.5 x 10^6 cells per well (7.5 x 10^5 cells/mL) in 6-well plates, with a final concentration of 20 nM for siRNA and a 1:1000 dilution performed in total for RNAiMAX. 72 hours after transfection, cells were collected either for plasmid transfection or Western blotting (WB).

2.3 Plasmid transfections

The CMV-GFP plasmid (green fluorescent protein (GFP) expressed under the cytomegalovirus (CMV) promoter) was used as a positive control for transient transfection and was a kind gift from Professor Len Seymour. The IFN-β-hygro reporter plasmid (enhanced GFP under the control of the IFN-β promoter, followed by an internal ribosome entry site and a hygromycin B phosphotransferase resistance cassette (EGFP-IRES-HygR)) was cloned in our laboratory and provided for use in experiments.

HEK293 WT cells or siRNA knockdown HEK293 cells collected 72 hours after siRNA transfection were seeded at 2.5 x 10^5 cells per well (5 x 10^5 cells/mL) in 24-well plates. Lipofectamine 3000 Reagent (Invitrogen cat #100022052) was first diluted with 1X Opti-MEM Medium in a 1:42.67 dilution. Plasmid DNA was diluted in 1X Opti-MEM Medium at a ratio of 1 µg plasmid per 50 µL 1X Opti-MEM. P3000 Reagent (Invitrogen cat #100022058) was then added to the diluted plasmids at 1 µL per 50 µL 1X Opti-MEM, and the master mixes were incubated for 5 minutes at room temperature. Diluted Lipofectamine 3000 Reagent and the diluted plasmid

master mixes were then mixed in a 1:1 volume ratio and incubated for 20 minutes at room temperature. The DNA-lipid complex was added to cells with a target plasmid DNA quantity of 0.5 µg per well, and samples were incubated for 24 hours before proceeding to inhibitor treatment or irradiation.

2.4 GSK3β inhibitor treatment and irradiation

HEK293 WT cells were treated 24 hours after plasmid transfection with 40 nM LY2090314 (Selleck Chemicals cat #S7063) or 20 µM 9-ING-41 (Selleck Chemicals cat #S9602) diluted in dimethyl sulfoxide (DMSO) (Sigma-Aldrich cat #D8418). A medium change was performed before inhibitor treatment. DMSO was added to untreated controls to reach a final concentration of 0.4%. Cells were irradiated at 10 Gray (Gy) using the GSR D1 ^{137}Cs gamma irradiator (Gamma-Service Medical GmbH), which produced γ radiation with photon energy of 662 keV and a calibrated dose rate of 1.65 Gy per minute, 4 hours after treatment. siRNA knockdown HEK293 cells were irradiated at 10 Gy following a medium change 24 hours after plasmid transfection.

2.5 Flow cytometry

HEK293 WT cells and siRNA knockdown HEK293 cells harvested at 24 or 72 hours post-irradiation were washed with 1X phosphate-buffered saline (Dulbecco A) (PBS) (Oxoid ref #BR0014G) and trypsinised with Trypsin-EDTA Solution (Sigma-Aldrich). FBS was added to stop trypsinisation, and samples were transferred to 96-well round bottom plates (Costar ref #7007). Cells were taken from untreated samples and boiled at 95°C, then mixed with cells taken again from untreated samples for positive control. Plates were centrifuged at 400 xg for 4 minutes. Cells were washed with 1X PBS and centrifuged (400 xg for 4 minutes), then stained with Zombie NIR Fixable Viability Kit (BioLegend cat #423106) and incubated at room temperature

for 20 minutes in the dark. After incubation, cells were centrifuged (400 xg for 4 minutes) and fixed with 4% Formaldehyde (PFA) diluted from Pierce™ 16% PFA (Thermo Fisher Scientific cat #28908) with 1X PBS, followed by an incubation of 10 minutes at room temperature in the dark. Cells were centrifuged (400 xg for 4 minutes) and resuspended in 1X PBS, then analysed on the CytoFLEX Flow Cytometer (Beckman Coulter). Data analysis was performed using FlowJo software 10.10.0.

2.6 HDAC inhibitor treatment and irradiation

For immunofluorescence microscopy (IF), HeLa WT cells were seeded in 96-well black microplates (PerkinElmer cat #101676-436) at 4000 cells per well (2 x 10^4 cells/mL) and left to incubate overnight. Cells were then treated with 0 nM, 50 nM, 200 nM or 500 nM vorinostat (Sigma-Aldrich cat #SML0061) diluted in DMSO. DMSO was added to untreated controls to reach a final concentration of 1%. Cells were irradiated at 3 Gy or 5 Gy using the GSR D1 gamma irradiator 4 hours after treatment, and harvested 48 hours after irradiation.

For WB, HeLa WT cells were seeded at 1 x 10^6 cells per well (5 x 10^5 cells/mL) in 6-well plates and incubated overnight. Cells were then treated with 0 nM, 200 nM, 500 nM, 1 µM or 2 µM vorinostat diluted in DMSO. DMSO was added to untreated controls to reach a final concentration of 1%. Cells were irradiated with the same conditions as above and harvested 48 hours after irradiation.

2.7 Positive control treatment

For IF, polyinosinic-polycytidylic acid (poly (I:C)) (Sigma-Aldrich cat #P1530) was reconstituted in tissue culture grade water (diethylpyrocarbonate-treated, DNASE, RNASE free) (Fisher BioReagents cat #BP561-1), followed by heating at 50°C for

10 minutes and cooling at room temperature for re-annealing before use. 1X Opti-MEM Medium was used to dilute poly (I:C) to reach a concentration of 160 µg/mL. Lipofectamine 2000 (Invitrogen cat #11668019) was diluted in a 1:3.57 ratio with 1X Opti-MEM Medium. Both dilutions were incubated on ice for 5 minutes, then mixed in a 1:1 volume ratio. The mixture was further incubated on ice for 20 minutes before being added to HeLa cells at a final concentration of 4 µg/mL for poly (I:C).

The second positive control 2'3'-cGAMP (Sigma-Aldrich cat #SML1229) was reconstituted in tissue culture grade water, diluted to 2 mM with 1X Opti-MEM Medium and incubated for 5 minutes on ice. Lipofectamine 2000 was then added in a 1:2 dilution, and the mixture was incubated on ice for 20 minutes. After incubation, the mixture was added to cells for 2'3'-cGAMP transfection at a final concentration of 50 µM. Cells treated with both positive controls were harvested 4 hours after transfection for IF analysis.

For WB, 2'3'-cGAMP was reconstituted in tissue culture grade water and diluted with 1X Opti-MEM Medium to reach a concentration of 250.26 µM. The diluted 2'3'-cGAMP was incubated on ice for 5 minutes, followed by addition of Lipofectamine 2000 to achieve a 1:6 dilution. The transfection complex was incubated on ice for another 20 minutes before transfecting HeLa cells at a final concentration of 26 µM. Cells were harvested 4 hours after transfection for WB.

2.8 Immunofluorescence (IF) microscopy

HeLa WT cells were washed with 1X PBS containing 0.1% Tween-20 (Sigma-Aldrich cat #P7949) (PBS-T) twice 48 hours after irradiation. Cells were then fixed with ice-cold 1X PBS containing 4% PFA and 2% sucrose (Sigma-Aldrich cat #S0389) for 10 minutes on ice. After fixation, cells were washed twice with 1X PBS-

T, then incubated with 1X PBS containing 0.5% NP-40 Surfact-Amps™ Detergent Solution (Thermo Scientific cat #85124) for 10 minutes at room temperature to permeabilise cells. Cells were washed twice with 1X PBS-T for 5 minutes per wash, followed by blocking with 3% Bovine Serum Albumin (BSA) (Sigma-Aldrich cat #A7906) in 1X PBS-T for 1 hour at room temperature. Primary antibody incubation was performed overnight at 4°C with the following: 1:1000 cGAS (Cell Signalling Technology cat #15102S), 1:500 IRF-3 (Cell Signalling Technology cat #10949S) and 1:2000 Histone H3 lysine 27 acetylation (H3K27ac) marker (Abcam cat #ab4729).

After the incubation, cells were washed three times gently with 1X PBS-T for 5 minutes per wash, then incubated for 1 hour at room temperature in the dark with the following secondary antibodies: 1:500 Goat anti-rabbit IgG Alexa Fluor 488 (Invitrogen cat #A11034), 1:500 Goat anti-rabbit IgG Alexa Fluor 555 (Invitrogen cat #A21429) and 1:1000 Goat anti-mouse IgG Alexa Fluor 647 (Invitrogen cat #A21236). Cells were also incubated with 100 ng/mL 4′,6-diamidino-2-phenylindole (DAPI) (Sigma-Aldrich cat #D9542) at the same time as the secondary antibodies. Cells were then washed three times gently with 1X PBS-T for 5 minutes per wash, submerged in 1X PBS and imaged with the Dragonfly spinning disk confocal microscope (Andor Technology).

2.9 Cell fractionation for WB

Irradiated HeLa WT cells were washed, scraped with a cell scraper and collected with 1X PBS. The cell pellets were resuspended in cytoplasmic extraction buffer consisting of 10 mM 4-(2-hydroxyethyl)piperazine-1-ethanesulfonic acid (HEPES) (Sigma-Aldrich cat #H3375), 1.5 mM magnesium chloride ($MgCl_2$) (Sigma-Aldrich cat #M8266), 10 mM potassium chloride (Alfa Aesar cat # A11662), 1.0 mM

ethylenediaminetetraacetic acid (EDTA) (Sigma-Aldrich cat #E5134) and 0.075% NP-40 in distilled water adjusted to pH 7.6. 1 mM dithiothreitol (DTT) (Thermo Scientific cat #R0861), 1X cOmplete™ Mini protease inhibitor cocktail (Roche cat #11836153001) and phosphatase inhibitor cocktail 2 (1:100 dilution) (Sigma-Aldrich cat #P5726) were added fresh to the buffer before use. Cells were incubated with the cytoplasmic extraction buffer for 5 minutes on ice, then centrifuged at 400 xg for 4 minutes. The supernatant containing the cytoplasmic extracts were moved to clean tubes, and the remaining nuclei were washed gently with cytoplasmic extraction buffer without NP-40 added.

The nucleus suspension was then centrifuged at 400 xg for 4 minutes, and the supernatant was removed. The nuclear pellets were resuspended in nuclear extraction buffer consisting of 20 mM HEPES, 1.5 mM $MgCl_2$, 420 mM sodium chloride (NaCl) (Sigma-Aldrich cat #S9888), 0.2 mM EDTA and 25% glycerol (Thermo Scientific cat #C15892.K2) in distilled water adjusted to pH 8.0. 0.5 mM DTT, 1X protease inhibitor cocktail and phosphatase inhibitor cocktail 2 (1:100 dilution) were added fresh to the buffer before use. 5 M NaCl was then added to the suspension to adjust salt concentration to 400 mM. Nuclear extraction buffer was added again to the suspension with the same volume as the previous addition. The suspension was vortexed and incubated on ice for 10 minutes with periodical vortex to resuspend the pellet and obtain the nuclear extracts. The tubes containing the cytoplasmic extracts or the nuclear extracts were then centrifuged respectively at 25000 xg for 10 minutes to pellet any nuclei. The supernatant from the tubes were transferred separately to clean tubes, and glycerol was added to the tubes containing the cytoplasmic extracts to reach a concentration of 20%.

2.10 Western blotting (WB)

For GSK3β knockdown validation, siRNA knockdown HEK293 cells were lysed with Pierce™ RIPA lysis buffer (Thermo Scientific cat #89900) containing 1X protease inhibitor cocktail and phosphatase inhibitor cocktail 2 (1:100 dilution). Cell lysates underwent sonication for 10 seconds and were centrifuged at 4°C at 25000 xg for 10 minutes. Bicinchoninic acid (BCA) assay was conducted to determine the total protein concentration in samples. Cell lysates were then mixed with 1X NuPAGE™ LDS Sample Buffer (Invitrogen cat #NP0007) containing 50 mM DTT and incubated for 5 minutes at 95°C. 4–20% Mini-PROTEAN® TGX™ 10-well, 50 µl Precast Protein Gels (Bio-rad cat #4561094) were used with 1X sodium dodecyl sulfate (SDS) running buffer. 1X SDS running buffer was prepared from 10X SDS running buffer containing 0.0347 M SDS (Sigma-Aldrich cat #L3771), 0.25 M Trizma® base (Sigma-Aldrich cat #T1503) and 1.918 M glycine (Sigma-Aldrich cat #G7126) in distilled water. Precision Plus Protein Dual Color Standards (Bio-Rad cat #1610374) and samples were loaded. After gel-running, proteins were transferred from the gels to nitrocellulose membranes using Trans-Blot Turbo Mini 0.2 µm Nitrocellulose Transfer Pack (Bio-Rad cat #1704158) and Trans-Blot® Turbo™ Transfer System (Bio-Rad cat #1704150). Membranes were blocked in 3% BSA in 1X Tris-buffered saline containing 0.1% Tween-20 (TBS-T) for 1 hour at room temperature. 1X Tris-buffered saline (TBS) was prepared from 20X TBS containing 0.4 M Trizma® base and 2.74 M NaCl in distilled water. Membranes were then incubated overnight at 4°C with the following primary antibodies: 1:1000 GSK3β (Cell Signalling Technology cat #9315S) and 1:50000 vinculin (Abcam cat #ab18058). Membranes were washed 3 times in 1X TBS-T and incubated for 1 hour at room temperature with the following secondary antibodies: 1:10000 Goat anti-rabbit IgG HRP-linked

Antibody (Cell Signalling Technology cat #7074S) and 1:20000 Horse anti-mouse IgG HRP-linked Antibody (Cell Signalling Technology cat #7076S). Membranes were then washed 3 times in 1X TBS-T, and protein bands were visualised using Amersham™ ECL Prime Western Blotting Detection Reagent (Cytiva cat #RPN2236) and the ChemiDoc Imaging System (Bio-Rad).

For HDAC inhibition, irradiated HeLa WT cells were lysed with the same reagents and conditions as above to obtain whole cell lysates. After determining protein concentrations in samples with BCA assay, whole cell lysates or fractionated lysates (cytoplasmic and nuclear extracts) then underwent the same steps as above for preparation of loading samples, gel running and transfer. Membranes were blocked in 5% BSA in 1X TBS-T for 1 hour at room temperature, then incubated overnight at 4°C with the following primary antibodies: 1:1000 phospho-IRF-3 (p-IRF-3) (Ser396) (Cell Signalling Technology cat #4947S), 1:1000 total IRF-3 (Cell Signalling Technology cat #11904S), 1:1000 phospho-STING (p-STING) (Ser366) (Cell Signalling Technology cat #19781S), 1:1000 H3K27ac (Abcam cat #ab4729), 1:1000 phospho-TBK1 (p-TBK1) (Ser172) (Cell Signalling Technology cat #5483S), 1:1000 NF-κB p65 (Cell Signalling Technology cat #8242T), 1:2000 histone H3 (Cell Signalling Technology cat #4499S) and 1:50000 vinculin (Abcam cat #ab18058). All antibodies were diluted with 5% BSA in 1X TBS-T except vinculin, which was diluted with 3% BSA in 1X TBS-T. Membranes were washed 3 times in 1X TBS-T and incubated for 1 hour at room temperature with the same secondary antibodies used above. Membranes were then washed 3 times in 1X TBS-T, and protein bands were visualised using the same detection reagents and imaging system as above.

2.11 Alamar blue assay

HEK293 cells were seeded in 96-well plates at 300 cells per well (1.71 x 10^3 cells/mL) and 500 cells per well (2.86 x 10^3 cells/mL) respectively. HeLa cells were seeded at 500 cells per well (2.86 x 10^3 cells/mL) and 750 cells per well (4.28 x 10^3 cells/mL) respectively. Cells were incubated overnight before treatment with LY2090314, 9-ING-41 or vorinostat. For LY2090314, HEK293 cells were treated at eight final well concentrations ranging from 5 nM to 640 nM in a two-fold serial dilution series. For 9-ING-41, HEK293 cells were treated with seven concentrations ranging from 4.875 nM to 312 nM in a two-fold serial dilution series, plus 20 μM as an additional high-concentration point. As for vorinostat, HeLa cells were treated at eight concentrations ranging from 25 nM to 3200 nM (3.2 μM) in a two-fold serial dilution series as well. For vehicle controls (0 nM), DMSO was added to wells to give final concentrations equivalent to the DMSO content in wells with the highest drug treatment concentrations (LY2090314: 0.512%, 9-ING-41: 1.6%, vorinostat: 2.56%). For the negative control, only DMEM was added to wells without any cells. After 4 hours, cells were irradiated with either 3 Gy (both HEK293 and HeLa cells) or 5 Gy (HeLa cells only). Cells were then left to incubate for 7 days in the incubator. At 72 hours post-radiation, the medium containing the GSK3β inhibitor 9-ING-41 was replaced with fresh medium without the inhibitors. At the end of the incubation period, the redox dye resazurin (Sigma-Aldrich cat #R7017) (dissolved in 1X PBS and warmed up to 37°C) was added to each sample in a 1:10 ratio to give a 1X solution with final concentration of 0.1 mg/mL. Samples containing the dye were incubated for another 3 hours before fluorescence measurement at 560Ex/590Em.

2.12 Statistical analysis

Data analysis and figure preparation were performed using GraphPad Prism 10.5.0. Results were presented as mean ± standard deviation or median ± interquartile range (specified in figure legends). For experiments on GSK3β repression and IF after HDAC inhibition, statistical significance was assessed on biological replicates or per-image mean intensities by two-way ANOVA with Dunnett's or Bonferroni's multiple comparisons, depending on whether comparisons were made between three or more conditions or two conditions respectively (specific contrasts detailed in figure legends). Paired t test was performed for individual comparison between two conditions. For cell viability curves, radiosensitisation was assessed by non-linear regression and comparison of half maximal inhibitory concentration (IC_{50}) across radiation doses using extra sum-of-squares F-test, if absolute IC_{50} with 95% confidence interval (CI) could be estimated from the fitted range covered by the curves (vorinostat). Otherwise, radiosensitisation was assessed by two-way ANOVA with Bonferroni's multiple comparisons for comparison between 0 Gy and 3 Gy for each concentration (LY2090314 and 9-ING-41). Unless stated otherwise, tests were two-sided and a p-value of < 0.05 was considered statistically significant.

3. Results

3.1 Impacts of GSK3β inhibitors on cell viability and radiosensitisation

While there is the possibility that IFN-β production may be influenced by cell death caused by irradiation or toxicity of the inhibitors, Alamar blue assays were conducted to verify whether effects on cell viability or radiosensitisation would introduce bias to the analysis regarding enhancement in IFN-β levels. HEK293 cells were seeded and treated with a range of concentrations for each inhibitor, irradiated at 3 Gy 4 hours after treatment, and subjected to fluorescence detection following addition of resazurin 7 days after irradiation.

3.1.1 9-ING-41

For 9-ING-41, HEK293 cell viability was reduced in a dose-dependent manner at both seeding densities of 300 cells per well (cells/well) and 500 cells/well (**Figures 5A-B**). In unirradiated cells (0 Gy), viability stayed close to baseline (around 100%) for concentrations below 100 nM, remaining almost flat from 0 nM to the point representing 78 nM. However, higher concentrations at around 156 nM started experiencing a much steeper drop in cell viability, with near-complete loss of viability at concentrations above 1 μM. When combined with 3 Gy irradiation, baseline viability was reduced to around 40% (300 cells/well) or 60% (500 cells/well), showing that radiation alone decreased baseline viability more strongly at lower seeding densities. Addition of 9-ING-41 further decreased viability across the tested concentration range, with a trend similar to that observed in unirradiated cells.

While irradiation alone reduced baseline viability, the overall dose-response curves for 9-ING-41 treatment in irradiated and unirradiated cells were of very similar shape, indicating that 9-ING-41 did not sensitise cells to radiation (**Figures 5A-B**). This was supported by normalising the irradiated condition to a baseline of 100% cell viability.

Comparison between 0 Gy and 3 Gy for each concentration point displayed no consistent significant differences (**Supplementary Figure 1**). Therefore, these results suggested that 9-ING-41 is more cytotoxic to HEK293 cells at higher concentrations of above 100 nM, and that this inhibitor did not provide evidence of consistent radiosensitisation effects on cells.

3.1.2 LY2090314

For LY2090314, HEK293 cell viability was also reduced in a dose-dependent manner at seeding densities of 300 cells/well and 500 cells/well (**Figures 5C-D**). At 0 Gy with 300 cells/well, viability remained close to baseline levels at concentrations below 10 nM, with only a gradual decrease with increasingly steeper slope from close to 100% at 5 nM to around 65% at 640 nM (**Figure 5C**). A similar trend was observed at 0 Gy with 500 cells/well, with a decrease of smaller extent from close to 100% at 5 nM to slightly above 80% at 640 nM (**Figure 5D**). When combined with 3 Gy irradiation, baseline viability was reduced to around 45% (300 cells/well) or 80% (500 cells/well) (**Figures 5C-D**). Across both densities, the addition of LY2090314 markedly reduced viability in irradiated samples compared to unirradiated samples, with a much sharper decline beginning at around 10 nM and extending through higher concentrations. At 3 Gy with 300 cells/well, viability dropped from around 45% at baseline to around 20% at approximately 30 nM, and approached near-complete loss of around 10% by 640 nM (**Figure 5C**). With 500 cells/well, viability dropped with increasingly steeper slope from 80% at baseline to around 40% at 80 nM, then further dropped to around 15% by 640 nM (**Figure 5D**). These suggested a leftward shift in the dose-response curve compared to 0 Gy.

Unlike the similar trends observed with 9-ING-41, comparison of irradiated versus unirradiated curves indicated radiosensitising effects of LY2090314, as the decline

in viability was consistently more pronounced under irradiation at both seeding densities (**Figures 5C-D**). This was further supported by statistical comparisons of cell viability at individual concentrations, which revealed significant differences between 0 Gy and 3 Gy for concentrations ranging approximately from 10 nM to 640 nM (**Figures 5E-F**). Therefore, these results indicated that LY2090314 is less likely cytotoxic to HEK293 cells unless concentration exceeds 100 nM, with radiosensitisation effects observed across the tested concentration range, in contrast to the other GSK3β inhibitor 9-ING-41.

3.2 Effects on IFN-β production post-radiation following administration of GSK3β inhibitors

To test whether GSK3β inhibition altered IFN-β production post-radiation, HEK293 cells were first treated with GSK3β inhibitors LY2090314 and 9-ING-41. Cells were transfected with or without the IFN-β-hygro reporter plasmid, treated with the inhibitors 24 hours after transfection, and then irradiated with 10 Gy 4 hours after the inhibitor treatments. Flow cytometry was then used to quantify the median fluorescence intensity (MFI) of the GFP signal measured in the live cell population. Another purpose of this experiment was to determine whether the inhibitors exhibited intrinsic fluorescence, as GFP signals produced from the reporter plasmid were mainly measured to quantify IFN-β promoter activity, and fluorescence from these inhibitors may interfere with such signals and skew the analysis.

Figure 6A shows the representative gating strategies for identifying GFP-positive cells from the live single cell population. The live cell gate and GFP-positive gate were set up according to the no treatment controls without the reporter plasmid, and

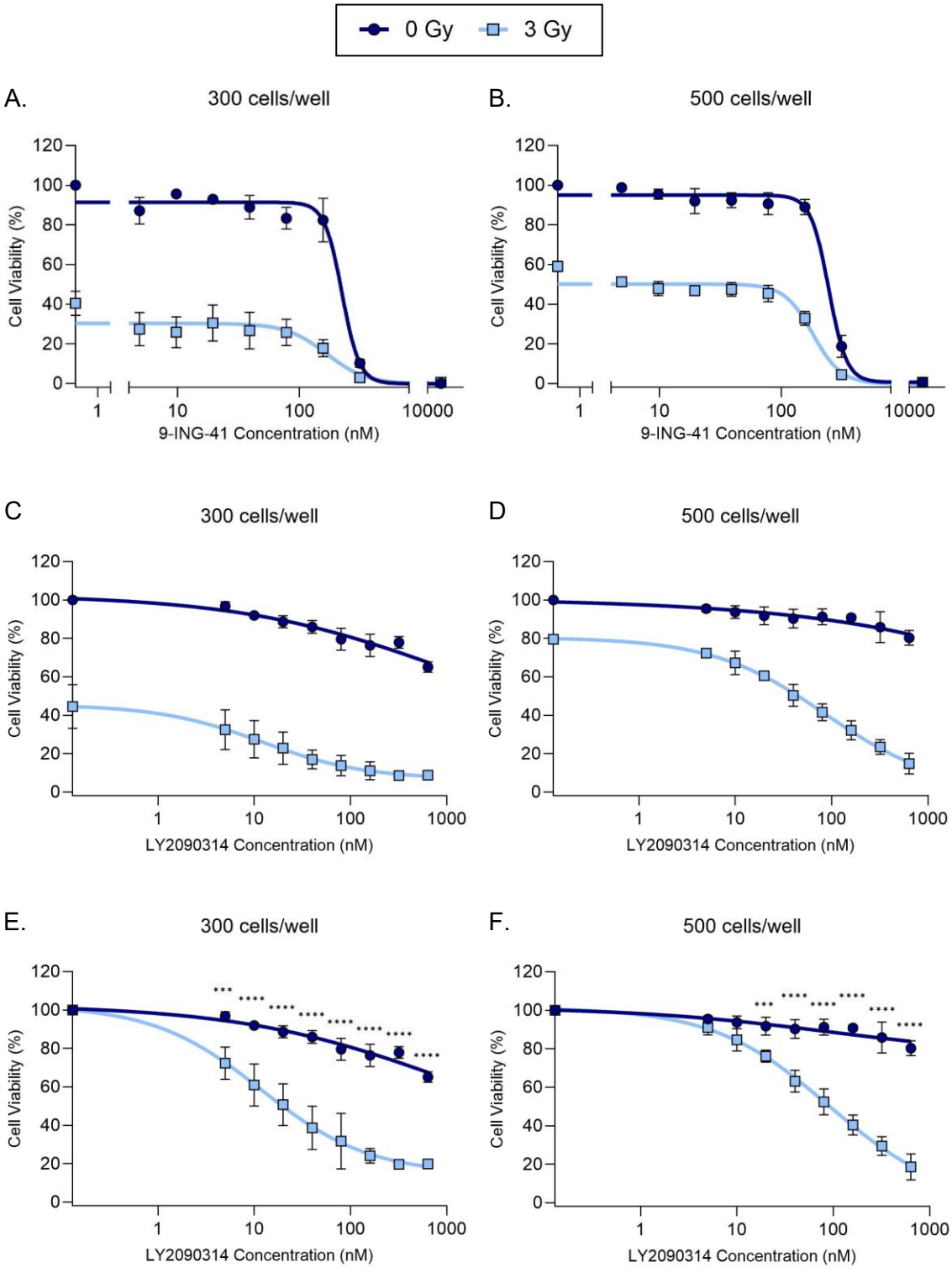
0 Gy
3 Gy
A.
300 cells/well
B.
500 cells/well
Cell Viability (%)
9-ING-41 Concentration (nM)
C
300 cells/well
D
500 cells/well
LY2090314 Concentration (nM)
E.
300 cells/well
F.
500 cells/well

Figure 5. HEK293 cell viability following treatment with GSK3β inhibitors of increasing concentrations and irradiation. HEK293 cells were seeded at two different seeding densities (300 and 500 cells/well) and treated with different concentrations of **(A-B)** 9-ING-41 (0, 4.875, 9.75, 19.5, 39, 78, 156, 312 nM and 20 μM) or **(C-D)** LY2090314 (0, 5, 10, 20, 40, 80, 160, 320 and 640 nM)**,** followed by irradiation with 3 Gy. Values obtained from fluorescence detection upon addition of resazurin to wells 7 days post-radiation were normalised to the vehicle control at 0 Gy (set as 100% cell viability) and the negative control (set as 0% cell viability). For LY2090314, cell viability was further normalised in **(E-F)** with values for 0 Gy normalised to vehicle control at 0 Gy (set as 100%) and values for 3 Gy normalised to vehicle control at 3 Gy (set as 100% as well) to detect any radiosensitisation effects. Data presented as mean ± standard deviation with x-axis plotted on a $\log_{10}$ scale. Three biological replicates (N = 3) with three technical replicates (n = 3). Statistical significance assessed on biological replicates by two-way ANOVA with Bonferroni's multiple comparisons for comparison between 0 Gy and 3 Gy for each concentration, *** $p < 0.001$, **** $p < 0.0001$.

the live cell gate was also verified by the live/dead dye positive control containing boiled dead cells. This was to ensure that an appropriate number of live cells could still be included in the analysis after exclusion of dead cells caused by radiation or inhibitor treatments. In addition to MFI levels (**Figures 6B-C, left panel**), the MFI distribution normalised to mode for each treatment condition was also presented as histograms for qualitative comparison (**Figures 6B-C, right panel**). GFP+ positive control confirmed successful plasmid transfection (**Figures 6B-C**).

At 24 hours post-radiation, no significant differences were observed between the MFI of the no stimulus control (with reporter plasmid, right of dashed line) and transfected samples treated with LY2090314, regardless of whether irradiation was performed (**Figure 6B**). The lack of significance was also seen at 72 hours post-radiation (**Figure 6C**). This suggested that IFN-β levels were not significantly affected by the administration of LY2090314. LY2090314 treatment alone did not significantly alter the GFP signals compared to the no treatment control (without plasmid, left of dashed line), again regardless of whether irradiation was conducted (**Figures 6B-C**), showing that no significant intrinsic fluorescence from LY2090314 was detected that might interfere with fluorescence activity of the reporter plasmid.

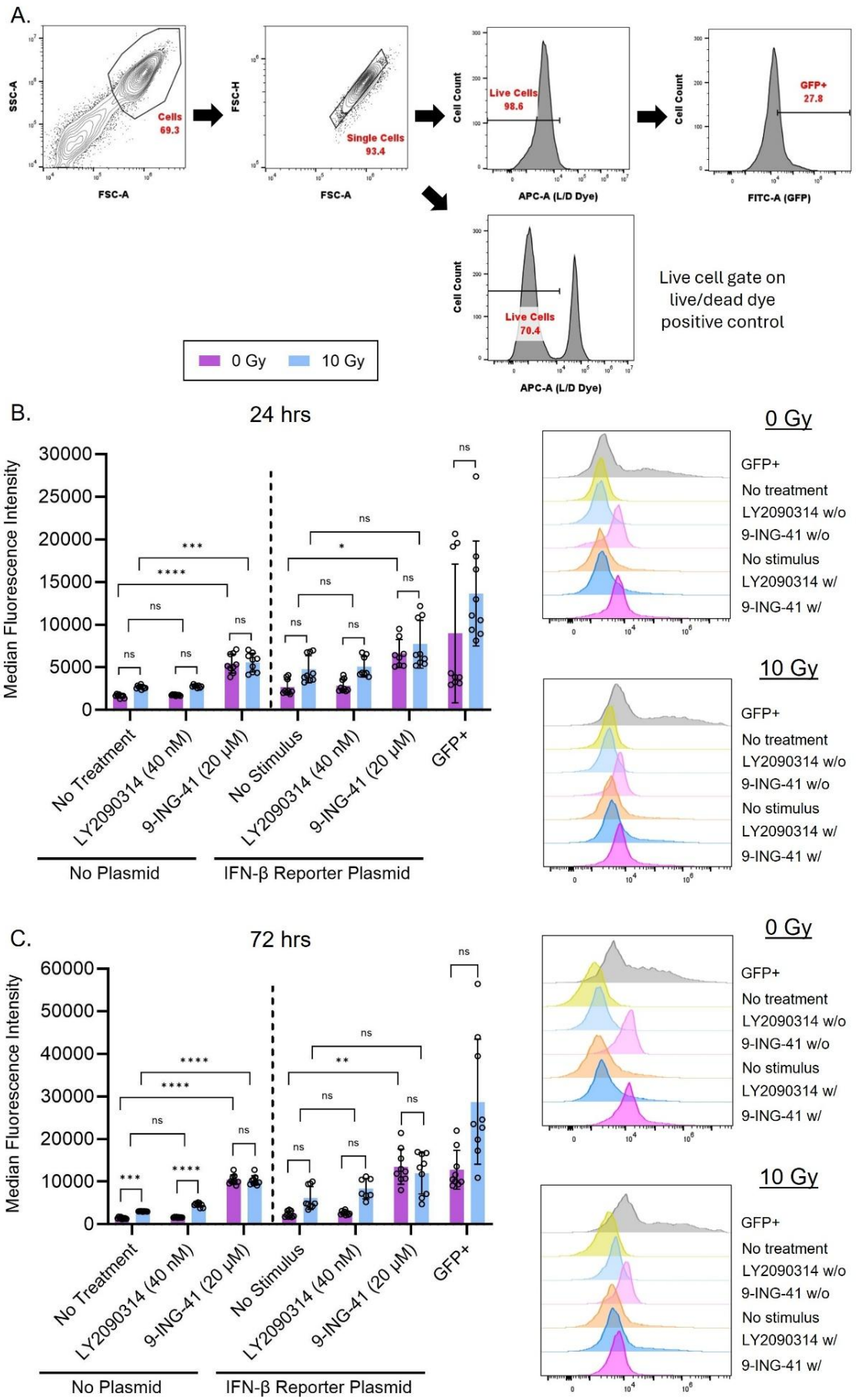
A.
SSC-A
FSC-A
Cells
69.3
FSC-H
FSC-A
Single Cells
93.4
Cell Count
APC-A (L/D Dye)
Live Cells
98.6
Cell Count
FITC-A (GFP)
GFP+
27.8
Cell Count
APC-A (L/D Dye)
Live Cells
70.4
Live cell gate on
live/dead dye
positive control
0 Gy
10 Gy
B.
24 hrs
Median Fluorescence Intensity
No Treatment
LY2090314 (40 nM)
9-ING-41 (20 μM)
No Stimulus
LY2090314 (40 nM)
9-ING-41 (20 μM)
GFP+
No Plasmid
IFN-β Reporter Plasmid
0 Gy
10 Gy
GFP+
No treatment
LY2090314 w/o
9-ING-41 w/o
No stimulus
LY2090314 w/
9-ING-41 w/
C.
72 hrs
Median Fluorescence Intensity
No Treatment
LY2090314 (40 nM)
9-ING-41 (20 μM)
No Stimulus
LY2090314 (40 nM)
9-ING-41 (20 μM)
GFP+
No Plasmid
IFN-β Reporter Plasmid
0 Gy
10 Gy
GFP+
No treatment
LY2090314 w/o
9-ING-41 w/o
No stimulus
LY2090314 w/
9-ING-41 w/

Figure 6. MFI of GFP signals measured in HEK293 live cells after GSK3β inhibitor treatment and irradiation. HEK293 cells were seeded and transfected with or without the IFN-β-hygro reporter plasmid, then treated with either LY2090314 (40 nM) or 9-ING-41 (20 μM) and irradiated at 10 Gy. Flow cytometry was used to measure stimulation in IFN-β promoter activity in the form of GFP signals. **(A)** Representative gating strategies employed in flow cytometry analysis for distinguishing GFP-positive cells from the live single cell population. At least 1000 cells were captured in each condition for analysis. The live/dead dye positive control (containing boiled dead cells) was also displayed as a reference of how the live cell gate was capable of gating out dead cells. MFI of GFP signals generated from the reporter plasmid at **(B)** 24 hours or **(C)** 72 hours post-radiation was reported **(left panel)** together with representative histograms displaying distribution of MFI normalised to mode for qualitative comparison **(right panel)** of shifts in GFP signal. GFP+ control confirmed successful transfection of plasmids. Data presented as mean ± standard deviation. N = 3, n = 3. Each circular symbol represents one technical replicate. Statistical significance assessed on biological replicates by two-way ANOVA with Dunnett's or Bonferroni's multiple comparisons (Dunnett's for comparison between no treatment control without plasmid or no stimulus control transfected with plasmid (both with DMSO) and their respective inhibitor-treated samples, Bonferroni's for comparison between radiation doses (0 Gy versus 10 Gy) for each condition). Paired t test for comparison between 0 Gy and 10 Gy for GFP+ transfection control. ns = non-significant, * $p < 0.05$, ** $p < 0.01$, *** $p < 0.001$, **** $p < 0.0001$. L/D, live/dead; GFP, green fluorescent protein; w/o, without; w/, with; MFI, median fluorescence intensity; DMSO, dimethyl sulfoxide.

However, there was a slightly significant increase in MFI in transfected samples treated with 9-ING-41 compared to the no stimulus control (with plasmid, right of dashed line) without exposure to radiation at 24 hours post-radiation ($p = 0.0457$) (**Figure 6B**). With exposure to radiation (10 Gy), this increase was no longer considered significant ($p = 0.1216$). This was also observed at 72 hours post-radiation (0 Gy: $p = 0.0027$, 10 Gy: $p = 0.0953$) (**Figure 6C**). At the same time, it was observed that samples treated with 9-ING-41 alone showed a significant increase in MFI compared to the no treatment control (no plasmid, left of dashed line) at both timepoints without radiation exposure (24 hours and 72 hours post-radiation: $p < 0.0001$) or after exposure to 10 Gy radiation (24 hours post-radiation: $p = 0.0004$; 72 hours post-radiation: $p < 0.0001$) (**Figures 6B-C**). All these suggested the possibility of intrinsic fluorescence from the drug itself that might interfere with GFP signals from the reporter plasmid. Therefore, the lack of

significant changes in IFN-β production post-radiation after administration of GSK3β inhibitors could not be entirely concluded from this experiment.

3.3 Effects on IFN-β production post-radiation following GSK3β knockdown with siRNA

To validate the results obtained from pharmacological inhibition of GSK3β and avoid the potential issue of fluorescence interference from the drugs, HEK293 cells were transfected with either siNT as control or siGSK3β to knock down GSK3β. 72 hours after that, siRNA knockdown cells were transfected with or without the IFN-β-hygro reporter plasmid and subjected to irradiation at 10 Gy 24 hours after plasmid transfection. Flow cytometry was again used to quantify the MFI of GFP signals. Similar gating strategies were applied (**Figure 6A**). Similar to above, apart from MFI levels (**Figures 7A-B, left panel**), histograms were also presented for qualitative comparison (**Figures 7A-B, right panel**). Successful knockdown of GSK3β in cells was confirmed by western blotting (**Figure 7C**).

According to **Figures 7A and 7B**, no significant differences in MFI were shown between the siNT control and samples with GSK3β knockdown that were transfected with the reporter plasmid at both 24 and 72 hours post-radiation. Similar results were obtained under both unirradiated and irradiated conditions. Consistently low GFP signals detected in controls without the reporter plasmid confirmed minimal GFP signal interference from siRNA transfection, while GFP+ positive control confirmed successful plasmid transfection. This suggested that IFN-β production was not significantly altered by GSK3β knockdown post-radiation, similar to what was observed after LY2090314 administration.

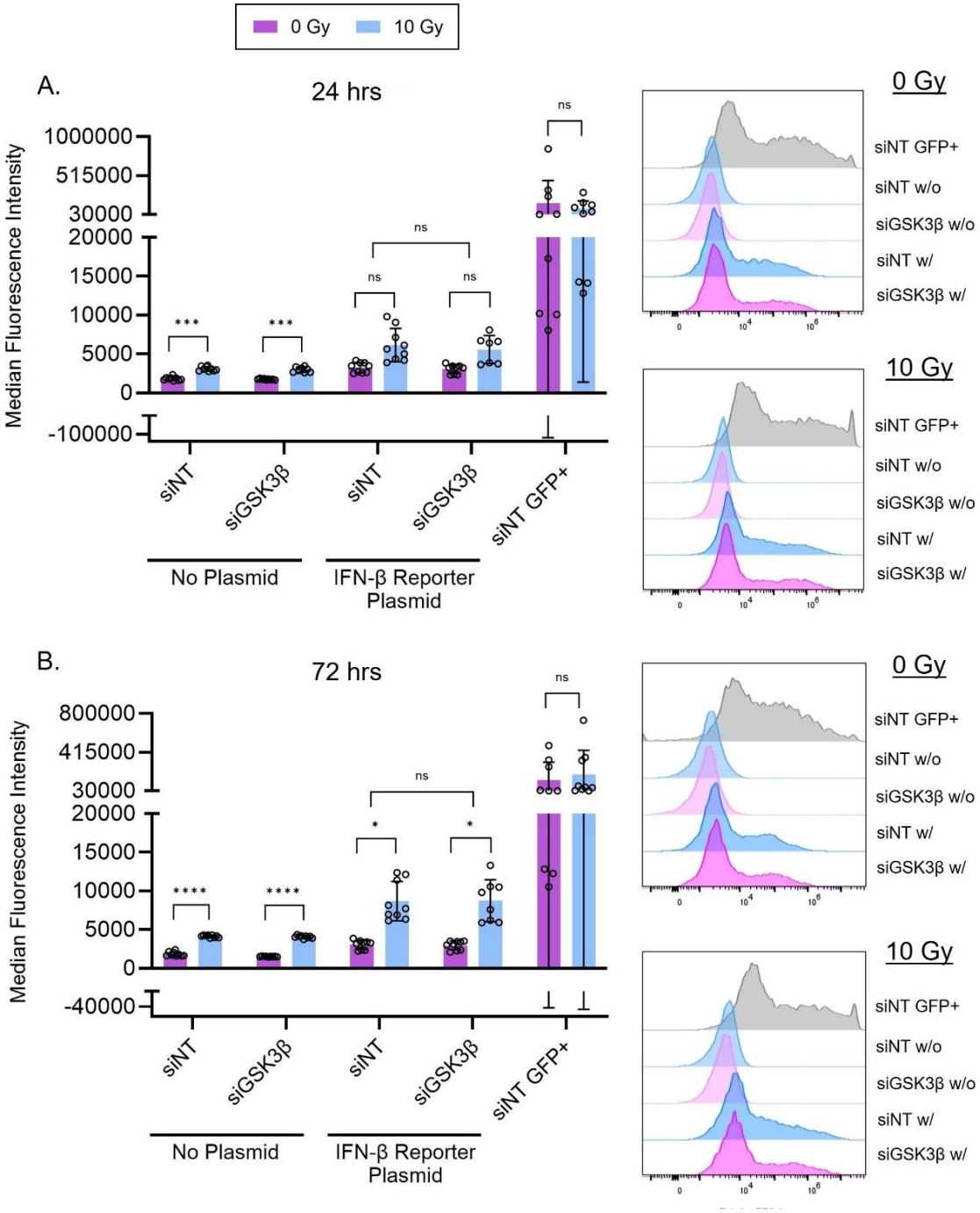
0 Gy
10 Gy
A.
24 hrs
Median Fluorescence Intensity
1000000
515000
30000
20000
15000
10000
5000
0
-100000
***
***
ns
ns
ns
ns
siNT
siGSK3β
siNT
siGSK3β
siNT GFP+
No Plasmid
IFN-β Reporter Plasmid
0 Gy
siNT GFP+
siNT w/o
siGSK3β w/o
siNT w/
siGSK3β w/
10 Gy
siNT GFP+
siNT w/o
siGSK3β w/o
siNT w/
siGSK3β w/
B.
72 hrs
Median Fluorescence Intensity
800000
415000
30000
20000
15000
10000
5000
0
-40000
****
****
*
*
ns
ns
siNT
siGSK3β
siNT
siGSK3β
siNT GFP+
No Plasmid
IFN-β Reporter Plasmid
0 Gy
siNT GFP+
siNT w/o
siGSK3β w/o
siNT w/
siGSK3β w/
10 Gy
siNT GFP+
siNT w/o
siGSK3β w/o
siNT w/
siGSK3β w/

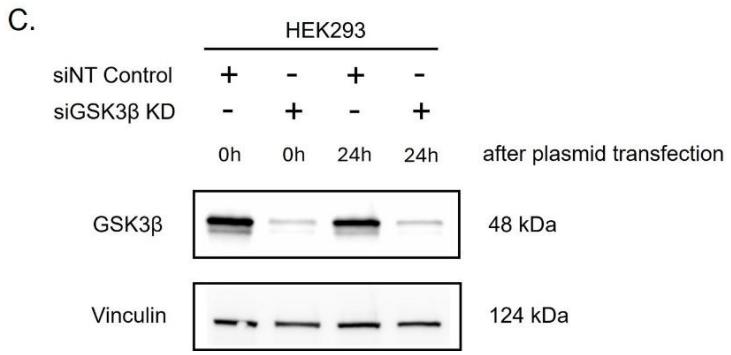
C.
HEK293
siNT Control + - + -
siGSK3β KD - + - +
0h 0h 24h 24h
after plasmid transfection
GSK3β
48 kDa
Vinculin
124 kDa

Figure 7. MFI of GFP signals measured in HEK293 live cells after knockdown of GSK3β with siRNA and irradiation. HEK293 cells were seeded and transfected with either siNT or siGSK3β. After siRNA knockdown, cells were transfected with or without the IFN-β-hygro reporter plasmid, then irradiated at 10 Gy. Flow cytometry was utilised to measure stimulation in IFN-β promoter activity in the form of GFP signals. At least 1000 cells were captured in each condition for analysis. MFI of GFP signals generated from the reporter plasmid at **(A)** 24 hours or **(B)** 72 hours post-radiation was quantified **(left panel)** together with representative histograms displaying distribution of MFI normalised to mode for qualitative comparison **(right panel)** of shifts in GFP signal. GFP+ control confirmed successful transfection of plasmids. **(C)** Successful knockdown of GSK3β was validated by western blotting. Data presented as mean ± standard deviation. N = 3, n = 3. Each circular symbol represents one technical replicate. Statistical significance assessed on biological replicates by two-way ANOVA with Bonferroni's multiple comparisons for comparison between siNT control and siGSK3β knockdown without or with plasmid respectively, or between radiation doses (0 Gy versus 10 Gy) for each condition. Paired t test for comparison between 0 Gy and 10 Gy for GFP+ transfection control. ns = non-significant, * $p < 0.05$, ** $p < 0.01$, *** $p < 0.001$, **** $p < 0.0001$. siNT, non-targeting siRNA; KD, knockdown; GFP, green fluorescent protein; w/o, without; w/, with; MFI, median fluorescence intensity.

One thing to note was that the MFI of siNT and siGSK3β samples without the reporter plasmid seemed to experience prominent increases after cells were irradiated for both 24 and 72 hours post-radiation, suggesting possible autofluorescence effects from dead cells that were captured in flow cytometry (**Figures 7A-B**). Overall, results from both approaches suggested that GSK3β repression did not greatly affect IFN-β production post-radiation.

3.4 Influence of vorinostat on cell viability and radiosensitisation

Before moving on to investigate whether HDAC inhibition promoted cGAS/STING pathway activation and eventual increase in IFN-β production post-radiation, Alamar blue assays were performed to determine whether the HDAC inhibitor vorinostat induced any effects on cell viability or radiosensitisation. HeLa cells were seeded and treated with a range of vorinostat concentrations, irradiated at 3 Gy or 5 Gy 4 hours after treatment according to the radiation doses that would be used in

the other experiments, and then subjected to fluorescence detection following addition of resazurin 7 days after irradiation.

HeLa cell viability was reduced in a dose-dependent manner at seeding densities of 500 cells/well and 750 cells/well (**Figures 8A-B**). In unirradiated samples (0 Gy), viability remained close to baseline levels at around 100% for concentrations lower than 500 nM, with the curve staying almost flat from 0 nM to the point representing 400 nM. At higher doses starting from around 800 nM, cell viability decreased gradually with steeper slopes, and near-complete loss of viability occurred at around 3.2 µM.

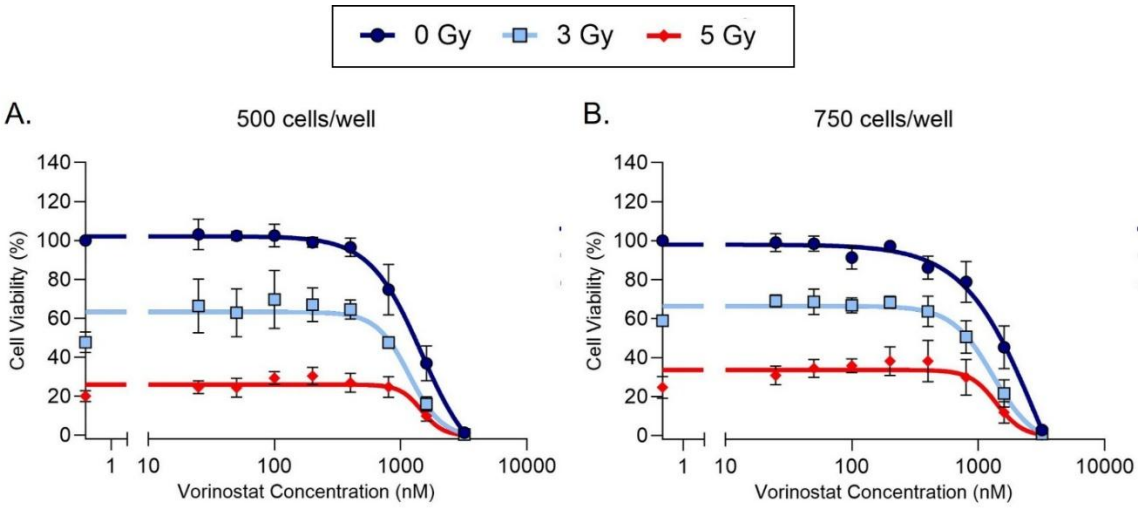

Figure 8. HeLa cell viability following treatment with HDAC inhibitor vorinostat of increasing concentrations and radiation doses. HeLa cells were seeded at **(A)** 500 cells/well or **(B)** 750 cells/well and treated with different concentrations of vorinostat (0, 25, 50, 100, 200, 400, 800, 1600 and 3200 nM)**,** followed by irradiation with 3 Gy or 5 Gy. Values obtained from fluorescence detection upon addition of resazurin to wells 7 days post-radiation were normalised to the vehicle control at 0 Gy (set as 100% cell viability) and the negative control (set as 0% cell viability). Data presented as mean ± standard deviation with x-axis plotted on a $\log_{10}$ scale. Three biological replicates (N = 3) with three technical replicates (n = 3). Absolute IC_{50} with 95% CI calculated together with extra sum-of-squares F test for statistical analysis. CI, confidence interval; IC_{50}, half maximal inhibitory concentration.

When combined with 3 Gy irradiation, baseline viability was reduced to around 50% (500 cells/well) or 60% (750 cells/well). This was further reduced to around 20% (500 cells/well) or 25% (750 cells/well) at 5 Gy radiation. Addition of vorinostat to irradiated samples further decreased cell viability across the tested concentration range, with trends similar to that observed in unirradiated samples (**Figures 8A-B**).

At 500 cells/well, the absolute IC_{50} of vorinostat at 0 Gy, 3 Gy and 5 Gy radiation was 1269 nM (95% CI [1144, 1409]), 1159 nM (95% CI [939, 1406]) and 1438 nM (95% CI [1127, 1764]) respectively. At 750 cells/well, the IC_{50} was 1532 nM (95% CI [1353, 1750]), 1233 nM (95% CI [1096, 1386]) and 1379 nM (95% CI [1001, 1754]) respectively. These indicated that the IC_{50} of vorinostat under unirradiated conditions was similar to that under irradiated conditions. The overall dose-response curves for irradiated and unirradiated samples were also of very similar shape (**Figures 8A-B**), and this was further supported by normalising the irradiated conditions to a baseline of 100% cell viability (**Supplementary Figure 2**). An extra sum-of-squares F test comparing models with shared versus separate $logIC_{50}$ values across 0 Gy, 3 Gy and 5 Gy radiation also found no significant differences (500 cells/well: $p = 0.2170$, 750 cells/well: $p = 0.5233$). Therefore, these results suggested that vorinostat is only more cytotoxic to HeLa cells at higher concentrations of above 800 nM, and that it did not provide evidence on significant radiosensitisation effects on cells.

3.5 Effects of vorinostat on cGAS binding to MN, IRF-3 nuclear translocation and chromatin acetylation post-radiation

To determine whether vorinostat enhanced cGAS/STING activation post-radiation, cGAS binding to MN and IRF-3 nuclear translocation were evaluated. Chromatin acetylation levels (H3K27ac) were also measured to ensure effective HDAC inhibition achieved by vorinostat treatment. HeLa cells were treated with different concentrations of vorinostat 4 hours before irradiation with 3 Gy or 5 Gy. Cells were harvested for IF 48 hours after irradiation to allow sufficient time for cell division and MN formation. Representative IF images of cGAS association with MN and nuclear IRF-3 levels in HeLa cells after 3 Gy radiation exposure and 200 nM vorinostat treatment were shown as a reference in **Figure 9A**.

3.5.1 MN formation induced by radiation

To assess whether radiation influenced genomic instability and induced MN formation, the number of MN was quantified and normalised to nuclei counts (**Supplementary Figure 3**), expressed as MN per 100 nuclei (**Figure 9B**). At 0 Gy, MN frequency was below 5 per 100 nuclei across all vorinostat concentrations. This frequency rose to around 11-20 MN per 100 nuclei at 3 Gy radiation, and further increased to around 18-38 MN per 100 nuclei at 5 Gy radiation. However, no clear vorinostat concentration-dependent trends or substantial differences in MN frequencies were observed at each radiation dose. Therefore, these data demonstrated that radiation effectively induced MN formation, consistent with its known genotoxic effects, but no obvious effects of vorinostat concentration on MN frequency were detected under these conditions.

3.5.2 H3K27ac acetylation induced by vorinostat

To determine whether vorinostat effectively increased histone acetylation, H3K27ac intensity was quantified at single-cell level across vorinostat concentrations and irradiation conditions (**Figure 9C**). Global nuclear acetylation levels increased in a concentration-dependent manner, with distributions showing clear upward shifts especially at higher concentrations of vorinostat (200 nM and 500 nM) compared to baseline (0 nM). At 0 Gy, median intensity values and intensity distribution rose progressively with vorinostat treatment, peaking at 500 nM. Similar concentration-dependent increases were observed at both 3 Gy and 5 Gy radiation, with the highest vorinostat concentrations consistently producing the strongest acetylation signals. Although only one biological replicate was available, statistical analysis performed on per-image mean intensities supported that acetylation levels at 200 nM and 500 nM were significantly higher compared to 0 nM at all radiation doses. Radiation itself did not consistently alter nuclear acetylation levels across vorinostat concentrations. These findings suggested effective HDAC inhibition and enhanced histone acetylation by vorinostat under the tested conditions.

Acetylation was also examined specifically in MN to evaluate whether vorinostat-induced acetylation extended to these structures (**Figure 9D**). Although MN were much fewer in number compared to nuclei, especially at 0 Gy, detectable H3K27ac signal was present. Similar to nuclear measurements, MN acetylation levels tended to increase at higher vorinostat concentrations, particularly at 500 nM. However, the data were more variable due to lower MN counts, and therefore provided only qualitative confirmation that acetylation also occurred in MN. Together, these results demonstrated that vorinostat robustly increased global histone acetylation and

possibly DNA relaxation in cells. This effect also extended to MN, albeit with greater variability.

3.5.3 cGAS binding to MN

In terms of cGAS binding to MN, the proportion of cGAS-positive MN among total MN was examined across vorinostat concentrations and irradiation conditions (**Figure 9E**). Specific MN and cGAS-positive MN counts were recorded in **Supplementary Figure 4**. At 0 Gy, cGAS binding to MN was around 44.4% at baseline (0 nM), and this remained similar at 50 nM (42.9%) or 200 nM (45.6%) vorinostat treatment. However, this percentage dropped to around 25.0% at 500 nM vorinostat. Irradiated cells, on the other hand, displayed higher proportions of cGAS-positive MN compared to unirradiated samples. At baseline level (0 nM), the percentage increased from 44.4% at 0 Gy to around 60.7% at 3 Gy radiation and around 60.4% at 5 Gy radiation, indicating the possibility of radiation playing a role in enhancing cGAS binding to MN. At 3 Gy radiation, the percentage of cGAS-positive MN at 50 nM vorinostat remained similar to that at 0 nM, with a percentage of around 59.8%. This then slightly increased at 200 nM to around 64.6%, but then dropped to around 55.0% at 500 nM. For 5 Gy radiation, the percentage at 50 nM increased to around 66.3% compared to 60.7% at 0 nM. This percentage then peaked at 200 nM at around 73.8%, before decreasing back to around 60.5% at 500 nM, which was similar to baseline level (60.4%). As similar trends were observed across all radiation doses, with the percentage of cGAS-positive MN increasing at 200 nM vorinostat but dropping at 500 nM, these observations suggested that irradiation increased the overall proportion of MN bound by cGAS. Vorinostat might also further promote cGAS recruitment at moderate concentrations

(200 nM), although this was based on a single experimental replicate and cannot be interpreted quantitatively.

3.5.4 IRF-3 nuclear translocation

Similar trends were observed for IRF-3 nuclear translocation as shown in **Figure 9F**. Nuclear IRF-3 intensity values measured at single-cell level revealed generally overlapping distributions across vorinostat concentrations, although modest shifts in the distributions were observed at intermediate concentrations. At 0 Gy, the median nuclear IRF-3 intensity remained close to baseline (0 nM) at 50 nM vorinostat, but appeared to increase slightly at 200 nM before returning towards baseline at 500 nM. The intensity distribution also showed the clearest upward shift at 200 nM vorinostat. A similar trend was observed at 3 Gy, with both the median intensity and upward shift in distribution peaking at 200 nM, and then declining back to around baseline level (0 nM) at 500 nM. At 5 Gy radiation, distributions showed less variation across vorinostat concentrations, with median intensities and overall distributions of all tested concentrations remaining relatively unchanged compared to baseline (0 nM). cGAMP- or poly(I:C)-treated positive controls produced more elongated and clear upward shifts in intensity distributions compared to vorinostat-treated samples, consistent with robust IRF-3 nuclear accumulation and confirming capability of the assay in detecting IRF-3 nuclear localisation. In terms of whether radiation augmented or synergised with vorinostat to promote more IRF-3 nuclear localisation, comparisons between radiation doses at each vorinostat concentration showed that distributions at 3 Gy and 5 Gy were either visually similar or sometimes even lower than that at 0 Gy across all concentrations. Overall, this suggested more IRF-3 nuclear translocation was potentially induced by cGAS binding and activation at moderate vorinostat concentrations like 200 nM, but such effects seemed to

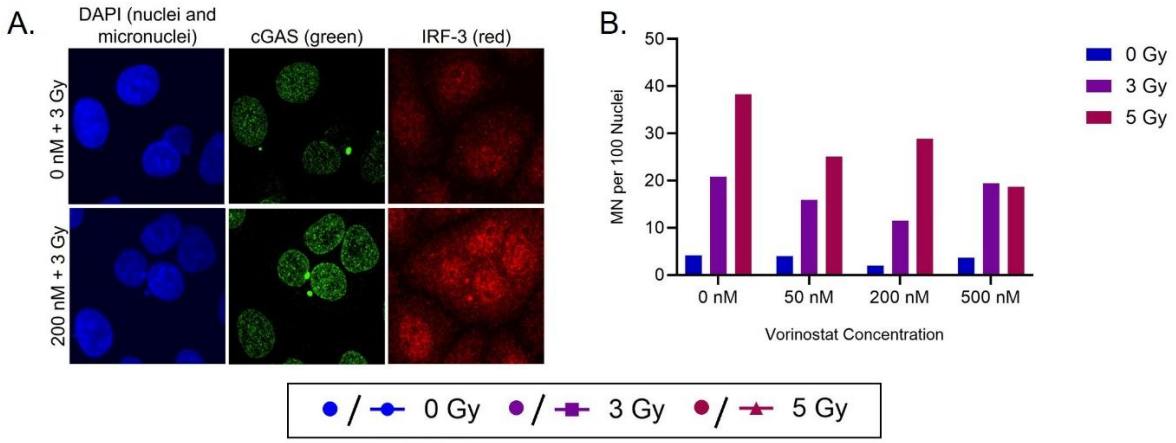

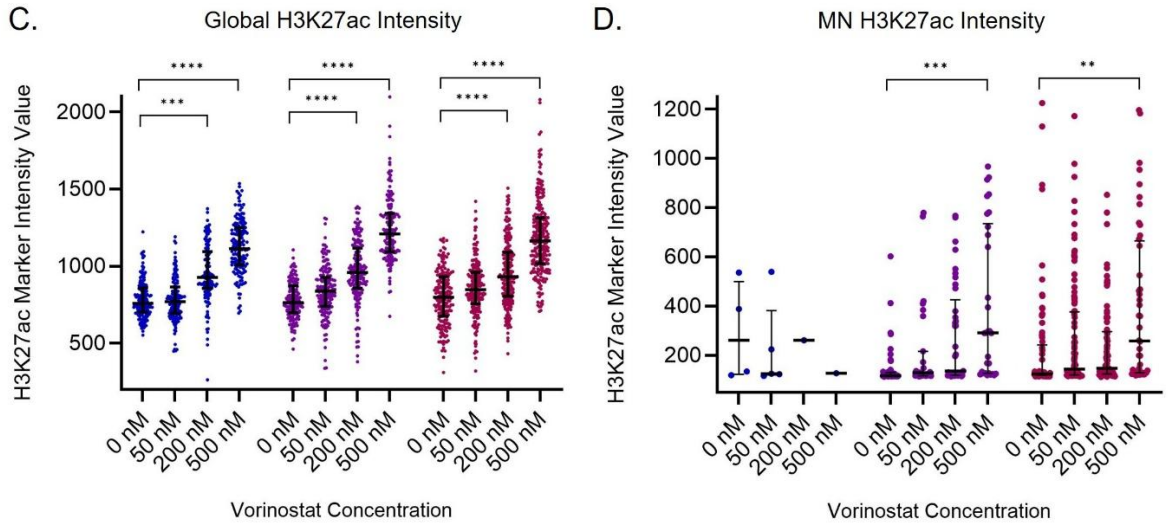

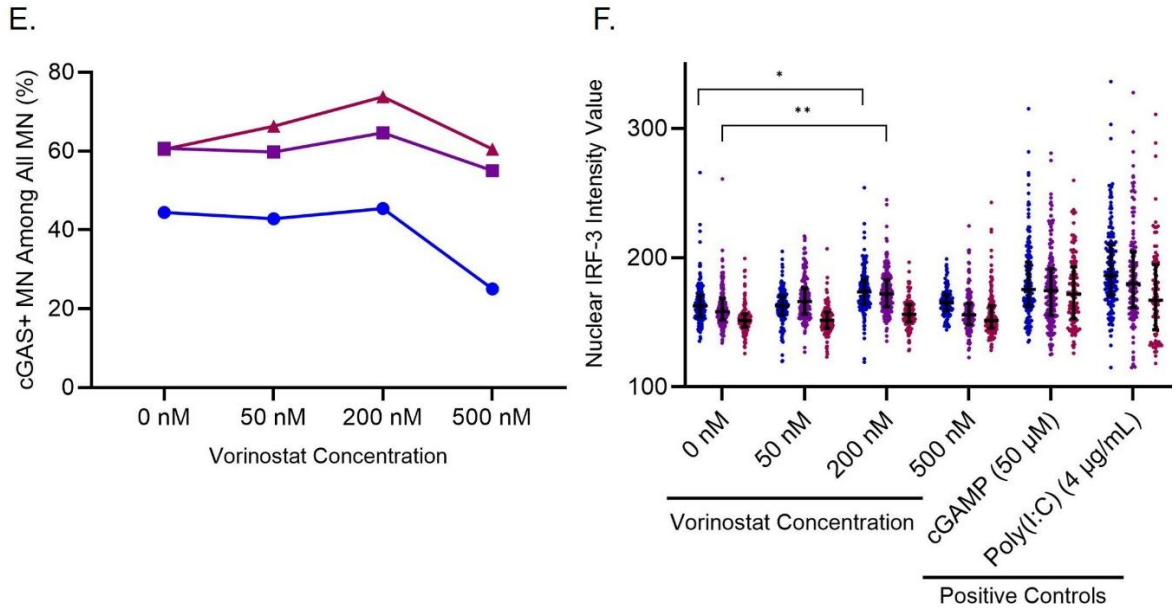

Significance	0 nM	50 nM	200 nM	500 nM
0 Gy vs 3 Gy	ns	ns	ns	ns
0 Gy vs 5 Gy	**	*	****	*

Figure 9. Evaluation of MN formation, chromatin acetylation and cGAS/STING pathway responses following HDAC inhibition and irradiation. HeLa cells were treated with vorinostat (0, 50, 200 or 500 nM), irradiated with 3 Gy or 5 Gy, and harvested for IF microscopy. **(A)** Representative IF images showing nuclei and MN (DAPI, blue), cGAS (green) association with MN and nuclear IRF-3 (red) levels in HeLa cells. Samples that were untreated or treated with 200 nM vorinostat after 3 Gy radiation exposure are shown as a reference. 4-8 images were captured per condition and used to quantify **(B)** MN formation presented as number of MN per 100 nuclei, **(C-D)** histone acetylation levels (represented by H3K27ac marker) in **(C)** cells globally or **(D)** MN specifically, **(E)** percentage of cGAS-positive MN among all MN and **(F)** IRF-3 nuclear localisation by measuring fluorescence intensity levels. cGAMP or poly(I:C)-treated positive controls were used as references for robust IRF-3 activation and nuclear localisation.

Data in **(B)** and **(E)** are presented as total numbers or percentages from combining all images for each condition due to low and varying MN count in some images. Underlying nuclei, MN and cGAS-positive MN count data used to derive **(B)** and **(E)** are shown in Supplementary Figures 3 and 4. Data in **(C)**, **(D)** and **(F)** are presented as single-cell fluorescence distributions with median ± interquartile range, and with each individual point representing a single cell quantified from IF images. Single experiment (N = 1) with one replicate measurement (n = 1). Statistical significance was assessed on per-image (4-8 images per condition) mean intensities by two-way ANOVA with Dunnett's multiple comparisons for comparison between vorinostat concentrations at each radiation dose and between radiation doses for each vorinostat concentration (summarised in table) to determine any additive or synergistic effects. ns = non-significant, * $p < 0.05$, ** $p < 0.01$, *** $p < 0.001$, **** $p < 0.0001$. MN, micronuclei; H3K27ac, histone H3 lysine 27 acetylation; IF, immunofluorescence.

diminish at higher concentrations like 500 nM. On the other hand, looking at the effects of radiation dose across treatments, there were generally no consistent synergistic effects between vorinostat and radiation.

Although the experiment only consisted of one biological replicate, per-image mean intensities (≥ 4 images per condition) were used for statistical testing to provide more evidence for the trends described. Results displayed that only 200 nM vorinostat significantly increased nuclear IRF-3 intensity compared to 0 nM at both 0 Gy and 3 Gy (0 Gy: $p = 0.0379$, 3 Gy: $p = 0.0012$) (**Figure 9F**). Differences between 0 nM and 50 nM or 500 nM were all non-significant. Similarly, no consistently significant positive interactions between radiation and vorinostat were detected (summarised in table).

Overall, vorinostat may modestly enhance IRF-3 nuclear accumulation at intermediate concentrations (200 nM), but this effect was not sustained at higher concentrations. Radiation also did not consistently amplify the effects of vorinostat on nuclear IRF-3 localisation, indicating no consistent synergy with vorinostat, although these conclusions were based on a single replicate and should be interpreted cautiously.

3.6 Responses from downstream signalling components of cGAS/STING pathway following HDAC inhibition post-radiation

To validate the results obtained from IF and further investigate whether HDAC inhibition promoted cGAS/STING pathway activation post-radiation that would in turn elevate activation of downstream signalling components, WB was performed on both whole-cell lysates and fractionated lysates of HeLa cells treated with different concentrations of vorinostat, and irradiated with 3 Gy or 5 Gy 4 hours after treatment. Cells were collected 48 hours after irradiation for whole-cell lysis or cell fractionation into cytoplasmic and nuclear fractions respectively.

Whole-cell lysates were analysed by WB to evaluate changes in levels of downstream signalling proteins not involved in nuclear translocation, such as p-TBK1 and p-STING. H3K27ac levels were also examined to determine whether histone acetylation increased with vorinostat concentration. Chemiluminescent images of the blots represented in **Figure 10A** showed that there were no clear differences in band intensity for p-TBK1 (84 kDa) across tested vorinostat concentrations (0-2 μM) and irradiation conditions. The cGAMP-treated positive control also did not seem to produce a stronger signal, indicating possible minimal

pathway activation under these conditions. For p-STING, faint bands were observed at around 40 kDa along with stronger off-target bands located at lower molecular weights (around 16 kDa and 22 kDa). Band intensity at the expected size of around 40 kDa did not vary consistently with treatment or irradiation, including the cGAMP-treated positive controls, and the presence of off-target bands suggested limited antibody specificity when blotting for this protein. In contrast, H3K27ac histone acetylation marker levels increased with vorinostat concentration, most evident at 1-2 μM, supporting effective HDAC inhibition by vorinostat. Notably, the cGAMP-treated positive controls showed lower H3K27ac levels compared to untreated or vorinostat-treated samples. Radiation also did not induce obvious effects on acetylation levels. Vinculin was used as loading control and confirmed comparable sample loading across different conditions. Overall, within the sensitivity of whole-cell WB, vorinostat increased histone acetylation but did not reveal clear changes in p-TBK1 or p-STING levels post-radiation.

To evaluate nuclear translocation of p-IRF-3 indicative of cGAS/STING pathway activation, as well as effects on total IRF-3 protein levels, fractionated lysates were probed in both cytoplasmic and nuclear fractions. This was also to provide a complementary biochemical approach to the single-cell readouts from IF. As shown in **Figures 10B-C**, vorinostat at all tested concentrations did not yield a consistent increase in nuclear p-IRF-3 levels (around 45-55 kDa) relative to the untreated control (0 nM). Total nuclear IRF-3 levels (around 50-55 kDa) showed only minor and inconsistent variations across concentrations. Cytoplasmic p-IRF-3 and total IRF-3 levels were broadly similar between conditions, mirroring what was observed in the nuclear fraction. Radiation exposure also did not seem to play a part in altering cytoplasmic or nuclear p-IRF-3 and total IRF-3 levels across vorinostat

concentrations. Vinculin and total histone H3 were utilised as cytoplasmic and nuclear loading controls respectively, and confirmed comparable sample loading across all conditions.

By contrast, cGAMP-treated positive controls produced a clear increase in band intensity for nuclear p-IRF-3 compared to all other samples. This was also accompanied by a modest increase in total nuclear IRF-3, consistent with canonical cGAS/STING pathway activation which included IRF-3 phosphorylation with nuclear translocation, as expected from a positive control. Similar observations were also made in cytoplasmic p-IRF-3 with a clear elevation of such levels, but total cytoplasmic IRF-3 levels were comparable to that of all other samples. Irradiation (3 Gy or 5 Gy) did not induce obvious differences in either cytoplasmic or nuclear p-IRF-3 and total IRF-3 readouts.

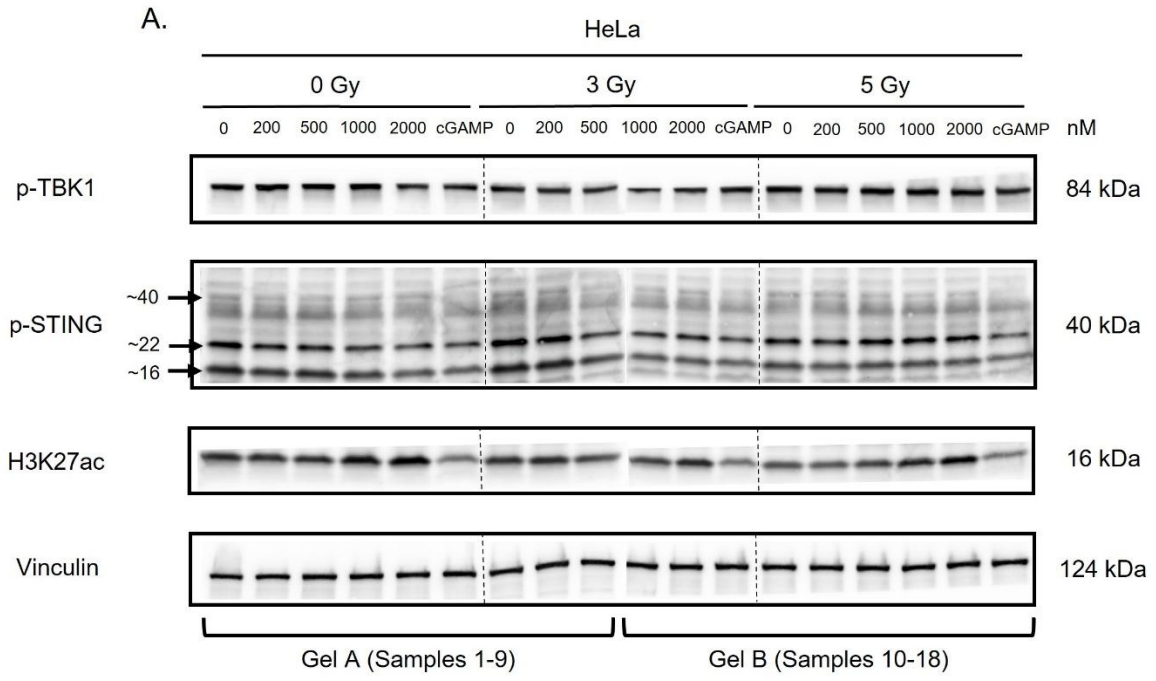

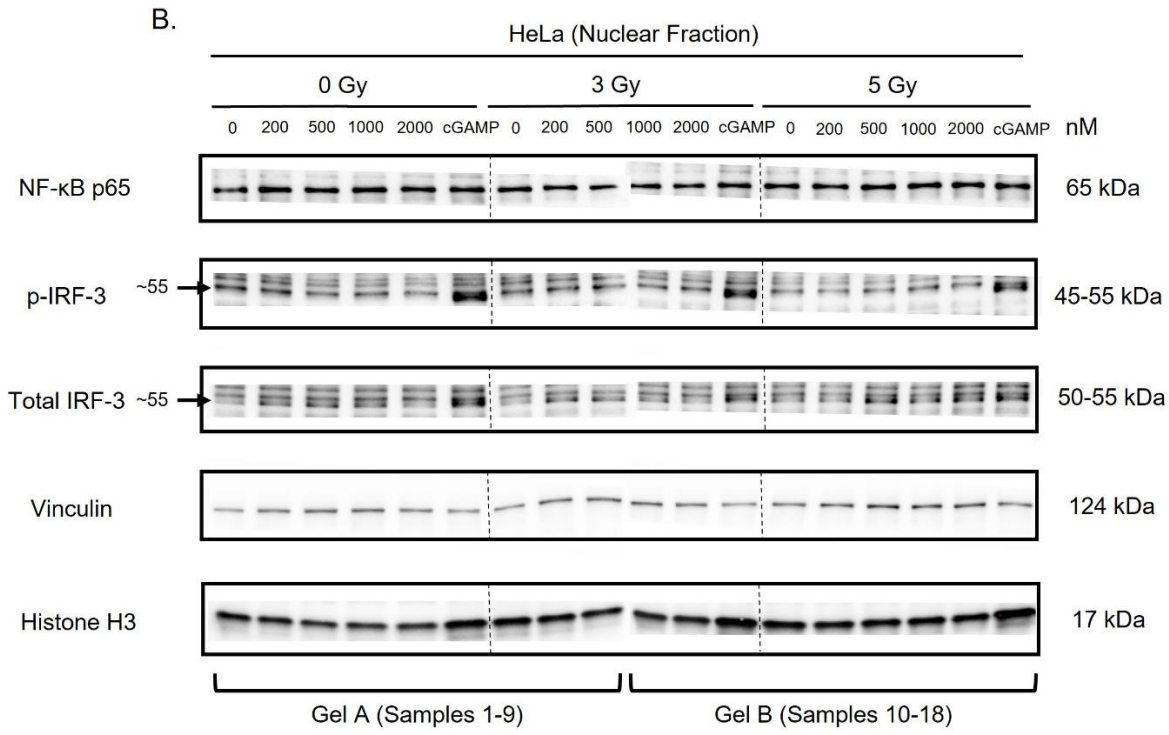
B.
HeLa (Nuclear Fraction)
0 Gy
3 Gy
5 Gy
0 200 500 1000 2000 cGAMP 0 200 500 1000 2000 cGAMP 0 200 500 1000 2000 cGAMP nM
NF-κB p65
65 kDa
p-IRF-3
~55
45-55 kDa
Total IRF-3
~55
50-55 kDa
Vinculin
124 kDa
Histone H3
17 kDa
Gel A (Samples 1-9)
Gel B (Samples 10-18)

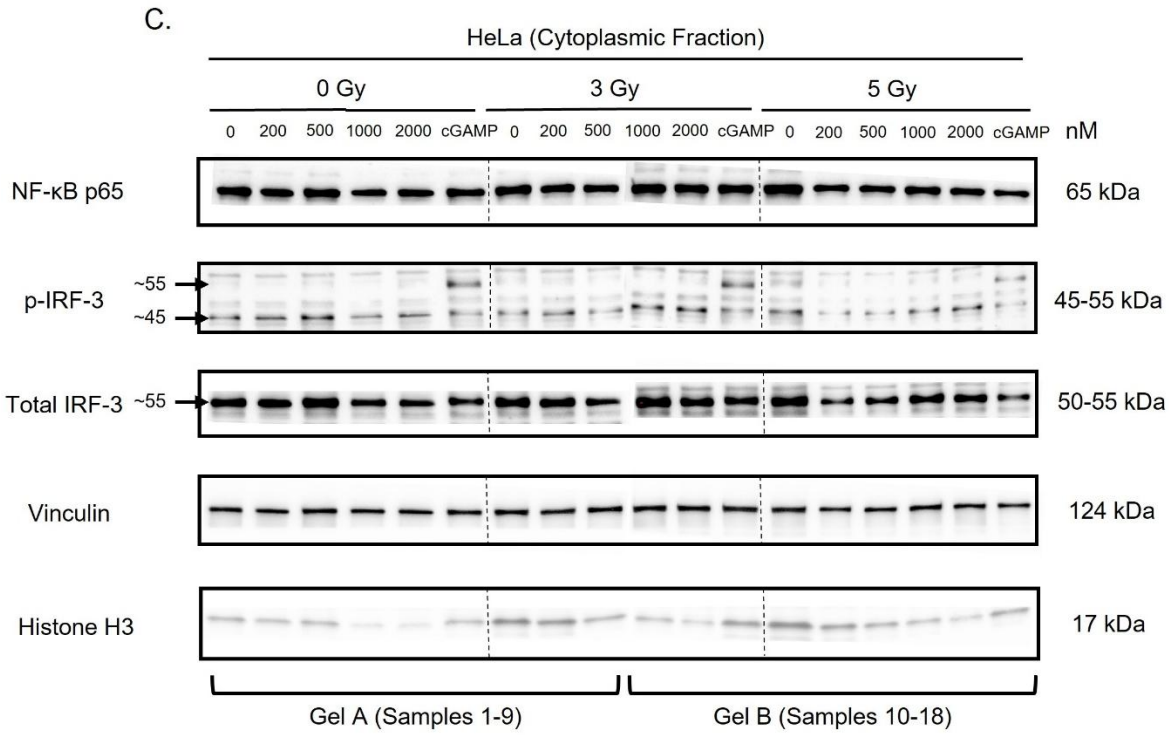
C.
HeLa (Cytoplasmic Fraction)
0 Gy
3 Gy
5 Gy
0 200 500 1000 2000 cGAMP 0 200 500 1000 2000 cGAMP 0 200 500 1000 2000 cGAMP nM
NF-κB p65
65 kDa
p-IRF-3
~55
~45
45-55 kDa
Total IRF-3
~55
50-55 kDa
Vinculin
124 kDa
Histone H3
17 kDa
Gel A (Samples 1-9)
Gel B (Samples 10-18)

Figure 10. Evaluation of responses from downstream signalling components of cGAS/STING pathway following HDAC inhibition and irradiation. HeLa cells were treated with vorinostat (0, 200, 500, 1000 and 2000 nM), irradiated with 3 Gy or 5 Gy, and harvested for cell fractionation and western blotting. cGAMP-treated samples were used as positive control for activation of STING and downstream signalling components. **(A)** Proteins that mainly stay in either the cytoplasm (p-TBK1, p-STING) or nucleus (H3K27ac) and are not involved in nuclear translocation were blotted using whole-cell lysates. Vinculin was used as loading control. Proteins involved in nuclear localisation (p-IRF-3, total IRF-3 and NF-κB) were blotted using **(B)** nuclear fraction extracts and **(C)** cytoplasmic fraction extracts obtained from cell fractionation. Vinculin and histone H3 were used as cytoplasmic and nuclear loading controls respectively. Single experiment (N = 1) with one replicate measurement (n = 1).

Western blot images were cropped for presentation clarity. Due to lane number constraints, samples were resolved across separate gels within each panel, with samples 1-9 and 10-18, as indicated in the figure, derived from different gels run under identical experimental conditions and imaged together using the same exposure settings. Blots for different target proteins were generated from separate gels and membranes and assembled for comparative presentation. Each gel included the appropriate loading control to verify even protein loading, with representative loading controls shown in this figure for clarity.

To further validate whether minimal changes were made to cGAS/STING activation following vorinostat treatment, fractionated lysates were further probed for NF-κB in cytoplasmic and nuclear fractions, which showed comparable band intensities at 65 kDa across all vorinostat concentrations and positive controls for all radiation doses in both fractions. Therefore, within the sensitivity of fractionated WB, vorinostat did not detectably enhance IRF-3 phosphorylation or nuclear translocation, nor did it promote NF-κB nuclear localisation post-radiation.

4. Discussion

The potential of inducing anti-tumour immunity after radiotherapy, especially type I IFN production that can facilitate immune cell recruitment, has recently been explored in different cancer contexts to enhance therapeutic efficacy. (100–102) The cGAS/STING pathway is generally activated by cytosolic DNA produced as a result of radiation-induced DNA damage. However, following irradiation, damaged chromosomal fragments may become sequestered within MN in the cytoplasm away from the main nucleus. Highly condensed nucleosomal DNA in MN can limit effective cGAS activation and consequently reduce downstream type I IFN production. This study thus evaluated whether modulation of GSK3β or HDAC activity could enhance radiation-induced IFN-β production. Here we discuss the biological and methodological factors that may explain the limited effects observed.

4.1 Differential effects of LY2090314 and 9-ING-41 on GSK3β inhibition and radiosensitisation

The two GSK3β inhibitors LY2090314 and 9-ING-41 differed in their effects on radiosensitisation as measured by the 7-day Alamar blue assays, which were not subject to GFP fluorescence interference observed with 9-ING-41 in flow cytometric analysis. Although both inhibitors decreased cell viability in a concentration-dependent manner, LY2090314 reduced cell viability further when in combination with irradiation, consistent with radiosensitisation, while 9-ING-41 had no such effect. This divergence was notable given that both drugs have been reported to be ATP-competitive inhibitors of GSK3β and are currently being tested in early-phase clinical trials. (86,87,89)

Apart from playing a major role in the Wnt/β-catenin pathway, GSK3β has also been shown to play a role in DNA damage response (DDR) and different repair pathways, such as base excision repair and DSB repair, by regulating different key proteins important for DNA repair, such as tumor protein p53 binding protein 1 and Rad3-related protein. GSK-3β also phosphorylated targets to trigger proteasomal degradation and promote activation of NF-κB activity for evading apoptosis. (82,83,103–106) These supported the idea that sufficiently deep GSK3β inhibition possessed potential in inducing radiosensitisation effects by impeding DNA damage repair.

While both LY2090314 and 9-ING-41 inhibited GSK3β, one of the factors that might have contributed to their differences in radiosensitisation was the possibility of differences in functional target engagement. Even though both drugs targeted GSK3β, their potency, selectivity and off-target effects might not be identical. LY2090314 was developed to modulate β-catenin levels and Wnt signalling in cancer. It has been shown to promote stabilisation of β-catenin, which is usually degraded after being phosphorylated by GSK3β, as well as elevate the expression of axis inhibition protein 2, a Wnt responsive gene and marker of pathway activation in a panel of melanoma and neuroblastoma cell lines. (84,85) These served as pharmacodynamic evidence of deep GSK3β inhibition. On the other hand, while 9-ING-41 demonstrated the ability to suppress GSK3β activity in neuroblastoma cells by downregulating phospho-glycogen synthase, a direct downstream target of GSK3β, (107) it inhibited validated targets of GSK3β action to a lesser extent, including the inability in stabilising β-catenin. Moreover, examination of in vitro sensitivity of over 100 different kinases to 9-ING-41 showed that 22 kinases were inhibited at over 50% at micromolar concentrations, with equivalent potent action

against GSK3β and other kinases like proto-oncogene serine/threonine-protein kinases 1 and 3. (108) While both inhibitors might have displayed good potency for GSK3β, the extent and duration of GSK3β inhibition achieved by LY2090314 was sufficient to impact processes that modulated responses to radiation, with robust pharmacodynamic evidence pointing towards stronger on-target cellular pathway engagement, and thus supporting a deeper functional inhibition narrative that drove modest radiosensitisation. 9-ING-41, however, seemed to induce shallower or shorter-lived GSK3β inhibition under the tested doses and timing, as reflected by weak inhibition of validated GSK3β targets like β-catenin. This was possibly due to its off-target profile introducing compensatory signalling via pathways involving different kinases that masked GSK3β-mediated radiosensitisation, thus yielding no net effect. Therefore, the differences in cellular pharmacology and possible inhibitor-specific effects on cell-cycle or survival programmes likely affected the extent or duration of functional GSK3β inhibition and hence radiosensitisation.

An important methodological consideration in this study is the use of different radiation doses across assays, as well as the choice of viability readout. A lower radiation dose (3 Gy) was used for cell viability and radiosensitisation assays to ensure the maintenance of a sufficient number of viable cells for assessment of dose-response relationships. This could also minimise excessive cytotoxicity caused by radiation-induced DNA damage that could confound interpretation of inhibitors' effects. In contrast, a higher dose (10 Gy) was employed in IFN-β reporter assays to ensure robust induction of DNA damage and maximise detectability of downstream IFN signalling, which may often be transient in tumour cell models. Therefore, comparisons across assays using different radiation doses should be

interpreted qualitatively rather than quantitatively, as dose-dependent non-linear effects may influence both cell survival and signalling outcomes.

In this study, cell viability was assessed using the Alamar blue assay, which measures cellular metabolic activity representative of viable cell number and provides a short-term cell viability readout at the point of measurement, while enabling efficient screening across multiple inhibitor concentrations and radiation doses within a short period of time. While suitable for identifying relative changes in viability and radiosensitisation trends, the Alamar blue assay does not assess long-term reproductive survival, for which clonogenic assays remain the gold standard. Furthermore, Alamar blue measurements performed after a prolonged culture period may reflect cumulative effects of radiation and inhibitor treatment on metabolic viability, whereas IFN signalling and reporter assays were conducted within shorter timeframes (up to 72 hours) to capture early pathway activation. Differences in assay duration and biological endpoints may therefore contribute to discrepancies between viability and signalling readouts, which should be taken into consideration when interpreting the results. Consequently, radiosensitisation effects inferred from Alamar blue assays may underestimate delayed or clonogenically lethal radiation damage, and conclusions regarding radiation response should be interpreted in the context of short-term metabolic viability rather than long-term cell survival in this study.

4.2 Absence of increase in IFN-β levels post-radiation upon GSK3β repression

One of the main approaches investigated in this study was whether inhibiting GSK3β could modulate IFN-β production post-radiation, with GSK3β being implicated in NF-κB regulation that is upstream of type I IFN production. The experimental results, however, did not support this hypothesis.

4.2.1 Assay caveats

Although increases in MFI were detected in samples treated with 9-ING-41 and transfected with the reporter plasmid, especially at 0 Gy radiation, significant MFI elevation was also detected in 9-ING-41-treated samples even when the fluorescence-producing reporter plasmid was absent across all tested timepoints and radiation doses. Therefore, it was believed that 9-ING-41 itself possessed fluorescence effects that might interfere with the GFP signals that would reflect true promoter activation. The increase in MFI in 9-ING-41-treated and transfected samples thus might be explained by detection of these fluorescence effects, rather than actual increase in IFN-β production.

Another factor that complicated the interpretation was the experimental concentration used for 9-ING-41. The chosen concentration of 20 μM, although reported to achieve near-complete inhibition of GSK3β, (108) was very close to cytotoxic levels as observed in the cell viability assays, raising the possibility that observed outcomes reflected toxicity or extensive cell death rather than specific pathway modulation. Although gating strategies were employed to exclude dead cells and ensure sufficient number of live cells for analysis, the possible influence of cytotoxicity on IFN-β production independent of GSK3β inhibition still deemed 9-

ING-41 a suboptimal inhibitor for measuring the effect of GSK3β inhibition on type I IFN levels.

An additional caveat of the experimental setup is that effective functional GSK3β inhibition was not directly validated under the experimental conditions used to assess IFN-β production. While pharmacological inhibition and siRNA-mediated knockdown of GSK3β were employed, no downstream readouts were included to confirm suppression of GSK3β activity at the timepoints relevant to irradiation and IFN-β measurement. The absence of increased IFN-β production following GSK3β repression thus cannot be definitively attributed to an actual lack of involvement of GSK3β in regulating radiation-induced type I IFN responses, as the possibility of insufficient functional inhibition cannot be excluded in this experimental setting. In future studies, the inclusion of functional validation controls, such as assessment of established downstream targets of GSK3β like stabilisation of β-catenin with Western blotting, would be important to confirm effective GSK3β inhibition and facilitate more appropriate interpretation of any observed IFN-β level changes.

4.2.2 Pharmacological validation with LY2090314

On the other hand, LY2090314-treated samples displayed more reliable results. While no significant increases in MFI were detected following LY2090314 treatment in cells transfected with the reporter plasmid, no changes were seen either when cells were treated with LY2090314 without the reporter plasmid, indicating that the inhibitor itself was less likely to possess fluorescence effects that might skew interpretation. With a reported IC_{50} of 0.9 nM and ability to significantly stabilise β-catenin at 20-25 nM without greatly altering cell viability, (85,108) the experimental concentration of 40 nM served as an ideal level for investigating any changes in IFN-β production post-radiation without creating prominent cytotoxic effects, as

confirmed by the Alamar blue assays. Therefore, the final results suggested that neither LY2090314 nor 9-ING-41 induced measurable increases in IFN-β promoter activity in HEK293 cells post-radiation.

4.2.3 Genetic validation with siGSK3β knockdown

As the utilisation of GFP-expressing reporter plasmids would mean that any use of possibly fluorescent drugs would be a less reliable strategy to determine the correct GFP output, this confounding effect highlighted a general challenge in drug screening studies that rely on fluorescent reporters. Therefore, siRNA knockdown was then used to exclude these fluorescence artefacts and validate the pharmacological findings obtained from GSK3β repression by the two inhibitors. siRNA knockdown of GSK3β confirmed the observation that GSK3β repression did not lead to significant increases in IFN-β production following irradiation by comparing the siNT control with siGSK3β knockdown samples transfected with the plasmid. These results supported the conclusion that GSK3β repression alone was insufficient to enhance IFN-β signalling in HEK293 cells post-radiation.

One technical consideration in these experiments was the potential for autofluorescence from dead or dying cells, which might increase in number upon exposure to radiation and could mimic GFP reporter signals in flow cytometry. Although gating strategies like the live cell gate were employed to exclude dead cells, some autofluorescence was still detectable, which was most clearly reflected in the non-transfected siNT or siGSK3β controls. Importantly, however, this did not alter the overall conclusion, as there was no consistent increase in IFN-β signalling even when viable cells were isolated for analysis.

4.2.4 Mechanistic and model context for minimal changes in IFN-β production

The lack of changes in IFN-β production post-radiation after GSK3β repression raised broader questions on the context-dependent role of GSK3β in cancer cell survival and potentially type I IFN immune signalling. There has been an ongoing debate on the complex functions of GSK3β, which allows it to act as a tumour promoter or tumour suppressor under different conditions and contexts. While the directionality of action for GSK3β seemed to rely on the dominant downstream axis, another determinant that might explain the contradictory actions of GSK3β in cancer might be related to localisation, more specifically, an imbalance between pro-apoptotic cytoplasmic GSK3β and oncogenic nuclear GSK3β. It was proposed mechanistically that nuclear GSK3β promoted nuclear localisation of NF-κB, therefore enhancing transcription of pro-survival genes and thus acting as a tumour promoter, while localisation to the cytoplasm could induce pro-apoptotic effects as a tumour suppressor. (66,109)

Crucially, none of the pathways by themselves seem to supply all the input needed to activate the *IFNB1* enhanceosome responsible for promoting IFN-β transcription, which requires coincident IRF-3/7, NF-κB and activating protein-1 (AP-1). (110–112) While NF-κB was shown to be important for early IFN-β upregulation, it is IRF-3 that is the obligate driver for IFN-β upregulation, with NF-κB and AP-1 as co-activators. (112) Given these context-dependent roles and subcellular localisation effects, shifting GSK3β alone may not supply the IRF-3-centred inputs required for *IFNB1* enhanceosome activation, and thus may not translate into greater type I IFN induction, possibly due to the limitations set by MN, which aligned with the unchanged IFN-β readouts observed from the experiments in this study.

These considerations were also influenced by the use of HEK293, a human embryonic kidney non-tumour cell line that is not representative of cancer signalling states. It was previously reported that relative to cancer cell lines like HCT116 human colon cancer cells, HEK293 showed lower total GSK3β and much higher levels of inactive GSK3β, implying a baseline attenuation of GSK3β activity. (77) In this context, HEK293 exhibited attenuated baseline GSK3β activity, which may reduce headroom to detect effects from further repression in this model.

Therefore, while prior studies supported GSK3β as either pro-survival or tumour-suppressive depending on the context, the data in this study contrasted with the notion that modulating GSK3β alone is sufficient to raise IFN-β after irradiation. Instead, they support a model in which IRF-3-centred enhanceosome constraints and negative feedback highly influence the output.

4.2.5 Compensatory mechanisms for maintaining IFN levels

Given GSK3β's context-dependent roles and the attenuated GSK3β state in HEK293 cells, a weak IR-driven input may be insufficient to yield a measurable change in IFN-β output under our conditions. Thus, the possibility of compensatory mechanisms such as negative feedback and parallel pathway inputs that keep this output flat is also worth considering. The negative feedback loop involves a plethora of proteins, including 2'-5'-oligoadenylate synthase-like protein 1 (OASL1) and tripartite motif-containing protein 21 (TRIM21), to limit the extent and duration of type I IFN responses, preventing chronic and excessive inflammation. OASL1 is an interferon-stimulated gene, with its protein form reported to inhibit translation of IRF-7, and thus negatively regulated type I IFN production in the context of a viral infection. (113–115) In the context of cancer, this regulation was supported by OASL1 negatively regulating type I IFN production similar to that of viral infection

upon implantation of lung tumours in mouse models. Tumour-challenged OASL1-deficient mice expressed increased levels of type I IFN and IRF-7 in the tumours compared to wildtype mice. OASL-1 deficient mice that underwent cisplatin chemotherapy and radiotherapy also produced more type I IFNs in their tumours compared to those that did not receive any form of therapy. (116,117) TRIM21 protein is also stimulated by type I IFNs, and was found to inhibit type I IFN production by promoting ubiquitination and subsequent proteasomal degradation of IRFs like IRF-3. (113,118–120) Therefore, even if GSK3β repression produced modest gains in IFN-β production, inducible feedback may attenuate these increases at the timepoints measured, helping to explain the small net change observed.

On the other hand, partially overlapping kinase inputs – TBK1 and inhibitor of nuclear factor kappa-B kinase subunit epsilon – act redundantly to support mainly IRF-3/7 and NF-κB activation in the *IFNB1* enhanceosome. (121–123) If one route is weak or perturbed, the other may thus be able to compensate sufficiently to preserve activation levels, preventing big drops in type I IFN production. Accordingly, altering a modulatory node like GSK3β may not, on its own, produce a large IFN-β response in this model, highlighting the value of combinatorial or timing-dependent approaches to reveal any latent effects.

4.2.6 Conclusion for GSK3β repression approach

Overall, across pharmacological and genetic perturbations, GSK3β repression did not enhance IFN-β post-radiation in HEK293 cells. Accounting for assay caveats, possible explanations for the results observed include the complex role of GSK3β in cancer and the limits faced in fulfilling the requirements for *IFNB1* enhanceosome activation, with any modest changes further constrained by IFN-induced negative

feedback and parallel pathway inputs. Together, these findings suggested that GSK3β is unlikely to be a productive lever for boosting radiation-induced type I IFN in this setting, directing attention to alternative entry points.

4.3 Effects of HDAC inhibition on cGAS/STING pathway activation post-radiation

Given the neutral IFN-β outcome with GSK3β, the second strategy explored in this study focused on modulating chromatin structure to facilitate cGAS/STING activation within radiation-induced MN. The rationale for this approach derived from accumulating evidence that MN, although capable of recruiting cGAS, fail to robustly activate the pathway due to their highly condensed nucleosomal DNA. HDAC inhibition with vorinostat was therefore used to increase histone acetylation, thereby relaxing chromatin in the expectation that this would improve cGAS access to DNA and enhance downstream IFN signalling.

Results from IF showed that vorinostat treatment produced clear concentration-dependent increases in acetylation at both global and micronuclear levels, and moderate vorinostat concentrations (200 nM) were associated with an increased frequency of cGAS-positive MN and enhanced nuclear localisation of IRF-3 following irradiation. However, the effect was not sustained at higher concentrations (500 nM), and there were no additive or synergistic effects between vorinostat and radiation. In addition to this, these findings were not corroborated by WB.

4.3.1 Differences in observations between IF and WB

Several explanations may account for the above discrepancies. The divergent results between IF and WB might reflect fundamental methodological differences.

IF enables single-cell resolution and can detect subpopulation-specific or spatially restricted effects, such as acetylation confined to MN or nuclear accumulation of IRF-3 in cells. WB, by contrast, measures overall signals across entire populations or cellular fractions, potentially diluting subtle effects and masking heterogeneity. Thus, the apparent induction of IRF-3 translocation observed in IF may represent a minority of responding cells whose contribution was lost in bulk biochemical analysis like WB. This interpretation is consistent with pharmacodynamic work performed on HDAC inhibitors showing that single-cell assays captured marked cell-to-cell heterogeneity in acetylation that bulk lysates could obscure. (124) Method comparisons also noted that IF or other immunocytochemistry approaches are more single-cell sensitive, whereas WB, despite having high selectivity, is population-averaging. (125) In addition to that, fractionation purity may also play a role, as minor nuclear-cytoplasmic cross-contamination can dilute nuclear IRF-3 below WB detection, hence producing the discrepancy in results.

4.3.2 Possible mechanisms for decreases in cGAS-positive MN and nuclear IRF-3 at higher vorinostat concentrations

With the differences in cGAS-positive MN and nuclear IRF-3 levels especially between 200 nM and 500 nM vorinostat, the dose-dependent pattern observed suggested that vorinostat's on-target effects may operate within a narrow therapeutic window, with off-target effects, especially on substrates beyond histones, becoming more prominent at higher vorinostat concentrations. At 200 nM, chromatin relaxation may sufficiently expose DNA to cGAS without broadly disrupting nuclear organisation. (95) However, at 500 nM, excessive acetylation could destabilise chromatin to the point of impairing nuclear architecture, leading to cytotoxic stress responses that may counteract cGAS/STING activation. Vorinostat

at concentrations above 1.25 μM was reported to slow down replication forks, induce DSBs and oxidative DNA lesions in a number of cancer cell lines, including breast, colon and acute myeloid leukaemia cell lines. G2-M cell cycle arrest and eventually apoptosis also occurred after the vorinostat-induced DNA damage. (126–129) In addition to that, vorinostat is capable of broadly acetylating non-histone proteins that are associated with cell cycle arrest and apoptosis, such as p53 and α-tubulin. (129,130) The accumulation of acetylated proteins may thus interfere with critical cellular processes involved in functions like cell cycle regulation, angiogenesis and DNA repair independent of immune signalling.

All of the above may collectively impose cytotoxic stress at higher concentrations of vorinostat that can blunt downstream signalling readouts. Therefore, the decrease in IRF-3 nuclear translocation at 500 nM may reflect stress-induced signalling collapse rather than a direct suppression of cGAS activity. Higher concentrations like 500 nM might also reduce the number of cells that reach mitosis and form MN by the 48 hours post-radiation timepoint due to G2-M cell cycle arrest or apoptosis, possibly leading to fewer MN formed and poorer cGAS recruitment that ultimately resulted in fewer cGAS-positive MN at the measurement point.

Another possible explanation for the differences in responses between vorinostat concentrations is through a mix of direct post-translational modifications (PTMs), effects on regulators and MN chromatin context that may alter cGAS activity. In terms of PTMs, enforced cGAS acetylation on either Lys384, Lys394, or Lys414 was reported to contribute to keeping cGAS inactive, blocking DNA binding and enzymatic activity that may in turn suppress downstream IFN signalling. On the other hand, lysine acetyltransferases (KATs) like KAT5 were found to acetylate Lys47/Lys56/Lys62/Lys83 residues located in the N-terminal unstructured region

that is necessary for DNA binding in cGAS, leading to increased cGAS association with DNA to promote cGAS activation. (131–136) Thus, depending on the distinct acetylation sites, acetylation of cGAS could either positively or negatively regulate cGAS activation. By preventing deacetylation, vorinostat may potentially shift the balance towards whichever acetylation state is present. Depending on cellular context and available KATs, hyperacetylation could lock cGAS in an inhibitory state even while global histone acetylation rises, thus possibly explaining reduced IRF-3 translocation at 500 nM.

In terms of impacts on regulators, vorinostat may also induce effects related to acetylation on cGAS/STING regulators and kinases. It was suggested that HDAC3 and HDAC9 directly deacetylated TBK1 at Lys241 and Lys692, and hence activated TBK1 to promote IRF-3-activated transcription. (137–139) As a pan-HDAC inhibitor, vorinostat may therefore dampen TBK1 activity upstream of IRF-3 by more extensively inhibiting both HDAC3 and HDAC9 at higher concentrations, potentially leading to the decrease in nuclear IRF-3 at 500 nM.

In terms of MN chromatin context, it was shown that MN with active transcription pre-rupture prevented cGAS localisation. (140) As vorinostat can increase histone acetylation and generally elevate transcriptional activity, MN may be more biased towards a transcriptionally active state pre-rupture at higher vorinostat concentrations, reducing cGAS recruitment post-rupture and thus yielding a smaller fraction of cGAS-positive MN even as global acetylation rose.

In addition to that, time-dependent effects may play a role. The single 48-hour snapshot may not reflect the entire kinetics of the cGAS/STING axis. IRF-3 nuclear translocation is often transient, and cGAS recruitment to MN may also be short-lived

across the population depending on when individual cells complete mitosis and when MN rupture. A higher vorinostat concentration like 500 nM can plausibly generate an earlier, larger pulse of cGAS/STING activity that may then trigger negative feedback sooner as mentioned previously with proteins like TRIM21. (113,118–120) Thus, by 48 hours post-radiation, the pathway may seem to yield lower nuclear IRF-3 and a smaller fraction of cGAS-positive MN in that snapshot as their peak activity might have already passed. In contrast, 200 nM may produce a milder, more sustained response whose peak overlapped the 48-hour readout, hence making both IRF-3 and cGAS-positive MN more evident at that timepoint.

4.3.3 Possible mechanisms for lower nuclear IRF-3 following radiation at higher doses

At 5 Gy, nuclear IRF-3 levels were consistently lower than at 0 or 3 Gy across vorinostat concentrations, despite the fraction of cGAS-positive MN remaining similar to that at 3 Gy. This decoupling of cGAS binding from downstream IRF-3 output is consistent with recent reports that MN are not uniformly productive for cGAS signalling. cGAS can localise to MN without robust activation (cGAMP synthesis) depending on MN rupture status, chromatin or transcriptional state of MN and the handling of DNA damage. (63,140) As cGAS binding does not equal cGAS activation, 5 Gy radiation may potentially create modifications in MN that are inhibitory for cGAS activation to explain why comparable fractions of cGAS-positive MN could nonetheless yield lower IRF-3 levels. On the other hand, if 5 Gy radiation did cause similar or even higher levels of cGAS activation compared to 0 Gy or 3 Gy, this may be explained by the time-dependent effect as mentioned previously, where potential larger cGAS/STING pulse caused by higher doses of radiation can

induce earlier negative feedback that dampens nuclear IRF-3 levels before the measured timepoint.

A second plausible explanation for this observation is related to the trafficking of STING from the endoplasmic reticulum (ER) to the Golgi apparatus. After DNA binding, STING needs to translocate from the ER to perinuclear compartments including the Golgi to activate downstream signalling. (141) DNA damage was reported to perturb Golgi structure and vesicular transport through induction of Golgi dispersal, blocking ER-to-Golgi traffic and thus hindering STING-dependent signalling events that include TBK1 and IRF-3 phosphorylation and ultimately induction of IFN-β. (142,143) Therefore, it is possible that higher genotoxic stress caused by higher radiation doses like 5 Gy may further compromise this transit, eventually resulting in lower nuclear IRF-3 levels due to reduced signalling downstream of STING.

4.3.4 Assay caveats and limitations

Apart from assay sensitivity in single-cell measurements and fractionation purity, a few other limitations also presented more challenges in interpreting the observed data thoroughly. Firstly, IF was only able to measure cGAS binding but not activation. While cGAS activation is a crucial step for downstream signalling as mentioned previously, cGAS binding observed in this study cannot be definitively correlated to the changes in IRF-3 levels. Quantification of cGAS activation will be needed by techniques like enzyme-linked immunosorbent assay (ELISA) to further confirm true activation of the pathway.

In terms of interpreting histone acetylation data in WB, it is important to consider the use of appropriate histone loading controls. While total histone H3 was included in

the nuclear and cytoplasmic fractions as a marker of successful fractionation and as a loading control for the nuclear fraction, no corresponding total histone H3 control was included for the whole-cell lysate samples, and acetylation signals were not quantitatively normalised to total histone levels. As histone acetylation markers like H3K27ac are interpreted relative to total histone abundance, the absence of consistent normalisation may limit the ability to determine whether observed differences reflect actual changes in acetylation state or variability in histone content or extraction efficiency. This consideration is particularly relevant for fractionation-based assays used in this study, where chromatin recovery may differ between conditions. Although total histone H3 levels are generally expected to remain stable across conditions, inclusion and quantitative use of total histone H3 loading controls across all fractions in future experiments would allow more robust normalisation and strengthen conclusions regarding chromatin acetylation changes following HDAC inhibition and irradiation.

Interpretation of p-STING signals in WB also presented limitations related to antibody specificity. Multiple bands were detected using the p-STING antibody, which may possibly reflect non-specific binding or cross-reactivity with unrelated proteins. In the absence of specificity validation, it is difficult to definitively attribute individual bands to real p-STING signals. Inclusion of appropriate specificity controls, such as STING knockdown or knockout samples that would show weakened or loss of bands if there is minimal non-specific binding, would be important in future studies to validate antibody specificity and enable more confident interpretation of p-STING dynamics following irradiation and HDAC modulation.

Furthermore, this study was limited by one biological replicate at a single timepoint (48 hours post-radiation) for several vorinostat and irradiation conditions, so

variance and effect sizes were uncertain. In addition to this, MN scoring was partly operator-dependent with much difficulty in assessing MN rupture and transcriptional state, and may thus skew the analysis for responses downstream of cGAS binding. Finally, pan-HDAC inhibitors like vorinostat exert global chromatin acetylation effects that can co-vary with MN-local effects. The experimental readouts may therefore mix MN-local effects that this study would like to investigate with global dose-dependent changes, making it challenging to distinguish between global induction effects and subtle MN-restricted signals.

As discussed later in the context of future directions, complementary approaches such as quantitative PCR-based assessment of IFN-β or IFN-stimulated gene transcription, as well as ELISA-based quantification of secreted IFN-β protein across multiple timepoints, may provide greater sensitivity and more detailed measurements for detecting transient or delayed IFN signalling responses.

4.3.5 Conclusion for HDAC inhibition approach

Taken together, these results suggest that while HDAC inhibition may be capable of remodelling chromatin and modestly influence cGAS recruitment and IRF-3 localisation, the effects are subtle, dose-dependent and not consistently translated into robust IFN-β production. The discrepancy between promising biochemical evidence (increased acetylation) and limited functional outcomes (lack of cGAS/STING/IFN-β pathway induction) highlighted the challenge of manipulating chromatin to influence innate immune signalling. Chromatin relaxation within MN may facilitate cGAS binding but does not guarantee productive cGAMP generation or downstream pathway activation. Overall, these findings added nuance to the concept of chromatin-based modulation of cGAS/STING and suggested that more

investigation is needed to determine whether HDAC inhibition is a robust strategy for enhancing radiation-induced IFN-β production.

4.4 Role of MN in cGAS/STING pathway signalling and type I IFN induction

In this study, increased cGAS-positive MN at 3 or 5 Gy did not consistently translate into higher nuclear IRF-3 with vorinostat, prompting the question of whether MN are reliable drivers of cGAS/STING in this context. One of the most recently debated questions in the field is whether MN act as true drivers of cGAS/STING activation or are just largely non-productive by-products of genome instability. On the one hand, several studies have provided evidence that MN are important substrates for cGAS recognition. Following DNA damage caused by irradiation and subsequent mitotic progression that can lead to MN formation, cGAS localises to ruptured MN and this correlates with the induction of type I IFNs and downstream gene expression, suggesting that MN serve as sites of sustained cytosolic DNA sensing. In these models, the rupture of the MN nuclear envelope provides a temporal window in which exposed double-stranded DNA is accessible to cGAS. (58,59,144,145) MN were also reported to recruit a subset of nuclear and cytoplasmic proteins that were biased to DNA binders, supporting the concept that MN provide a major source of cytosolic DNA for cGAS detection and activation. (146) This has led to the prevailing view that MN act as a crucial intermediate structure linking genomic damage to innate immune activation.

While the above reports support the idea of MN as active drivers of cGAS/STING in defined contexts, the 5 Gy data in this study along with other studies contrast with this view, with accumulating evidence challenging the universality of this model.

Apart from the challenge of highly condensed nucleosomal DNA in MN hindering cGAS activation as targeted in this study, (65) several reports have observed that not all MN engage cGAS, and even when cGAS binding occurred, productive STING/TBK1/IRF3 signalling was not guaranteed, aligning with this study's data. One study showed that cGAS accumulation during mitosis did not activate STING in the subsequent interphase or trigger IFN response, and that irradiation activated STING independently of MN formation. This suggested that cGAS accumulation in MN may not be a robust indicator of its activation, and that MN may not be the primary trigger of the cGAS/STING pathway. (63) Another study demonstrated that cGAS-coated chromatin bridges instead of MN were responsible for activating cGAS. (64) Ruptured MN were also found to be rapidly targeted for lysosomal degradation via autophagy, biasing them towards collapse and clearance, and thereby shortening the window for cGAS/STING signalling and dampening IFN output. (147,148) Thus, although MN formation is a visible and frequent outcome of radiation-induced genomic stress, their actual contribution to downstream IFN production may be context-dependent and less potent than initially assumed.

Importantly, there are other MN-independent routes to IFN induction that complicate interpretation. For example, mitochondrial stress after high-dose irradiation can lead to mitochondrial DNA leakage into the cytosol, which can also activate the cGAS/STING pathway and induce type I IFN production. (149–152) Additionally, epigenetic stimuli such as DNA methyltransferase inhibition can induce a 'viral mimicry' response, where silenced endogenous retroelements are reactivated to generate double-stranded RNA that is then sensed by cytosolic sensors like melanoma differentiation-associated protein 5 and RIG-I, activating mitochondrial antiviral signalling protein and IRF-7 to drive IFN production independently of MN.

(153,154) These alternative inputs indicate that IFN production after irradiation cannot be solely attributed to MN-associated signalling.

Taken together, the current evidence suggests that MN may function as one of the several possible sources of immunostimulatory DNA following irradiation, but their contributions are not universal or exclusive. In some contexts, MN provide a potent and active source for cGAS recruitment and innate immune signalling, while in other situations, they are effectively neutralised or bypassed as inert by-products in favour of other DNA- or RNA-sensing pathways.

4.5 Biological significance, future directions and concluding perspective

Although the interventions tested in this study did not yield strong enhancement in IFN-β after irradiation, the findings are biologically significant in refining the map of where leverage may or may not exist within the cGAS/STING/IFN axis. They demonstrated that indirect strategies such as GSK3β repression or broad HDAC inhibition did not necessarily provide robust entry points to amplify radiation-induced type I IFN production, at least in the tested setting. By ruling out these directions, this study narrows the focus to more promising alternatives that may directly stabilise or potentiate cGAS/STING activity, protect STING trafficking, or modulate the kinetics of negative feedback. In this sense, the results contributed incremental but important knowledge to the broader effort of rendering radiotherapy more pro-immunogenic.

Several future directions can be explored following the observations obtained from this study. Firstly, more direct strategies to manipulate the pathway can be considered, such as pharmacological cGAMP analogues, small-molecule STING

agonists or interventions that stabilise STING in its active trafficking state. Methodological refinements should also be included for more direct measurement of pathway activation, such as utilising ELISA to quantify cGAMP and quantitative PCR or ELISA to confirm IFN-β output in HDAC inhibition conditions. These assays could directly demonstrate whether increased cGAS binding translates into functional activation, which could not be definitively established here. Moreover, investigating more cancer cell types and tumour contexts will be essential, since the signalling architecture in HEK293 cells is not representative of transformed states where GSK3β activity and IFN regulation may be wired differently. Finally, running analyses with multiple timepoints rather than a single time endpoint would allow clearer dissection of transient pulses versus sustained responses.

Importantly, this study also highlights that type I IFN itself represents a double-edged sword. While transient induction after radiotherapy can enhance antigen presentation, T-cell priming and anti-tumour immunity, (32–42) chronic or excessive IFN signalling can drive immunosuppressive feedback, foster T-cell exhaustion and potentially promote tumour adaptation and immune dysfunction. (33,34,155,156) This duality suggests that successful therapeutic exploitation will depend not only on amplifying IFN, but also on tuning its amplitude and duration to avoid detrimental consequences. Therefore, interventions that bias towards a controlled, transient period of increased IFN rather than prolonged activation may hold the greatest translational value.

In conclusion, this study underscores the challenges of manipulating radiation-induced IFN responses through indirect kinase or chromatin modulators. Although the approaches tested here did not achieve strong positive results, they sharpen our understanding of the pathway's constraints and inform the debate on the role of

MN in cGAS/STING activation. This work emphasises that refining radiotherapy's immunogenic potential will likely require direct and more precisely timed interventions in the DNA-sensing machinery. By clarifying these boundaries, this study contributes to a more nuanced foundation for developing rational combination strategies in the future.

5. References

1. Choong ES, Turner RN, Flatley MJ. Radiotherapy: basic principles and technical advances. *Orthop Trauma*. 2014;28(3):167–71. https://doi.org/10.1016/j.mporth.2014.04.003

2. Mee T, Kirkby NF, Defourny NN, Kirkby KJ, Burnet NG. The use of radiotherapy, surgery and chemotherapy in the curative treatment of cancer: results from the FORTY (Favourable Outcomes from RadioTherapY) project. *Br J Radiol*. 2023;96(1152):20230334. https://doi.org/10.1259/bjr.20230334

3. Hami R, Apeke S, Redou P, Gaubert L, Dubois LJ, Lambin P, et al. Predicting the Tumour Response to Radiation by Modelling the Five Rs of Radiotherapy Using PET Images. *J Imaging*. 2023;9(6):124. https://doi.org/10.3390/jimaging9060124

4. Zhu H, Chua MLK, Chitapanarux I, Kaidar-Person O, Mwaba C, Alghamdi M, et al. Global radiotherapy demands and corresponding radiotherapy-professional workforce requirements in 2022 and predicted to 2050: a population-based study. *Lancet Glob Health*. 2024;12(12):e1945–53. https://doi.org/10.1016/S2214-109X(24)00355-3

5. Baskar R, Lee KA, Yeo R, Yeoh KW. Cancer and Radiation Therapy: Current Advances and Future Directions. *Int J Med Sci*. 2012;9(3):193–9. https://doi.org/10.7150/ijms.3635

6. Skliarenko J, Barry A. Clinical and practical applications of radiation therapy: when should radiation therapy be considered for my patient? *Medicine*. 2020;48(2):84–9. https://doi.org/10.1016/j.mpmed.2019.11.004

7. Kumari S, Mukherjee S, Sinha D, Abdisalaam S, Krishnan S, Asaithamby A. Immunomodulatory Effects of Radiotherapy. *Int J Mol Sci*. 2020;21(21):8151. https://doi.org/10.3390/ijms21218151

8. Hu W, Pei Y, Ning R, Li P, Zhang Z, Hong Z, et al. Immunomodulatory effects of carbon ion radiotherapy in patients with localized prostate cancer. *J Cancer Res Clin Oncol*. 2023;149(8):4533–45. https://doi.org/10.1007/s00432-022-04194-9

9. Cytlak UM, Dyer DP, Honeychurch J, Williams KJ, Travis MA, Illidge TM. Immunomodulation by radiotherapy in tumour control and normal tissue toxicity. *Nat Rev Immunol*. 2022;22(2):124–38. https://doi.org/10.1038/s41577-021-00568-1

10. Mahmood U. Radiotherapy driven immunomodulation of the tumor microenvironment and its impact on clinical outcomes: a promising new treatment paradigm. *Immunol Med*. 2022;45(3):136–45. https://doi.org/10.1080/25785826.2021.1997268

11. Tang J, Malachowska B, Wu X, Guha C. Repurposing Radiation Therapy for Immuno-oncology. *Clin Oncol*. 2021;33(11):683–93. https://doi.org/10.1016/j.clon.2021.08.015

12. Zhang Z, Liu X, Chen D, Yu J. Radiotherapy combined with immunotherapy: the dawn of cancer treatment. *Signal Transduct Target Ther*. 2022;7(1):258. https://doi.org/10.1038/s41392-022-01102-y

13. Zhao X, Shao C. Radiotherapy-Mediated Immunomodulation and Anti-Tumor Abscopal Effect Combining Immune Checkpoint Blockade. *Cancers*. 2020;12(10):2762. https://doi.org/10.3390/cancers12102762

14. Guo S, Yao Y, Tang Y, Xin Z, Wu D, Ni C, et al. Radiation-induced tumor immune microenvironments and potential targets for combination therapy. *Signal Transduct Target Ther*. 2023;8(1):205. https://doi.org/10.1038/s41392-023-01462-z

15. Kaur P, Asea A. Radiation-induced effects and the immune system in cancer. *Front Oncol*. 2012;2:191. https://doi.org/10.3389/fonc.2012.00191

16. Zenga J, Awan MJ, Frei A, Foeckler J, Kuehn R, Kasprzak J, et al. Radiation therapy results in preferential tumor antigen-specific lymphodepletion in head and neck cancer. *Nat Commun*. 2025;16(1):5660. https://doi.org/10.1038/s41467-025-60827-w

17. Wang L, Lynch C, Pitroda SP, Piffkó A, Yang K, Huser AK, et al. Radiotherapy and immunology. *J Exp Med*. 2024;221(7):e20232101. https://doi.org/10.1084/jem.20232101

18. Constanzo J, Faget J, Ursino C, Badie C, Pouget JP. Radiation-Induced Immunity and Toxicities: The Versatility of the cGAS-STING Pathway. *Front Immunol*. 2021;12:680503. https://doi.org/10.3389/fimmu.2021.680503

19. Lumniczky K, Impens N, Armengol G, Candéias S, Georgakilas AG, Hornhardt S, et al. Low dose ionizing radiation effects on the immune system. *Environ Int*. 2021;149:106212. https://doi.org/10.1016/j.envint.2020.106212

20. Yang C, Liang Y, Liu N, Sun M. Role of the cGAS-STING pathway in radiotherapy for non-small cell lung cancer. *Radiat Oncol*. 2023;18(1):145. https://doi.org/10.1186/s13014-023-02335-z

21. Vanpouille-Box C, Alard A, Aryankalayil MJ, Sarfraz Y, Diamond JM, Schneider RJ, et al. DNA exonuclease Trex1 regulates radiotherapy-induced tumour immunogenicity. *Nat Commun*. 2017;8(1):15618. https://doi.org/10.1038/ncomms15618

22. Anderson NM, Simon MC. The tumor microenvironment. *Curr Biol*. 2020;30(16):R921–5. https://doi.org/10.1016/j.cub.2020.06.081

23. de Visser KE, Joyce JA. The evolving tumor microenvironment: From cancer initiation to metastatic outgrowth. *Cancer Cell*. 2023;41(3):374–403. https://doi.org/10.1016/j.ccell.2023.02.016

24. Monjazeb AM, Schalper KA, Villarroel-Espindola F, Nguyen A, Shiao SL, Young K. Effects of Radiation on the Tumor Microenvironment. *Semin Radiat Oncol*. 2020;30(2):145–57. https://doi.org/10.1016/j.semradonc.2019.12.004

25. Boopathi E, Den RB, Thangavel C. Innate Immune System in the Context of Radiation Therapy for Cancer. *Cancers*. 2023;15(15):3972. https://doi.org/10.3390/cancers15153972

26. Chen J, Wang S, Ding Y, Xu D, Zheng S. Radiotherapy-induced alterations in tumor microenvironment: metabolism and immunity. *Front Cell Dev Biol*. 2025;13:1568634. https://doi.org/10.3389/fcell.2025.1568634

27. Arnold KM, Flynn NJ, Raben A, Romak L, Yu Y, Dicker AP, et al. The Impact of Radiation on the Tumor Microenvironment: Effect of Dose and Fractionation Schedules. *Cancer Growth Metastasis*. 2018;11. https://doi.org/10.1177/1179064418761639

28. McGee HM, Jiang D, Soto-Pantoja DR, Nevler A, Giaccia AJ, Woodward WA. Targeting the Tumor Microenvironment in Radiation Oncology: Proceedings from

the 2018 ASTRO–AACR Research Workshop. *Clin Cancer Res*. 2019;25(10):2969–74. https://doi.org/10.1158/1078-0432.CCR-18-3781

29. Kießler M, Plesca I, Sommer U, Wehner R, Wilczkowski F, Müller L, et al. Tumor-infiltrating plasmacytoid dendritic cells are associated with survival in human colon cancer. *J Immunother Cancer*. 2021;9(3):e001813. https://doi.org/10.1136/jitc-2020-001813

30. Fu C, Zhou L, Mi QS, Jiang A. Plasmacytoid Dendritic Cells and Cancer Immunotherapy. *Cells*. 2022;11(2):222. https://doi.org/10.3390/cells11020222

31. Goedegebuure RSA, Vonk C, Kooij LP, Derks S, Thijssen VLJL. Combining Radiation Therapy With Interferons: Back to the Future. *Int J Radiat Oncol Biol Phys*. 2020;108(1):56–69. https://doi.org/10.1016/j.ijrobp.2020.02.016

32. Medrano RFV, Hunger A, Mendonça SA, Barbuto JAM, Strauss BE. Immunomodulatory and antitumor effects of type I interferons and their application in cancer therapy. *Oncotarget*. 2017;8(41):71249–84. https://doi.org/10.18632/oncotarget.19531

33. Yu R, Zhu B, Chen D. Type I interferon-mediated tumor immunity and its role in immunotherapy. *Cell Mol Life Sci*. 2022;79(3):191. https://doi.org/10.1007/s00018-022-04219-z

34. Lim J, Kang I, La J, Ku KB, Kang BH, Kim Y, et al. Harnessing type I interferon-mediated immunity to target malignant brain tumors. *Front Immunol*. 2023;14:1203929. https://doi.org/10.3389/fimmu.2023.1203929

35. Holicek P, Guilbaud E, Klapp V, Truxova I, Spisek R, Galluzzi L, et al. Type I interferon and cancer. *Immunol Rev*. 2024;321(1):115–27. https://doi.org/10.1111/imr.13272

36. Fenton SE, Saleiro D, Platanias LC. Type I and II Interferons in the Anti-Tumor Immune Response. *Cancers*. 2021;13(5):1037. https://doi.org/10.3390/cancers13051037

37. Meyer SP, Bauer R, Brüne B, Schmid T. The role of type I interferon signaling in myeloid anti-tumor immunity. *Front Immunol*. 2025;16:1547466. https://doi.org/10.3389/fimmu.2025.1547466

38. Ohkuri T, Kosaka A, Ishibashi K, Kumai T, Hirata Y, Ohara K, et al. Intratumoral administration of cGAMP transiently accumulates potent macrophages for anti-tumor immunity at a mouse tumor site. *Cancer Immunol Immunother*. 2017;66(6):705–16. https://doi.org/10.1007/s00262-017-1975-1

39. Busselaar J, Sijbranda M, Borst J. The importance of type I interferon in orchestrating the cytotoxic T-cell response to cancer. *Immunol Lett*. 2024;270:106938. https://doi.org/10.1016/j.imlet.2024.106938

40. Lim J, La J, Kim HC, Kang I, Kang BH, Ku KB, et al. Type I interferon signaling regulates myeloid and T cell crosstalk in the glioblastoma tumor microenvironment. *iScience*. 2024;27(9):110810. https://doi.org/10.1016/j.isci.2024.110810

41. Lim JYH, Gerber SA, Murphy SP, Lord EM. Type I interferons induced by radiation therapy mediate recruitment and effector function of CD8+ T cells. *Cancer Immunol Immunother*. 2014;63(3):259–71. https://doi.org/10.1007/s00262-013-1506-7

42. Anz D, Rapp M, Eiber S, Koelzer VH, Thaler R, Haubner S, et al. Suppression of Intratumoral CCL22 by Type I Interferon Inhibits Migration of Regulatory T Cells

and Blocks Cancer Progression. *Cancer Res*. 2015;75(21):4483–93. https://doi.org/10.1158/0008-5472.CAN-14-3499

43. Urban-Wojciuk Z, Khan MM, Oyler BL, Fåhraeus R, Marek-Trzonkowska N, Nita-Lazar A, et al. The Role of TLRs in Anti-cancer Immunity and Tumor Rejection. *Front Immunol*. 2019;10:2388. https://doi.org/10.3389/fimmu.2019.02388

44. Chen X, Zhang Y, Fu Y. The critical role of Toll-like receptor-mediated signaling in cancer immunotherapy. *Med Drug Discov.* 2022;14:100122. https://doi.org/10.1016/j.medidd.2022.100122

45. Jiang Y, Zhang H, Wang J, Chen J, Guo Z, Liu Y, et al. Exploiting RIG-I-like receptor pathway for cancer immunotherapy. *J Hematol Oncol*. 2023;16(1):8. https://doi.org/10.1186/s13045-023-01405-9

46. Elion DL, Cook RS. Harnessing RIG-I and intrinsic immunity in the tumor microenvironment for therapeutic cancer treatment. *Oncotarget*. 2018;9(48):29007–17. https://doi.org/10.18632/oncotarget.25626

47. Deng L, Liang H, Xu M, Yang X, Burnette B, Arina A, et al. STING-Dependent Cytosolic DNA Sensing Promotes Radiation-Induced Type I Interferon-Dependent Antitumor Immunity in Immunogenic Tumors. *Immunity*. 2014;41(5):843–52. https://doi.org/10.1016/j.immuni.2014.10.019

48. Kho VM, Mekers VE, Span PN, Bussink J, Adema GJ. Radiotherapy and cGAS/STING signaling: Impact on MDSCs in the tumor microenvironment. *Cell Immunol*. 2021;362:104298. https://doi.org/10.1016/j.cellimm.2021.104298

49. Woo SR, Fuertes MB, Corrales L, Spranger S, Furdyna MJ, Leung MYK, et al. STING-Dependent Cytosolic DNA Sensing Mediates Innate Immune Recognition of Immunogenic Tumors. *Immunity*. 2014;41(5):830–42. https://doi.org/10.1016/j.immuni.2014.10.017

50. Storozynsky Q, Hitt MM. The Impact of Radiation-Induced DNA Damage on cGAS-STING-Mediated Immune Responses to Cancer. *Int J Mol Sci*. 2020;21(22):8877. https://doi.org/10.3390/ijms21228877

51. Li J, Bakhoum SF. The pleiotropic roles of cGAS–STING signaling in the tumor microenvironment. *J Mol Cell Biol*. 2022;14(4):mjac019. https://doi.org/10.1093/jmcb/mjac019

52. Szmyd R, Casolin S, French L, Manjón AG, Walter M, Cavalli L, et al. Homologous recombination promotes non-immunogenic mitotic cell death upon DNA damage. *Nat Cell Biol*. 2025;27(1):59–72. https://doi.org/10.1038/s41556-024-01557-x

53. Zhao L, Tang A, Long F, Mi D, Sun Y. Modeling of ionizing radiation-induced chromosome aberration and tumor prevalence based on two classes of DNA double-strand breaks clustering in chromatin domains. *Ecotoxicol Environ Saf*. 2023;259:115038. https://doi.org/10.1016/j.ecoenv.2023.115038

54. Burnette BC, Liang H, Lee Y, Chlewicki L, Khodarev NN, Weichselbaum RR, et al. The Efficacy of Radiotherapy Relies upon Induction of Type I Interferon–Dependent Innate and Adaptive Immunity. *Cancer Res*. 2011;71(7):2488–96. https://doi.org/10.1158/0008-5472.CAN-10-2820

55. Zhang Y, Hong W, Zheng D, Li Z, Hu Y, Chen Y, et al. Increased IFN-β indicates better survival in hepatocellular carcinoma treated with radiotherapy. *Clin Exp Immunol*. 2024;218(2):188–98. https://doi.org/10.1093/cei/uxae075

56. Du S, Chen Y, Chiang CL, Shi G, Zhang W, Yang P, et al. Increased Serum Type I Interferon Level May Predict Outcome in Hepatocellular Carcinoma Patients Treated with Radiotherapy. *Int J Radiat Oncol Biol Phys*. 2020;108(3):S85. https://doi.org/10.1016/j.ijrobp.2020.07.2243

57. Hatch EM, Fischer AH, Deerinck TJ, Hetzer MW. Catastrophic Nuclear Envelope Collapse in Cancer Cell Micronuclei. *Cell*. 2013;154(1):47–60. https://doi.org/10.1016/j.cell.2013.06.007

58. Mackenzie KJ, Carroll P, Martin CA, Murina O, Fluteau A, Simpson DJ, et al. cGAS surveillance of micronuclei links genome instability to innate immunity. *Nature*. 2017;548(7668):461–5. https://doi.org/10.1038/nature23449

59. Harding SM, Benci JL, Irianto J, Discher DE, Minn AJ, Greenberg RA. Mitotic progression following DNA damage enables pattern recognition within micronuclei. *Nature*. 2017;548(7668):466–70. https://doi.org/10.1038/nature23470

60. MacDonald KM, Benguerfi S, Harding SM. Alerting the immune system to DNA damage: micronuclei as mediators. *Essays Biochem*. 2020;64(5):753–64. https://doi.org/10.1042/EBC20200016

61. Basit A, Cho MG, Kim EY, Kwon D, Kang SJ, Lee JH. The cGAS/STING/TBK1/IRF3 innate immunity pathway maintains chromosomal stability through regulation of p21 levels. *Exp Mol Med*. 2020;52(4):643–57. https://doi.org/10.1038/s12276-020-0416-y

62. Chauvin SD, Stinson WA, Platt DJ, Poddar S, Miner JJ. Regulation of cGAS and STING signaling during inflammation and infection. *J Biol Chem*. 2023;299(7):104866. https://doi.org/10.1016/j.jbc.2023.104866

63. Sato Y, Hayashi MT. Micronucleus is not a potent inducer of the cGAS/STING pathway. *Life Sci Alliance*. 2024;7(4):e202302424. https://doi.org/10.26508/lsa.202302424

64. Flynn PJ, Koch PD, Mitchison TJ. Chromatin bridges, not micronuclei, activate cGAS after drug-induced mitotic errors in human cells. *Proc Natl Acad Sci*. 2021;118(48):e2103585118. https://doi.org/10.1073/pnas.2103585118

65. Takaki T, Millar R, Hiley CT, Boulton SJ. Micronuclei induced by radiation, replication stress, or chromosome segregation errors do not activate cGAS-STING. *Mol Cell*. 2024;84(11):2203-2213.e5. https://doi.org/10.1016/j.molcel.2024.04.017

66. Luo J. Glycogen synthase kinase 3β (GSK3β) in tumorigenesis and cancer chemotherapy. *Cancer Lett*. 2009;273(2):194–200. https://doi.org/10.1016/j.canlet.2008.05.045

67. Medunjanin S, Schleithoff L, Fiegehenn C, Weinert S, Zuschratter W, Braun-Dullaeus RC. GSK-3β controls NF-kappaB activity via IKKγ/NEMO. *Sci Rep*. 2016;6(1):38553. https://doi.org/10.1038/srep38553

68. Walz A, Ugolkov A, Chandra S, Kozikowski A, Carneiro BA, O'Halloran TV, et al. Molecular Pathways: Revisiting Glycogen Synthase Kinase-3β as a Target for the Treatment of Cancer. *Clin Cancer Res*. 2017;23(8):1891–7. https://doi.org/10.1158/1078-0432.CCR-15-2240

69. Abd-Ellah A, Voogdt C, Krappmann D, Möller P, Marienfeld RB. GSK3β modulates NF-κB activation and RelB degradation through site-specific phosphorylation of BCL10. *Sci Rep*. 2018;8(1):1352. https://doi.org/10.1038/s41598-018-19822-z

70. Pai SG, Carneiro BA, Mota JM, Costa R, Leite CA, Barroso-Sousa R, et al. Wnt/beta-catenin pathway: modulating anticancer immune response. *J Hematol Oncol*. 2017;10(1):101. https://doi.org/10.1186/s13045-017-0471-6

71. Tang QL, Xie XB, Wang J, Chen Q, Han AJ, Zou CY, et al. Glycogen Synthase Kinase-3β, NF-κB Signaling, and Tumorigenesis of Human Osteosarcoma. *J Natl Cancer Inst*. 2012;104(10):749–63. https://doi.org/10.1093/jnci/djs210

72. He R, Du S, Lei T, Xie X, Wang Y. Glycogen synthase kinase 3β in tumorigenesis and oncotherapy. *Oncol Rep*. 2020;44(6):2373–85. https://doi.org/10.3892/or.2020.7817

73. Mamaghani S, Patel S, Hedley DW. Glycogen synthase kinase-3 inhibition disrupts nuclear factor-kappaB activity in pancreatic cancer, but fails to sensitize to gemcitabine chemotherapy. *BMC Cancer*. 2009;9(1):132. https://doi.org/10.1186/1471-2407-9-132

74. Zheng Y, Yang Y, Zhu W, Liu R, Liu A, Zhang R, et al. GSK3B inhibition reduced cervical cancer cell proliferation and migration by modulating the PI3K/Akt signaling pathway and epithelial-to-mesenchymal transition. *Braz J Med Biol Res*. 2024;57:e13796. https://doi.org/10.1590/1414-431X2024e13796

75. Duda P, Akula SM, Abrams SL, Steelman LS, Martelli AM, Cocco L, et al. Targeting GSK3 and Associated Signaling Pathways Involved in Cancer. *Cells*. 2020;9(5):1110. https://doi.org/10.3390/cells9051110

76. Salim T, Sjölander A, Sand-Dejmek J. Nuclear expression of Glycogen synthase kinase-3β and lack of membranous β-catenin is correlated with poor survival in colon cancer. *Int J Cancer*. 2013;133(4):807–15. https://doi.org/10.1002/ijc.28074

77. Shakoori A, Ougolkov A, Yu ZW, Zhang B, Modarressi MH, Billadeau DD, et al. Deregulated GSK3β activity in colorectal cancer: Its association with tumor cell survival and proliferation. *Biochem Biophys Res Commun*. 2005;334(4):1365–73. https://doi.org/10.1016/j.bbrc.2005.07.041

78. Cho YJ, Kim JH, Yoon J, Cho SJ, Ko YS, Park JW, et al. Constitutive activation of glycogen synthase kinase-3β correlates with better prognosis and cyclin-dependent kinase inhibitors in human gastric cancer. *BMC Gastroenterol*. 2010;10(1):91. https://doi.org/10.1186/1471-230X-10-91

79. Bauer L, Langer R, Becker K, Hapfelmeier A, Ott K, Novotny A, et al. Expression Profiling of Stem Cell-Related Genes in Neoadjuvant-Treated Gastric Cancer: A NOTCH2, GSK3B and β-catenin Gene Signature Predicts Survival. *PLoS One*. 2012;7(9):e44566. https://doi.org/10.1371/journal.pone.0044566

80. Wang Y, Lam JB, Lam KSL, Liu J, Lam MC, Hoo RLC, et al. Adiponectin Modulates the Glycogen Synthase Kinase-3β/β-Catenin Signaling Pathway and Attenuates Mammary Tumorigenesis of MDA-MB-231 Cells in Nude Mice. *Cancer Res*. 2006;66(23):11462–70. https://doi.org/10.1158/0008-5472.CAN-06-1969

81. Duda P, Akula SM, Abrams SL, Steelman LS, Gizak A, Rakus D, et al. GSK-3 and miRs: Master regulators of therapeutic sensitivity of cancer cells. *Biochim Biophys Acta Mol Cell Res*. 2020;1867(10):118770. https://doi.org/10.1016/j.bbamcr.2020.118770

82. Lin J, Song T, Li C, Mao W. GSK-3β in DNA repair, apoptosis, and resistance of chemotherapy, radiotherapy of cancer. *Biochim Biophys Acta Mol Cell Res*. 2020;1867(5):118659. https://doi.org/10.1016/j.bbamcr.2020.118659

83. Tao S, Pu Y, Yang EJ, Ren G, Shi C, Chen LJ, et al. Inhibition of GSK3β is synthetic lethal with FHIT loss in lung cancer by blocking homologous recombination repair. *Exp Mol Med*. 2025;57(1):167–83. https://doi.org/10.1038/s12276-024-01374-0

84. Atkinson JM, Rank KB, Zeng Y, Capen A, Yadav V, Manro JR, et al. Activating the Wnt/β-Catenin Pathway for the Treatment of Melanoma – Application of LY2090314, a Novel Selective Inhibitor of Glycogen Synthase Kinase-3. *PLoS One*. 2015;10(4):e0125028. https://doi.org/10.1371/journal.pone.0125028

85. Harrison KS, Jones C. Wnt antagonists suppress herpes simplex virus type 1 productive infection. *Antiviral Res*. 2021;191:105082. https://doi.org/10.1016/j.antiviral.2021.105082

86. Rizzieri DA, Cooley S, Odenike O, Moonan L, Chow KH, Jackson K, et al. An open-label phase 2 study of glycogen synthase kinase-3 inhibitor LY2090314 in patients with acute leukemia. *Leuk Lymphoma*. 2016;57(8):1800–6. https://doi.org/10.3109/10428194.2015.1122781

87. Carneiro BA, Cavalcante L, Mahalingam D, Saeed A, Safran H, Ma WW, et al. Phase I Study of Elraglusib (9-ING-41), a Glycogen Synthase Kinase-3β Inhibitor, as Monotherapy or Combined with Chemotherapy in Patients with Advanced Malignancies. *Clin Cancer Res*. 2024;30(3):522–31. https://doi.org/10.1158/1078-0432.CCR-23-1916

88. Kuroki H, Anraku T, Kazama A, Bilim V, Tasaki M, Schmitt D, et al. 9-ING-41, a small molecule inhibitor of GSK-3beta, potentiates the effects of anticancer therapeutics in bladder cancer. *Sci Rep*. 2019;9(1):19977. https://doi.org/10.1038/s41598-019-56461-4

89. Pal K, Cao Y, Gaisina IN, Bhattacharya S, Dutta SK, Wang E, et al. Inhibition of GSK-3 Induces Differentiation and Impaired Glucose Metabolism in Renal Cancer. *Mol Cancer Ther*. 2014;13(2):285–96. https://doi.org/10.1158/1535-7163.MCT-13-0681

90. Gray JE, Infante JR, Brail LH, Simon GR, Cooksey JF, Jones SF, et al. A first-in-human phase I dose-escalation, pharmacokinetic, and pharmacodynamic evaluation of intravenous LY2090314, a glycogen synthase kinase 3 inhibitor, administered in combination with pemetrexed and carboplatin. *Invest New Drugs*. 2015;33(6):1187–96. https://doi.org/10.1007/s10637-015-0278-7

91. Mahalingam D, Carneiro BA, Safran H, Powell SF, Coveler AL, Davis EJ, et al. Phase 2 study of 9-ING-41, a small molecule selective glycogen synthase kinase-3 beta (GSK-3β) inhibitor, with gemcitabine/nab-paclitaxel (GnP) in first-line advanced pancreatic ductal adenocarcinoma (PDAC). *J Clin Oncol*. 2022;40(4_suppl):578–578. https://doi.org/10.1200/jco.2022.40.4_suppl.578

92. Ugolkov A, Qiang W, Bondarenko G, Procissi D, Gaisina I, James CD, et al. Combination Treatment with the GSK-3 Inhibitor 9-ING-41 and CCNU Cures Orthotopic Chemoresistant Glioblastoma in Patient-Derived Xenograft Models. *Transl Oncol*. 2017;10(4):669–78. https://doi.org/10.1016/j.tranon.2017.06.003

93. Yang H, Salz T, Zajac-Kaye M, Liao D, Huang S, Qiu Y. Overexpression of histone deacetylases in cancer cells is controlled by interplay of transcription factors and epigenetic modulators. *FASEB J*. 2014;28(10):4265–79. https://doi.org/10.1096/fj.14-250654

94. Bondarev AD, Attwood MM, Jonsson J, Chubarev VN, Tarasov VV, Schiöth HB. Recent developments of HDAC inhibitors: Emerging indications and novel

molecules. *Br J Clin Pharmacol*. 2021;87(12):4577–97. https://doi.org/10.1111/bcp.14889

95. Agustinus AS, Al-Rawi D, Dameracharla B, Raviram R, Jones BSCL, Stransky S, et al. Epigenetic dysregulation from chromosomal transit in micronuclei. *Nature*. 2023;619(7968):176–83. https://doi.org/10.1038/s41586-023-06084-7

96. Ree AH, Dueland S, Folkvord S, Hole KH, Seierstad T, Johansen M, et al. Vorinostat, a histone deacetylase inhibitor, combined with pelvic palliative radiotherapy for gastrointestinal carcinoma: the Pelvic Radiation and Vorinostat (PRAVO) phase 1 study. *Lancet Oncol*. 2010;11(5):459–64. https://doi.org/10.1016/S1470-2045(10)70058-9

97. Galanis E, Anderson SK, Miller CR, Sarkaria JN, Jaeckle K, Buckner JC, et al. Phase I/II trial of vorinostat combined with temozolomide and radiation therapy for newly diagnosed glioblastoma: results of Alliance N0874/ABTC 02. *Neuro Oncol*. 2018;20(4):546–56. https://doi.org/10.1093/neuonc/nox161

98. Shi W, Lawrence YR, Choy H, Wachsberger PR, Andrews DW, Werner-Wasik M, et al. Vorinostat as a radiosensitizer for CNS malignancies: Preclinical results and phase I trial in brain metastasis. *J Clin Oncol*. 2013;31(15_suppl):2100. https://doi.org/10.1200/jco.2013.31.15_suppl.2100

99. Su JM, Kilburn LB, Mansur DB, Krailo M, Buxton A, Adekunle A, et al. Phase I/II trial of vorinostat and radiation and maintenance vorinostat in children with diffuse intrinsic pontine glioma: A Children's Oncology Group report. *Neuro Oncol*. 2022;24(4):655–64. https://doi.org/10.1093/neuonc/noab188

100. Hamon P, Gerbé De Thoré M, Classe M, Signolle N, Liu W, Bawa O, et al. TGFβ receptor inhibition unleashes interferon-β production by tumor-associated macrophages and enhances radiotherapy efficacy. *J Immunother Cancer*. 2022;10(3):e003519. https://doi.org/10.1136/jitc-2021-003519

101. Zhang Q, Jiang L, Wang W, Huber AK, Valvo VM, Jungles KM, et al. Potentiating the radiation-induced type I interferon anti-tumoral immune response by ATM inhibition in pancreatic cancer. *JCI Insight*. 2024;9(6):e168824. https://doi.org/10.1172/jci.insight.168824

102. Valvo VM, Zhang Q, Jiang L, Holcomb EA, Pearson AN, Edmunds AG, et al. Olaparib and Radiotherapy Induce Type I Interferon– and CD8+ T Cell–Dependent Sensitization to Immunotherapy in Pancreatic Cancer. *Mol Cancer Ther*. 2025;24(6):843–58. https://doi.org/10.1158/1535-7163.MCT-24-0210

103. Nadin SB, Cuello-Carrión FD, Cayado-Gutiérrez N, Fanelli MA. Overview of Wnt/β-Catenin Pathway and DNA Damage/Repair in Cancer. *Biology*. 2025;14(2):185. https://doi.org/10.3390/biology14020185

104. Zhang N, Tian YN, Zhou LN, Li MZ, Chen HD, Song SS, et al. Glycogen synthase kinase 3β inhibition synergizes with PARP inhibitors through the induction of homologous recombination deficiency in colorectal cancer. *Cell Death Dis*. 2021;12(2):183. https://doi.org/10.1038/s41419-021-03475-4

105. Ding L, Madamsetty VS, Kiers S, Alekhina O, Ugolkov A, Dube J, et al. Glycogen Synthase Kinase-3 Inhibition Sensitizes Pancreatic Cancer Cells to Chemotherapy by Abrogating the TopBP1/ATR-Mediated DNA Damage Response. *Clin Cancer Res*. 2019;25(21):6452–62. https://doi.org/10.1158/1078-0432.CCR-19-0799

106. Yang Y, Lei T, Du S, Tong R, Wang H, Yang J, et al. Nuclear GSK3β induces DNA double-strand break repair by phosphorylating 53BP1 in glioblastoma. *Int J Oncol*. 2018;52(3):709–20. https://doi.org/10.3892/ijo.2018.4237

107. Ugolkov AV, Bondarenko GI, Dubrovskyi O, Berbegall AP, Navarro S, Noguera R, et al. 9-ING-41, a small-molecule glycogen synthase kinase-3 inhibitor, is active in neuroblastoma. *Anticancer Drugs*. 2018;29(8):717–24. http://doi.org/10.1097/CAD.0000000000000652

108. Coats JT, Tauro S, Sutherland C. Elraglusib (formerly 9-ING-41) possesses potent anti-lymphoma properties which cannot be attributed to GSK3 inhibition. *Cell Commun Signal*. 2023;21(1):131. https://doi.org/10.1186/s12964-023-01147-8

109. Martelli AM, Evangelisti C, Paganelli F, Chiarini F, McCubrey JA. GSK-3: a multifaceted player in acute leukemias. *Leukemia*. 2021;35(7):1829–42. https://doi.org/10.1038/s41375-021-01243-z

110. Yie J, Senger K, Thanos D. Mechanism by which the IFN-β enhanceosome activates transcription. *Proc Natl Acad Sci*. 1999;96(23):13108–13. https://doi.org/10.1073/pnas.96.23.13108

111. Panne D, Maniatis T, Harrison SC. An Atomic Model of the Interferon-β Enhanceosome. *Cell*. 2007;129(6):1111–23. https://doi.org/10.1016/j.cell.2007.05.019

112. Hare DN, Baid K, Dvorkin-Gheva A, Mossman KL. Virus-Intrinsic Differences and Heterogeneous IRF3 Activation Influence IFN-Independent Antiviral Protection. *iScience*. 2020;23(12):101864. https://doi.org/10.1016/j.isci.2020.101864

113. Porritt RA, Hertzog PJ. Dynamic control of type I IFN signalling by an integrated network of negative regulators. *Trends Immunol*. 2015;36(3):150–60. https://doi.org/10.1016/j.it.2015.02.002

114. Leya M, Yang D, Bao THTN, Jeong H, Oh SI, Kim JH, et al. The role of 2'–5'-oligoadenylate synthase-like protein (OASL1) in biliary and hepatotoxin-induced liver injury in mice. *Sci Rep*. 2024;14(1):21873. https://doi.org/10.1038/s41598-024-72465-1

115. Lee MS, Kim B, Oh GT, Kim YJ. OASL1 inhibits translation of the type I interferon–regulating transcription factor IRF7. *Nat Immunol*. 2013;14(4):346–55. https://doi.org/10.1038/ni.2535

116. Sim CK, Cho YS, Kim BS, Baek IJ, Kim YJ, Lee MS. 2′–5′ Oligoadenylate synthetase-like 1 (OASL1) deficiency in mice promotes an effective anti-tumor immune response by enhancing the production of type I interferons. *Cancer Immunol Immunother*. 2016;65(6):663–75. https://doi.org/10.1007/s00262-016-1830-9

117. Sim CK, Lee JH, Baek IJ, Lee SW, Lee MS. Enhanced Antitumor Immune Response in 2′-5′ Oligoadenylate Synthetase-Like 1- (OASL1-) Deficient Mice upon Cisplatin Chemotherapy and Radiotherapy. *J Immunol Res*. 2019;2019(1):1–14. https://doi.org/10.1155/2019/7596786

118. Chen X, Cao M, Wang P, Chu S, Li M, Hou P, et al. The emerging roles of TRIM21 in coordinating cancer metabolism, immunity and cancer treatment. *Front Immunol*. 2022;13:968755. https://doi.org/10.3389/fimmu.2022.968755

119. Yoshimi R, Chang TH, Wang H, Atsumi T, Morse HC, Ozato K. Gene Disruption Study Reveals a Nonredundant Role for TRIM21/Ro52 in NF-κB-Dependent

Cytokine Expression in Fibroblasts. *J Immunol*. 2009;182(12):7527–38. https://doi.org/10.4049/jimmunol.0804121

120. Li A, Wang J, Qu Y. TRIM21: a multifaceted regulator in cancer. *Front Cell Dev Biol*. 2025;13:1637451. https://doi.org/10.3389/fcell.2025.1637451

121. Wegner J, Hunkler C, Ciupka K, Hartmann G, Schlee M. Increased IKKε protein stability ensures efficient type I interferon responses in conditions of TBK1 deficiency. *Front Immunol*. 2023;14:1073608. https://doi.org/10.3389/fimmu.2023.1073608

122. Córdoba-David G, García-Giménez J, Cardoso Castelo-Branco R, Carrasco S, Cannata P, Ortiz A, et al. Crosstalk between TBK1/IKKε and the type I interferon pathway contributes to tubulointerstitial inflammation and kidney tubular injury. *Front Pharmacol*. 2022;13:987979. https://doi.org/10.3389/fphar.2022.987979

123. Balka KR, Louis C, Saunders TL, Smith AM, Calleja DJ, D'Silva DB, et al. TBK1 and IKKε Act Redundantly to Mediate STING-Induced NF-κB Responses in Myeloid Cells. *Cell Rep*. 2020;31(1):107492. https://doi.org/10.1016/j.celrep.2020.03.056

124. Chung EJ, Lee S, Sausville EA, Ryan Q, Karp JE, Gojo I, et al. Histone deacetylase inhibitor pharmacodynamic analysis by multiparameter flow cytometry. *Ann Clin Lab Sci*. 2005;35(4):397–406. https://www.annclinlabsci.org/content/35/4/397.full [Accessed 29th September 2025].

125. Ma'arif B, Abada I, Mahardiani A, Hakim A, Maulina N, Purwitasari N, et al. A Systematic Review: Comparison of Immunocytochemistry, ELISA, and Western Blot Methods in Alkaline phosphatase Measurement at Genistein-induced Osteoblast Cell. *Biomed Pharmacol J*. 2022;15(4):1853–65. https://doi.org/10.13005/bpj/2523

126. Petruccelli LA, Dupéré-Richer D, Pettersson F, Retrouvey H, Skoulikas S, Miller WH. Vorinostat Induces Reactive Oxygen Species and DNA Damage in Acute Myeloid Leukemia Cells. *PLoS One*. 2011;6(6):e20987. https://doi.org/10.1371/journal.pone.0020987

127. Conti C, Leo E, Eichler GS, Sordet O, Martin MM, Fan A, et al. Inhibition of Histone Deacetylase in Cancer Cells Slows Down Replication Forks, Activates Dormant Origins, and Induces DNA Damage. *Cancer Res*. 2010;70(11):4470–80. https://doi.org/10.1158/0008-5472.CAN-09-3028

128. Bergadà L, Yeramian A, Sorolla A, Matias-Guiu X, Dolcet X. Antioxidants Impair Anti-Tumoral Effects of Vorinostat, but Not Anti-Neoplastic Effects of Vorinostat and Caspase-8 Downregulation. *PLoS One*. 2014;9(3):e92764. https://doi.org/10.1371/journal.pone.0092764

129. El Omari N, Khalid A, Makeen HA, Alhazmi HA, Albratty M, Mohan S, et al. Stochasticity of anticancer mechanisms underlying clinical effectiveness of vorinostat. *Heliyon*. 2024;10(12):e33052. https://doi.org/10.1016/j.heliyon.2024.e33052

130. Kim E, Bisson WH, Löhr CV, Williams DE, Ho E, Dashwood RH, et al. Histone and Non-Histone Targets of Dietary Deacetylase Inhibitors. *Curr Top Med Chem*. 2015;16(7):714–31. https://doi.org/10.2174/1568026615666150825125857

131. Dai J, Huang YJ, He X, Zhao M, Wang X, Liu ZS, et al. Acetylation Blocks cGAS Activity and Inhibits Self-DNA-Induced Autoimmunity. *Cell*. 2019;176(6):1447-1460.e14. https://doi.org/10.1016/j.cell.2019.01.016

132. Yu L, Liu P. Cytosolic DNA sensing by cGAS: regulation, function, and human diseases. *Signal Transduct Target Ther*. 2021;6(1):170. https://doi.org/10.1038/s41392-021-00554-y

133. Song ZM, Lin H, Yi XM, Guo W, Hu MM, Shu HB. KAT5 acetylates cGAS to promote innate immune response to DNA virus. *Proc Natl Acad Sci*. 2020;117(35):21568–75. https://doi.org/10.1073/pnas.1922330117

134. Joshi B, Joshi JC, Mehta D. Regulation of cGAS Activity and Downstream Signaling. *Cells*. 2022;11(18):2812. https://doi.org/10.3390/cells11182812

135. Alarcón-Espósito J, Nagiri RK, Gan L, Sinha SC. Identification and development of cGAS inhibitors and their uses to treat Alzheimer's disease. *Neurotherapeutics*. 2025;22(3):e00536. https://doi.org/10.1016/j.neurot.2025.e00536

136. Tang Y, Li X, Wei Y, Sun Y, Yang Y, Zhang X, et al. A preliminary study of KAT2A on cGAS-related immunity in inflammation amplification of systemic lupus erythematosus. *Cell Death Dis*. 2021;12(11):1036. https://doi.org/10.1038/s41419-021-04323-1

137. Tang J-L, Yang Q, Xu C-H, Zhao H, Liu Y-L, Liu C-Y, et al. Histone deacetylase 3 promotes innate antiviral immunity through deacetylation of TBK1. *Protein Cell*. 2021;12(4):261–78. https://doi.org/10.1007/s13238-020-00751-5

138. Ghosh G, Sen M. A New DNA Methyltransferase-Histone Deacetylase-Kinase Axis in Innate Immunity. *Mol Cell*. 2016;63(4):544–6. https://doi.org/10.1016/j.molcel.2016.08.007

139. Yang C, Croteau S, Hardy P. Histone deacetylase (HDAC) 9: versatile biological functions and emerging roles in human cancer. *Cellular Oncology*. 2021;44(5):997–1017. https://doi.org/10.1007/s13402-021-00626-9

140. MacDonald KM, Nicholson-Puthenveedu S, Tageldein MM, Khasnis S, Arrowsmith CH, Harding SM. Antecedent chromatin organization determines cGAS recruitment to ruptured micronuclei. *Nat Commun*. 2023;14(1):556. https://doi.org/10.1038/s41467-023-36195-8

141. Mukai K, Konno H, Akiba T, Uemura T, Waguri S, Kobayashi T, et al. Activation of STING requires palmitoylation at the Golgi. *Nat Commun*. 2016;7(1):11932. https://doi.org/10.1038/ncomms11932

142. Farber-Katz SE, Dippold HC, Buschman MD, Peterman MC, Xing M, Noakes CJ, et al. DNA Damage Triggers Golgi Dispersal via DNA-PK and GOLPH3. *Cell*. 2014;156(3):413–27. https://doi.org/10.1016/j.cell.2013.12.023

143. Foiani M, Bartek J. Golgi Feels DNA's Pain. *Cell*. 2014;156(3):392–3. https://doi.org/10.1016/j.cell.2014.01.030

144. Gekara NO. DNA damage-induced immune response: Micronuclei provide key platform. *J Cell Biol*. 2017;216(10):2999–3001. https://doi.org/10.1083/jcb.201708069

145. Dou Z, Ghosh K, Vizioli MG, Zhu J, Sen P, Wangensteen KJ, et al. Cytoplasmic chromatin triggers inflammation in senescence and cancer. *Nature*. 2017;550(7676):402–6. https://doi.org/10.1038/nature24050

146. MacDonald KM, Khan S, Lin B, Hurren R, Schimmer AD, Kislinger T, et al. The proteomic landscape of genotoxic stress-induced micronuclei. *Mol Cell*. 2024;84(7):1377-1391.e6. https://doi.org/10.1016/j.molcel.2024.02.001

147. Bartsch K, Knittler K, Borowski C, Rudnik S, Damme M, Aden K, et al. Absence of RNase H2 triggers generation of immunogenic micronuclei removed by autophagy. *Hum Mol Genet*. 2017;26(20):3960–72. https://doi.org/10.1093/hmg/ddx283

148. Martin S, Scorzoni S, Cordone S, Mazzagatti A, Beznoussenko GV, Gunn AL, et al. A p62-dependent rheostat dictates micronuclei catastrophe and chromosome rearrangements. *Science*. 2024;385(6712):eadj7446. https://doi.org/10.1126/science.adj7446

149. Hu MM, Shu HB. Mitochondrial DNA-triggered innate immune response: mechanisms and diseases. *Cell Mol Immunol*. 2023;20(12):1403–12. https://doi.org/10.1038/s41423-023-01086-x

150. West AP, Khoury-Hanold W, Staron M, Tal MC, Pineda CM, Lang SM, et al. Mitochondrial DNA stress primes the antiviral innate immune response. *Nature*. 2015;520(7548):553–7. https://doi.org/10.1038/nature14156

151. Tigano M, Vargas DC, Tremblay-Belzile S, Fu Y, Sfeir A. Nuclear sensing of breaks in mitochondrial DNA enhances immune surveillance. *Nature*. 2021;591(7850):477–81. https://doi.org/10.1038/s41586-021-03269-w

152. Kim J, Kim HS, Chung JH. Molecular mechanisms of mitochondrial DNA release and activation of the cGAS-STING pathway. *Exp Mol Med*. 2023;55(3):510–9. https://doi.org/10.1038/s12276-023-00965-7

153. Roulois D, Loo Yau H, Singhania R, Wang Y, Danesh A, Shen SY, et al. DNA-Demethylating Agents Target Colorectal Cancer Cells by Inducing Viral Mimicry by Endogenous Transcripts. *Cell*. 2015;162(5):961–73. https://doi.org/10.1016/j.cell.2015.07.056

154. Chiappinelli KB, Strissel PL, Desrichard A, Li H, Henke C, Akman B, et al. Inhibiting DNA Methylation Causes an Interferon Response in Cancer via dsRNA Including Endogenous Retroviruses. *Cell*. 2015;162(5):974–86. https://doi.org/10.1016/j.cell.2015.07.011

155. Snell LM, McGaha TL, Brooks DG. Type I Interferon in Chronic Virus Infection and Cancer. *Trends Immunol*. 2017;38(8):542–57. https://doi.org/10.1016/j.it.2017.05.005

156. Musella M, Galassi C, Manduca N, Sistigu A. The Yin and Yang of Type I IFNs in Cancer Promotion and Immune Activation. *Biology*. 2021;10(9):856. https://doi.org/10.3390/biology10090856

6. Appendices

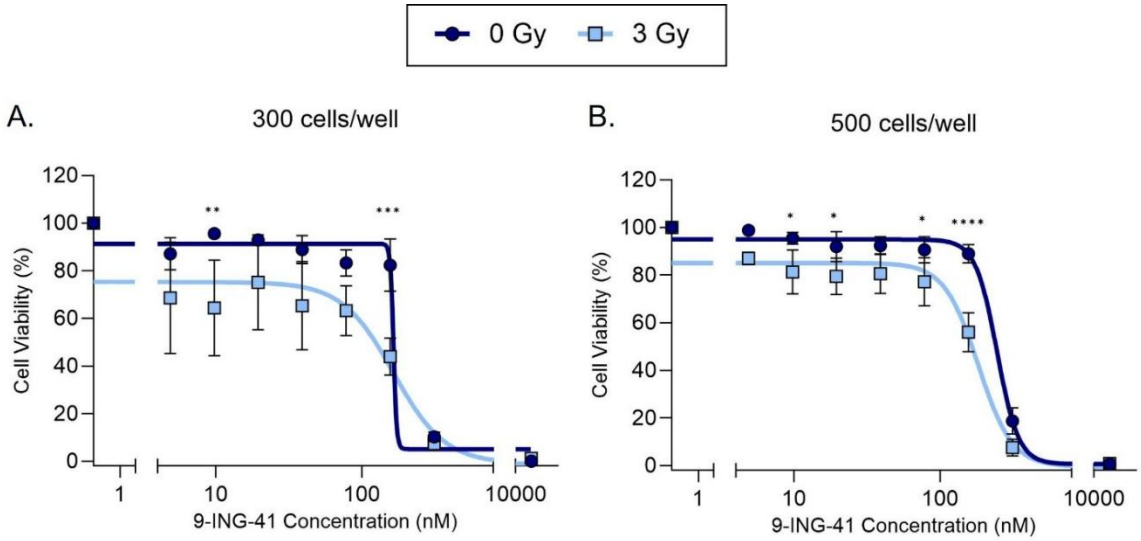

Supplementary Figure 1. HEK293 cell viability following treatment with 9-ING-41 of increasing concentrations and irradiation. HEK293 cells were seeded at **(A)** 300 cells/well or **(B)** 500 cells/well and treated with different concentrations of 9-ING-41 (0, 4.875, 9.75, 19.5, 39, 78, 156, 312 nM and 20 μM)**,** followed by irradiation with 3 Gy. Values obtained from fluorescence detection upon addition of resazurin to wells 7 days post-radiation were normalised to the vehicle control at 0 Gy (for unirradiated samples) or at 3 Gy (for irradiated samples) (set as 100% cell viability) and the negative control (set as 0% cell viability) to detect any radiosensitisation effects. Data presented as mean ± standard deviation with x-axis plotted on a $\log_{10}$ scale. Three biological replicates (N = 3) with three technical replicates (n = 3). Statistical significance assessed on biological replicates by two-way ANOVA with Bonferroni's multiple comparisons for comparison between 0 Gy and 3 Gy for each concentration, *** $p < 0.001$, **** $p < 0.0001$.

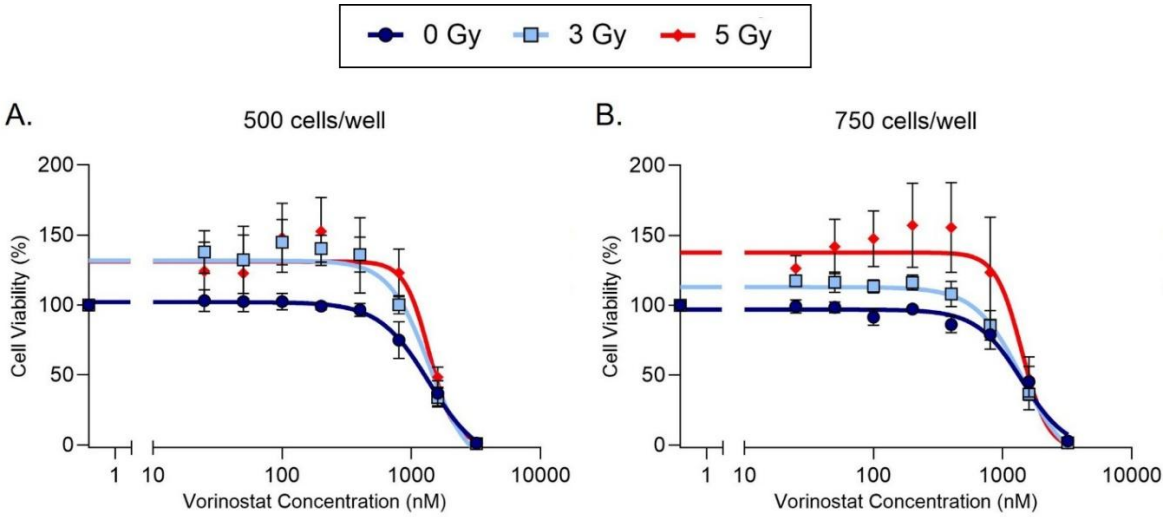

Supplementary Figure 2. HeLa cell viability following treatment with vorinostat of increasing concentrations and irradiation. HeLa cells were seeded at **(A)** 500 cells/well or **(B)** 750 cells/well and treated with different concentrations of vorinostat (0, 25, 50, 100, 200, 400, 800, 1600 and 3200 nM)**,** followed by irradiation with 3 Gy or 5 Gy. Values obtained from fluorescence detection upon addition of resazurin to wells 7 days post-radiation were normalised to the vehicle control at 0 Gy (for unirradiated samples), at 3 Gy (for irradiated samples at 3 Gy) or at 5 Gy (for irradiated samples at 5 Gy) (set as 100% cell viability) and the negative control (set as 0% cell viability) to detect any radiosensitisation effects. Data presented as mean ± standard deviation with x-axis plotted on a $\log_{10}$ scale. Three biological replicates (N = 3) with three technical replicates (n = 3). Absolute IC_{50} with 95% CI calculated together with extra sum-of-squares F test for statistical analysis. CI, confidence interval; IC_{50}, half maximal inhibitory concentration.

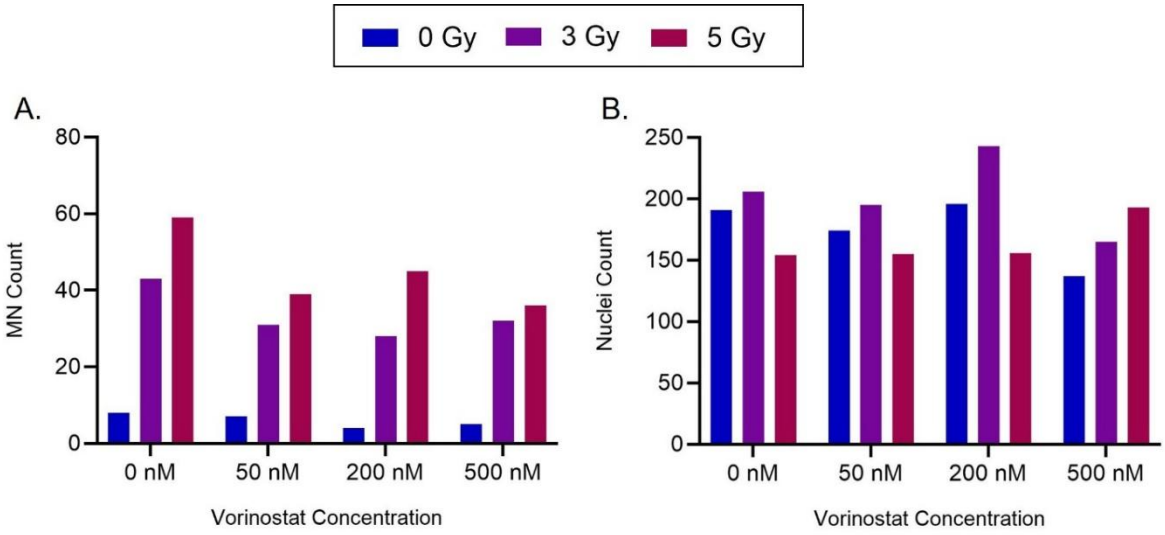

Supplementary Figure 3. Quantification of MN formation after vorinostat treatment and irradiation. HeLa cells were treated with vorinostat (0, 50, 200 or 500 nM), irradiated with 3 Gy or 5 Gy, and harvested for IF microscopy. 4-8 images were captured per condition and used to quantify the number of **(A)** MN and **(B)** nuclei. Data presented as total numbers from combining all images for each condition due to low and varying MN count in some images. Single experiment (N = 1) with one replicate measurement (n = 1). MN, micronuclei; IF, immunofluorescence.

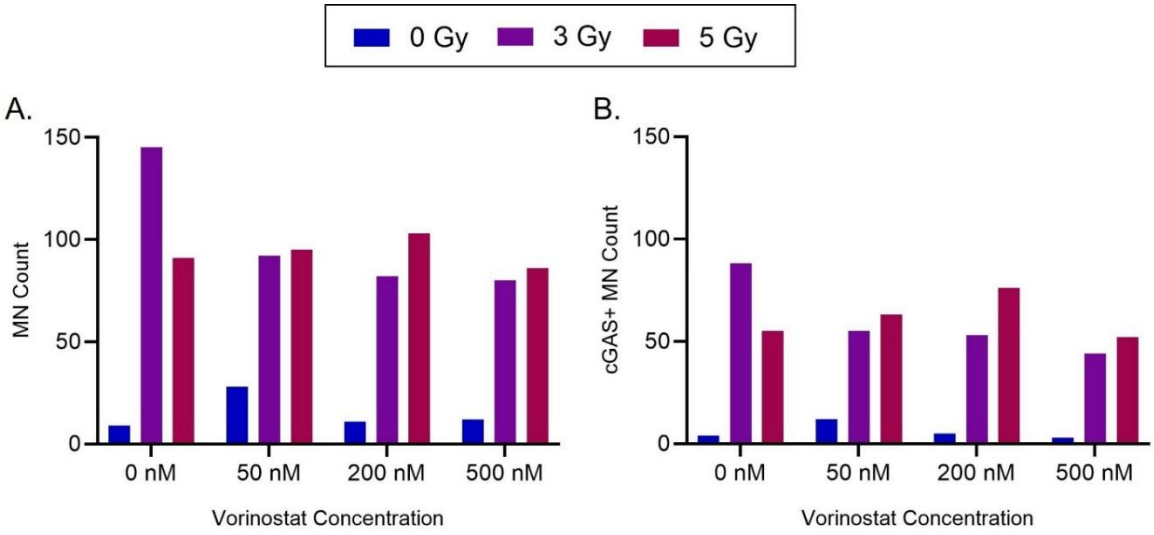

Supplementary Figure 4. Quantification of cGAS binding to MN after vorinostat treatment and irradiation. HeLa cells were treated with vorinostat (0, 50, 200 or 500 nM), irradiated with 3 Gy or 5 Gy, and harvested for IF microscopy. 4-8 images were captured per condition and used to quantify the number of **(A)** MN and **(B)** cGAS-positive MN. Data presented as total numbers from combining all images for each condition due to low and varying MN count in some images. Single experiment (N = 1) with one replicate measurement (n = 1). MN, micronuclei; IF, immunofluorescence.